UNIVERSITÀ DI PARMA

UNIVERSITÀ DEGLI STUDI DI PARMA

Dottorato di Ricerca in Tecnologie dell'Informazione

XXXI Ciclo

A SYSTEMATIC APPROACH TO THE ANALYSIS AND DESIGN OF ELECTRICAL MACHINES FOR AUTOMOTIVE TRACTION APPLICATIONS

Coordinatore:

Chiar.mo Prof. Marco Locatelli

Tutor:

Chiar.mo Prof. Carlo Concari

Dottorando: *Giorgio Pietrini*

Anni 2015/2018

Sommario

Negli ultimi decenni, il processo di elettrificazione ha interessato diversi aspetti e attività delle moderne società industrializzate. In questo contesto, l'elettrificazione dei trasporti mostra ancora un ritardo significativo. Ciò è dovuto principalmente alle prestazioni altamente competitive del petrolio come fonte di energia sia sotto il profilo tecnico sia economico. Tuttavia, le considerazioni in merito all'inquinamento dell'aria unitamente a politiche di autosufficienza energetica hanno recentemente aumentato l'interesse dell'industria automobilistica verso i powertrain ibridi ed elettrici. Inoltre, in pochi anni, i powertrain elettrici hanno raggiunto le prestazioni di quelli a combustione interna e, grazie a particolari caratteristiche (quali ad esempio il sovraccarico e gli alti livelli di efficienza), hanno persino superato i risultati dei powertrains convenzionali.

Il presente lavoro di tesi si concentra sulle macchine elettriche usate per la propulsione e il freno dei nuovi autoveicoli, con una particolare attenzione alla geometria di rotore, alle configurazioni degli avvolgmenti e ai più importanti trade-off relativi al design della macchina elettrica. Anche le possibilità di controllo sull'intero intervallo di velocità sono state considerate accuratamente. In più, un nuovo modello magnetico ricorsivo è stato sviluppato per eseguire ottimizzazioni multi-obiettivo dei parametri di rotore e un'inedita geometria di tipo spoke-type viene proposta per ridurre il volume del magnete permanente nella macchina.

Questa tesi è organizzata nel seguente modo: l'introduzione fornisce le informazioni di contesto generale in materia di elettrificazione dell'automobile, il capitolo 1 si occupa dei requisiti specifici di un motore per trazione dimostrando che i motori a magneti permanenti interni sono quelli che meglio soddisfano tali vincoli, nel capitolo 2 un'approfondita analisi di due macchine prese in considerazione come casi di studio viene svolta per mezzo sia di un'approccio analitico sia di simulazioni a elementi finiti, quindi nel capitolo 3 si esegue un'analisi critica delle principali opzioni di progetto della macchina e infine, nel capitolo 4, le linee-guida risultanti vengono applicate al design di un nuovo motore prototipo destinato alle corse di formula studentesca (SAE). Il progetto copre non soltanto i tipici aspetti elettromagnetici del motore ma anche le proprietà termiche e meccaniche della macchina.

Abstract

In the last decades, the electrification process has involved several aspects and activities of modern industrialized societies. In this context, the electrification of the transportation sector still exhibits a significant delay. This is mainly due to the rather competitive oil performances as an energy source from both a technical and economic point of view. However, air pollution considerations as well as energy self-sufficiency policies have recently raised the industrial interest for automotive hybrid and electric powertrains. Moreover, in just a few years, the electrical powertrains have reached the Internal Combustion Engine performances and, thanks to their particular features (such as the overload and the very high efficiency levels), they even outperformed most of the conventional powertrains.

This work focuses on the electrical machines used for the new car propulsion and braking, with special regard to the rotor geometry, winding configurations and all the most important trade-offs related to the machine design. The control capabilities over the whole speed range have also been considered carefully. In addition, a new recursive magnetic model has been developed to perform multi-objective rotor parameters optimization and a novel spoke-type geometry is proposed to reduce the machine permanent magnet volume.

This thesis is organized in the following way: the introduction gives the general background information about the car electrification topic, the chapter 1 deals with the specific requirements for a traction motor showing that the Interior Permanent Magnet is the motor type which best meets those constraints, in the chapter 2 a deep analysis is carried out on two case study machines by means of both analytic approach and Finite Elements simulations, then chapter 3 performs a critical analysis of the machine main design options and finally, in chapter 4, the resultant guidelines are applied to the design of a new motor prototype for Student Formula races. The design covers not only the typical electric and magnetic aspects of the motor but also the thermal and mechanical properties of the machine.

Contents

List of Figures

List of Tables

Main Symbols

d_c	Wire size (mm or AWG).
g	Airgap (mm).
g'	Carter's equivalent airgap $g' = k_c \cdot g$ (mm).
g''	Equivalent airgap due to saturation $g'' = k_{sat} \cdot g'$ (mm).
h_{bi}	Stator back-iron height (mm).
h_m	Permanent magnet height (mm).
h_s	Stator slot height (mm).
k_c	Carter's coefficient.
k_d	Winding distribution factor.
k_{fill}	Slot fill factor.
k_p	Winding pitch factor.
k_{pack}	Stacking factor.
k_w	Winding factor.
m	Number of phases.
n_c	Turns per slot.
n_{cc}	Wires in parallel per conductor.
n_{cs}	Equivalent number of turns in series per slot.
n_{pp}	Parallel circuits per phase.
p	Number of pole pairs.
p_s	Slot pitch (mm).
q	Number of slots per pole and phase.
r	Gear ratio.

t_{CP}	Vehicle acceleration time in constant power speed range (s).
t_{CT}	Vehicle acceleration time in constant torque speed range (s).
v	Vehicle longitudinal speed (m/s or km/h).
w_m	Permanent magnet width (mm).
w_{se}	Outer slot width (mm).
w_{so}	Stator slot opening width (mm).
w_t	Stator tooth width (mm).
y_q	Number of slots per pole.
$B_{gm}(\theta_r)$	No-load flux density distribution (T).
$\widehat{B}_{gm}$	PM-only component of the magnetic loading (amplitude) (T).
B_{rem}	Permanent magnet remanent flux density (T).
$B_{sd}(\theta_r)$	Stator armature reaction d-axis flux density distribution (T).
$\widehat{B}_{sd}$	Stator armature reaction d-axis magnetic loading (T).
$B_{sq}(\theta_r)$	Stator armature reaction q-axis flux density distribution (T).
$\widehat{B}_{sq}$	Stator armature reaction q-axis magnetic loading (T).
D	Stator inner diameter (mm).
D_a	Shaft diameter (mm).
D_e	Stator outer diameter (mm).
D_r	Rotor outer diameter (mm).
G_{Cu}	Stator copper mass (kg).
$G_{Fe\,rot}$	Rotor mass (Fe core) (kg).
$G_{Fe\,stat}$	Stator mass (Fe core) (kg).
$\hat{I}$	Current peak magnitude or amplitude (A).
I_{ch}	Characteristic current (A).
I_{MAX}	Maximum phase current (A).
I_{rot}	Rotor moment of inertia ($\mathrm{kg\,m^2}$).
J_s	Surface current density ($\mathrm{A\,mm^{-2}}$).
$\widehat{K}_s$	Linear current density or electrical loading ($\mathrm{A\,mm^{-1}}$).
L_c	Total single conductor length (mm).
L_d	d-axis inductance (H).
L_{ew}	End-winding length (mm).

L_{lam}	Lamination thickness (mm).
L_q	q-axis inductance (H).
L_{stk}	Stack length (mm).
N_s	Equivalent number of series conductors per phase.
N_{sc}	Number of coils in series per phase.
P_{MAX}	Maximum mechanical power (W).
Q_s	Number of slots.
R	Wheels radius (m).
R_{ph}	Phase resistance (Ω).
S_{1c}	Cross-section surface of the single copper wire (mm^2).
S_c	Cross-section surface of one conductor in the slot (mm^2).
$S_{c\,eq}$	Cross-section surface of an eq. single serial conductor (mm^2).
S_{Cu}	Copper part of the slot cross surface (mm^2).
S_{slot}	Cross-section surface of the slot (mm^2).
T	Motor torque (N m); temperature (°C).
T_{MAX}	Maximum motor torque (N m).
$U_{r\,i}$	$i-th$ rotor island magnetic potential (A).
$U_{rm\,i}$	No-load $i-th$ rotor island magnetic potential (A).
U_{sd}	d-axis current stator magnetic potential (A).
U_{sq}	q-axis current stator magnetic potential (A).
V_{bus}	Inverter bus voltage (V).
V_{MAX}	Maximum amplitude of the phase voltage fundamental (V).
α_i^e	Current angle (electrical deg or rad).
$\alpha_{m\,i}$	$i-th$ flux barrier angular width (at the airgap) (deg or rad).
α_s	Slot pitch (deg).
β_i^e	Current advance angle (electrical deg or rad).
θ	Generic angular coordinate (stator abc reference frame) (deg).
θ_m	Rotor angular position (deg).
θ_r	Generic angular coordinate (rotor dq reference frame) (deg).
μ_0	Magnetic permeability of free space ($H\,m^{-1}$).
μ_{rec}	Permanent magnet relative recoil permeability ($H\,m^{-1}$).

ξ	Saliency ratio.
τ_p	Pole pitch (mm).
ω_b	Base speed (rad/s or rpm).
ω_e	Rotor angular frequency (electrical rad/s).
ω_{MAX}	Machine maximum speed (rpm).
Λ_d	d-axis flux linkage (V s).
Λ_q	q-axis flux linkage (V s).
Λ_{PM}	PM-only flux linkage (V s).

Introduction

The process of transportation electrification started between the XIX and XX centuries with the first electrical railway, trolley-bus and subways. Through the years, many attempts have been made to bring electric traction also to the cars but with no impact on the mass production. Nowadays the conditions have changed. Energy self-sufficiency and the environmental issue are two of the most important challenges facing today's society. Transport electrification is probably the key to solve both these problems, as confirmed by the increasingly stringent standards for Internal Combustion Engine (ICE) emissions. For this reason, the global automotive industry is making substantial investments in order to broaden their supply of Hybrid (HEV) and Electric Vehicles (EV).

As numerous studies have shown [1], a large part of the overall energy demand in the modern nations is due to the transportation activities. For instance, according to the Lawrence Livermore National Laboratory (LLNL) Energy Flow Chart (Fig. 1), 28.7 % of the USA total energy consumption in 2016 could be attributed to the means of transport. Together with industrial activities (25.2 %), these two entries represent more than half of the annual energy budget. However, the composition of the energy sources is completely different. Industry uses natural gas (39 %), petroleum (33 %), electricity (13 %), biomass (9 %) and coal (5 %), whereas transport relies on petroleum for 92 % of its energy demand. There are two reasons for this imbalance: the oil very high energy density (about 10 kWh/L) and the affordable energy cost (approximately 0.04 $/kWh). In other words, oil is today both technologically

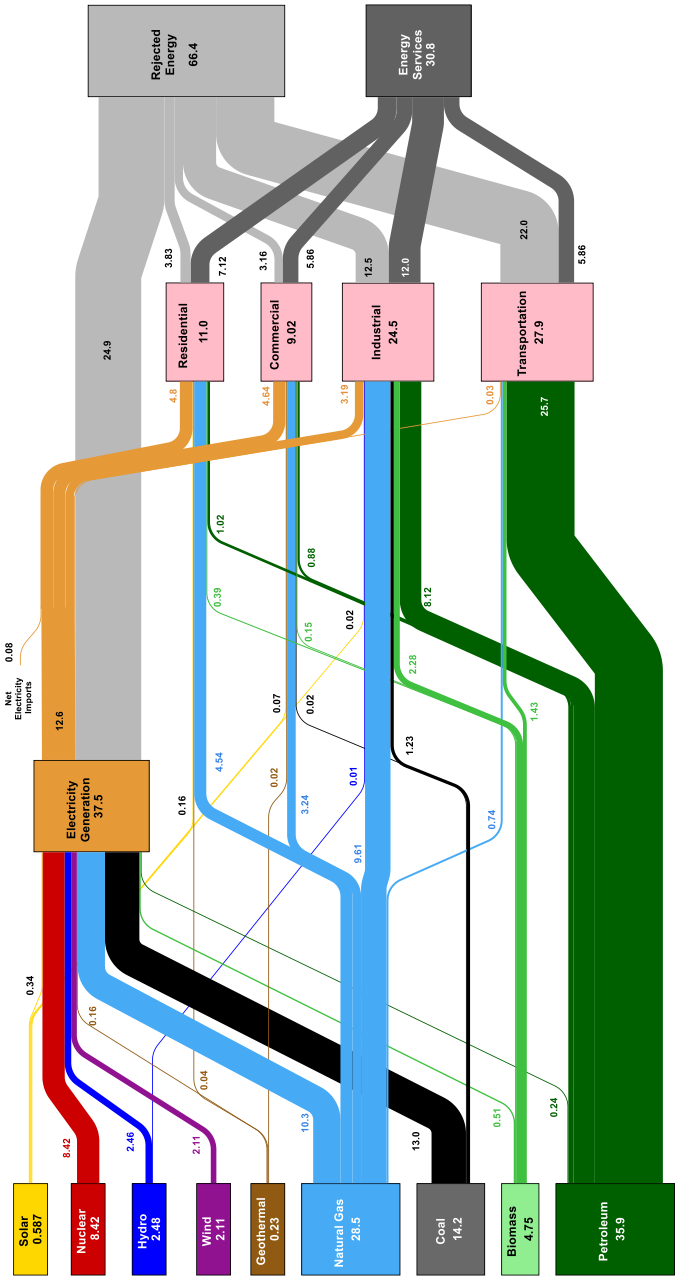

Figure 1: Estimated 2016 U.S. energy consumption: 102 EJ (or 102×10^{18} J).

Table 1: Energy storage comparison.

	Energy density (kWh/L)	Production cost ($/kWh)
Gasoline (Oil)	10	$0.04 \div 0.06$
Lead acid	0.1	60
Nickel-cadmium (Ni-Cd)	0.3	$250 \div 300$
Nickel-metal hydride (Ni-MH)	$0.18 \div 0.22$	$200 \div 250$
Lithium-ion polymer (LiPo)	$0.2 \div 0.25$	150
Lithium-ion	$0.2 \div 0.4$	150
Supercapacitor (EDLC)	$0.004 \div 0.014$	> 2000

and economically very competitive. As Tab. 1 shows, the performances of the main energy storage alternatives to oil are several orders of magnitude lower [2, 3]. Anyway, the oilfields strong localization makes the brent price subject to significant fluctuations. Moreover, the growing consumption of petroleum from emerging economies will likely drive the price up in the next years. Also the average energy efficiency of the modern industrial processes is higher (49 %) than the transport one (21 %). Electrical powertrains can rebalance the energy supplies and enhance the efficiency at the same time.

The first measures against the air pollution taken by the car manufacturers have been providing the cars with more filters, such as the DPF (Diesel Particulate Filter), and more advanced emissions after-treatment systems. Unfortunately, as stated by the EU Joint Research Centre Institute of Energy and Transport [4], the traffic related particulate matter (PM) consists of: exhaust particles, produced by the incomplete fuel combustion and concurrent lubricant volatilization; and non-exhaust particles, generated from road surface, clutch and especially tyre and conventional brake wear. Currently, exhaust and non-exhaust sources contribute almost equally to the total traffic-related PM10 emissions but as stricter exhaust emission rules go into effect, the non-exhaust sources relative contribution will increasingly become more significant. The

Table 2: Mechanical complexity comparison [5].

Parts	Chevrolet Bolt	VW Golf
Moving parts	24	149
(engine)	3	113
(gearbox)	12	27
(other)	9	9
+ Wearing parts	11	24
- Moving & wearing parts	0	6
Total	35	167

brake wear PM10 is characterized by high concentrations of heavy and transition metals (Fe, Cu, Zn, Sn, Sb), as well as of sulfur. These particles have toxic effects and can promote the occurrence of respiratory and cardiovascular diseases. In addition, the transition metals produce reactive oxygen species (ROS), intensifying the oxidative stress in the tissues. Triggering the immune response, these chemicals are also responsible for chronic inflammatory diseases like asthma. Electric motors are able to work equally as propulsive systems with efficiency levels (up to 97 %) unreachable by ICEs and as braking systems which can recharge the battery, converting the vehicle kinetic energy (regenerative brake). Electric and hybrid powertrains can therefore address the environmental issue in a more effective way, since are able to decrease both the exhaust and non-exhaust particulate.

Today's automotive industry is engaging with the challenge of the vehicle electrification in a simplifying perspective. The powertrain of the present electric cars includes typically only one electric motor for traction and regenerative braking, a single-speed gearbox, and only one inverter unit to feed and control the motor (e.g., Nissan Leaf, BMW i3, Tesla, GM/Chevrolet Bolt). Therefore, the complexity of an Electric Vehicle (EV) powertrain is very low compared to a conventional one [5, 6]. For instance (Tab. 2), a Volkswagen Golf powertrain

Table 3: Main (H)EV motors power densities [7].

	Motor	Peak power density (kW/L)	Peak specific power (kW/kg)	Year
HEV	Toyota Prius (50 kW)	3.3	1.1	2004
	Honda Accord (12 kW)	1.5	0.5	2006
	Toyota Camry (70 kW)	5.9	1.7	2007
	Lexus LS 600h (165 kW)	6.6	2.5	2008
	Toyota Prius (60 kW)	4.8	1.6	2010
BEV	Nissan Leaf (80 kW)	4.2	1.4	2012
	BMW i3 (125 kW)	6.4	2.3	2016
	Chevy-LG Bolt (150 kW)	7.5	2.7	2017
	DOE target	5.7	1.6	2020

is composed by 167 parts (149 moving and 18 wearing) whereas in a Chevy Bolt (which can be considered an equivalent EV car) this number drops to 35 parts (24 moving and 11 wearing). Looking at the Bolt's motor, only 3 moving parts can be counted while the Golf's 4-cylinder engine has 113 moving parts. Similarly, the Bolt's single-speed gearbox has only 4 gear wheels (12 moving parts), instead of the 27 moving parts in a Golf's 6-speed automatic transmission (Tab. 2). Moreover, many additional components, required by Internal Combustion Engine (ICE) cars, are not present in EVs: the clutch, the starter generator, the start-stop system, and emissions after-treatment. Of course, if on the one hand, the mechanical complexity decreases, on the other the electronic complexity rises but usually the overall density (with the only exception of the battery) results significantly higher in EVs. A 4-cylinder ICE, like that in the VW Golf, normally weighs approximately 140 kg, so it can achieve a specific power higher than 1 kW/kg very unlikely. On the contrary, the Chevy Bolt electric motor specific power is almost three times higher. Tab. 3 reports

Table 4: Annual fuel cost (mileage $>$ 16 000 km).

ICE	HEV	BEV
1000 ÷ 1200 $	500 ÷ 860 $	340 ÷ 420 $

the power densities of some of the most widespread traction electrical motors for both HEV and BEV (Battery Electric Vehicle) [7]. As can be observed, density ranges from 1.5 to 7.5 and rises with the power rating. The specific power and the density of motors with 125 kW or more already reach the U.S. Department of Energy (DOE) 2020 targets. HEVs rely on this complexity and density exchange between the mechanical powertrain half and the electrical one. If not, there would be no space on-board for the electric motor/generator (one or more as in Toyota/Lexus), inverters, DC-DC converters and so on.

By means of this mechanical simplification, the EV reliability is improved and the maintenance costs are substantially reduced. Taking into account the regular change of fluids (such as engine oil), preventive inspections and the parts replacement, the Golf's maintenance costs 610 $ a year on average, whereas a Bolt needs only 255 $ a year [5]. This means savings of 60 % on the annual maintenance bill. In addition, thanks to the high electric motor efficiency, the fuel costs also are remarkably decreased in HEVs and BEVs. In Tab. 4 can be found a fuel cost estimate for conventional ICE vehicles, HEVs and BEVs, based on an annual mileage of more than 16 000 km [2, 8]. High reliability and low cost of ownership are two of the most important factors for customers [9] during the vehicle selection process (see Fig. 2) and this explains the growing popularity of HEVs and BEVs in the recent years.

Anyway, EVs are not only cleaner, reliable and cost effective vehicles. Electric motors for automotive traction applications have also higher performances, as the above power density considerations suggest. Actually, the most active car manufacturers in the EV industrial sector belong to the high-end sportscar market segment since the high production costs find easily justification. For instance, the Tesla Roadster can reach a top speed of more than 400 km/h and

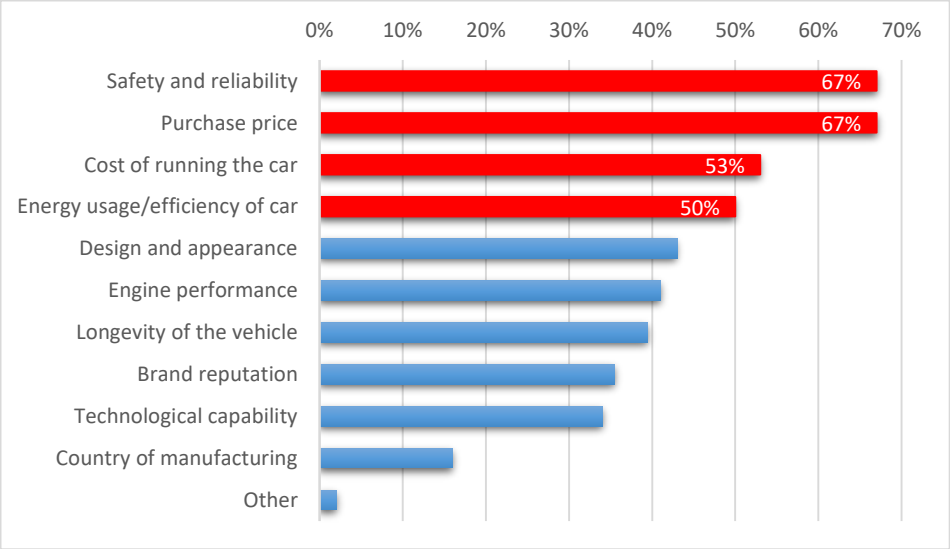

Figure 2: Customer survey about most important factors in vehicle selection process [9].

has a $0 - 100\,\mathrm{km/h}$ acceleration time of only $2.1\,\mathrm{s}$. The Rimac Concept Two exhibits even more amazing specifications: a $412\,\mathrm{km/h}$ top speed, $1.85\,\mathrm{s}$ for the $0 - 100\,\mathrm{km/h}$ acceleration, a maximum power near to $2\,\mathrm{MW}$, and four-wheel drive torque vectoring.

The performances upper-bound has been definitely set by the Venturi Buckeye Bullet 3 (VBB-3) on September 19, 2016. This experimental electric car, created by the Center for Automotive Research (CAR) of the Ohio State University under the leadership of Prof. Giorgio Rizzoni, has reached $549.4\,\mathrm{km/h}$ shattering the previous speed world record for an all-electric car set by the same team in 2010.

Although the scientific literature about electrical machines is very rich and there are several design methods, it is important to understand the effect of each design option in the context of electric propulsion. The aim of this thesis is to provide a reasoned choice of the most suitable motor type for EV and

HEV, and to find some guidelines in order to achieve the maximum performance in automotive traction. Then, at the end of this thesis, the project of an electric motor based on these principles is presented. In addition, a very computationally-efficient magnetic model for the rotor geometry optimization is proposed. A novel spoke-type rotor topology with reduced usage of rare-earth permanent magnets is also developed and analyzed in depth pointing out both the advantages and the weaknesses.

The two main approaches adopted in this work are analytical and Finite Element simulations. In particular, the latter were carried out using open source software (FEMM and ProjectChrono) together with the MATLAB computing environment to post-process the data. The Dolomites and SyR-e tools were also used for the design phase.

Chapter 1

Traction motors characteristics for EVs and HEVs

Contrary to the electric motors for industrial applications, which move external loads or operate tools, electrical motors for traction applications apply a propulsion force to a vehicle which incorporates the motor itself. Obviously, the torque fraction allocated to move the motor mass, instead of the main part of the vehicle, is wasted, therefore the power-to-weight ratio (or specific power) is of primary concern in these particular machines. Similar considerations can be made for the volume, so the torque density has a comparable importance.

Since the motor torque is directly related to its volume, most of the EV and HEV powertrains include a single speed gearbox to relax the motor torque requirements. However, in this way the motor rotation speed rises and then a satisfactory motor behavior at high speeds is also essential.

As discussed in the introduction, battery is the most expensive component in EVs. In order to guarantee the maximum range achievable with the on-board battery, the motor efficiency has to be carefully considered.

Finally, the electric motors have a specific feature, the overload capability, that is a great advantage with respect to ICEs. In the overload working condition, the motor can reach higher performances than the nominal rating

still remaining thermally safe for about 30 seconds or a couple of minutes, depending on the manufacturer. Intermittent overload for short durations is very useful for vehicle accelerations at any speed.

1.1 Interior Permanent Magnet motors

In summary, the main characteristics that an electrical motor for automotive traction should meet are:

- High specific torque and power;
- High torque and power density;
- Relatively high maximum speed;
- Good energy efficiency;
- Good overload capability;
- Competitive cost.

All these constraints make the design process rather difficult, as many tradeoffs have to be found.

Among the many electric motor typologies, three are the possible options to be used as traction EV unit: IMs (Induction Motors), SPM (Surface Permanent Magnet) motors and IPM (Interior Permanent Magnet) motors. As well known, the first belongs to the category of the asynchronous electrical machines whereas the second and third are synchronous.

IM has long been used for traction applications (e.g., trains, trolley-buses, subways...) because of its wide speed range (beyond 100 000 rpm). Anyway, IM torque density is not very high and its efficiency ν as well as its power factor (PF) are rather low [10]: the average product $\nu \cdot \mathrm{PF} \simeq 0.5$ expresses the net electric power converted in mechanical form. For this reason, today's car manufacturers are phasing out IMs from their catalog, although there are some important exceptions like Tesla.

SPM motor torque and power densities are much better, as well as its efficiency (more than 95 %) and power factor (above 0.9). However it is not as simple as with IM to reach high speeds, since the rotor magnetic field is produced by the permanent magnets (PM), and therefore it can't easily work in the flux weakening region. Drive failures at high speed are also extremely more dangerous due to the back-emf out of control. Moreover, the amount of PM, which this type of motor needs, is significant, resulting therefore in rather expensive solutions for high torque ratings. These observations explain why the SPM motors are rarely used in HEVs and EVs powertrains, except for the axial-flux permanent magnets (AFPM) motors. AFPM motors have unquestionably the best-in-class torque density and some electrical motor manufacturers (e.g., Yasa motors and Emrax) have focused their production on this motor topology. Due to the particular aspect ratio of these machines, which looks like a disk, it is not always simple to place AFPM motors on board EVs. The rotor disk shape in AFPM machines has also another drawback: the high moment of inertia compared to a conventional rotor with the same mass. This lowers the acceleration (and regenerative braking) performances of an EV, but such an effect may be exploited in HEV mounting the AFPM motor directly on the engine crank palm thus replacing the engine flywheel [11].

Anyway, most of the car manufacturers today provide their HEVs and EVs with IPM motors for the traction unit and also the academic research agrees considering IPM motors to be the most suitable technology for automotive traction applications [13, 14]. IPM motors belong to the category of the permanent magnets synchronous motors (PMSM) along with SPM but, having the PMs buried inside the rotor, saliency is introduced in the machine magnetic circuit (see Fig. 1.1). Since the magnetic incremental permeability of rare-earth magnet materials is nearly that of free space, the magnetic reluctance along the d-axis flux path (where the PMs are mounted) results higher than in q-axis. In an SPM machine, the *effective* airgap (that is the magnetic one, not geometrical) in the flux path of L_d (d-axis inductance) and L_q (q-axis inductance) is the same, then $L_d = L_q$. On the contrary, looking at the

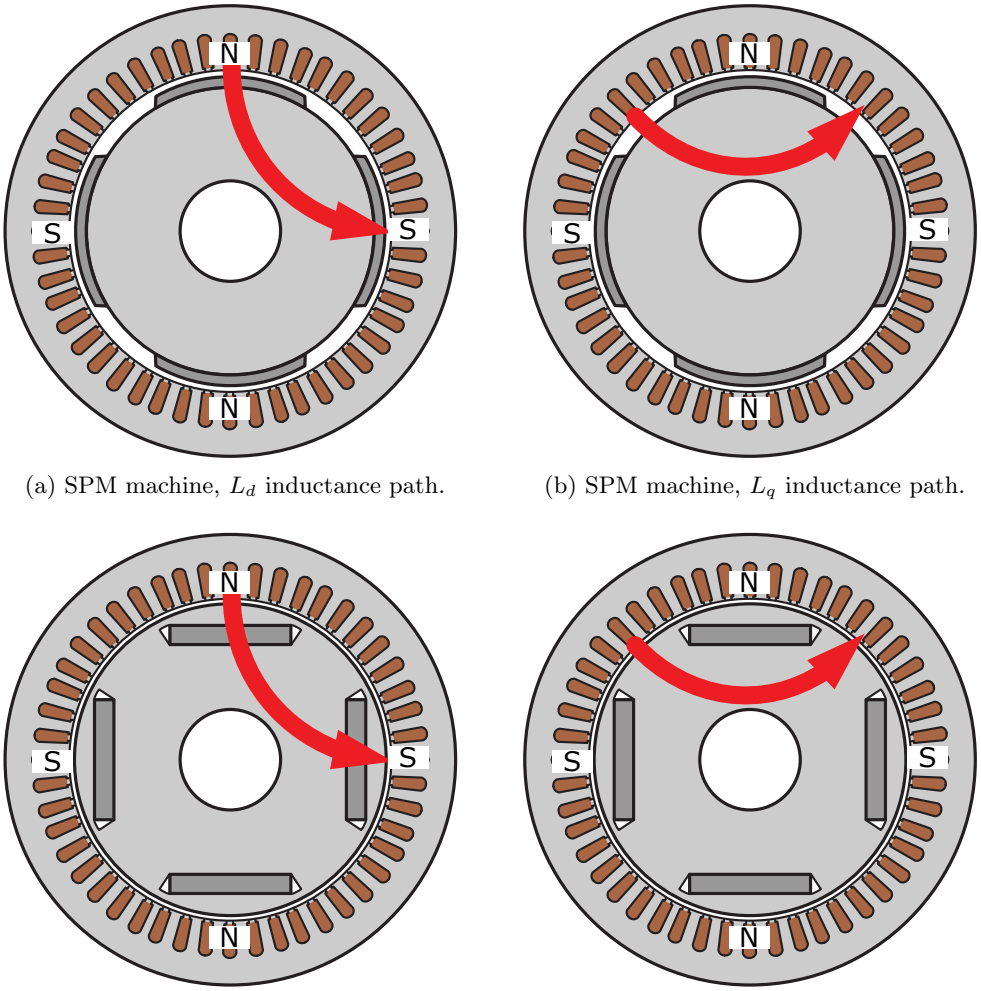

(a) SPM machine, L_d inductance path.

(b) SPM machine, L_q inductance path.

(c) IPM machine, L_d inductance path.

(d) IPM machine, L_q inductance path.

Figure 1.1: SPM versus IPM drawings (adapted from [12]).

IPM magnetic circuit in rotor reference frame [12, 15], the d-axis flux path is $steel \rightarrow air \rightarrow steel \rightarrow magnet \rightarrow steel \rightarrow magnet \rightarrow steel \rightarrow air \rightarrow steel$, whereas q-axis flux path is $steel \rightarrow air \rightarrow steel \rightarrow air \rightarrow steel$ as shown in Fig. 1.1c, 1.1d. Hence, in IPM motors $L_d < L_q$ as the d-axis (or direct axis)

is the axis that is aligned with the PM field and the q-axis (or quadrature axis) is 90° electrically advanced from the d-axis. As a consequence, the motor torque production characteristics are changed. In Fig. 1.2 the main IPM rotor topologies are reported together with the SPM (Fig. 1.2a) for comparison. Permanent magnets can also be arranged in more layers, as happens in the PM assisted Synchronous Reluctance Motors (PMASynREL).

Saliency, namely the difference in the d and q-axis inductances, produces reluctance torque in addition to the PM electromagnetic torque (or mutual torque).

The general torque expression (1.1) applied to the IPM machines shows the two torque components clearly: the first term is independent of i_d but is directly proportional to the stator current i_q, so it is the mutual torque component, while the second term is proportional to the $i_d \cdot i_q$ product and to the difference $L_d - L_q$, so it is the reluctance torque part.

$$T = \frac{3}{2} \cdot p \cdot (\Lambda_d \, i_q - \Lambda_q \, i_d) = \frac{3}{2} \cdot p \cdot [\Lambda_{PM} + (L_d - L_q) \; i_d] \, i_q \tag{1.1}$$

where p is the pole pairs number, Λ_d is the d-axis flux linkage as well as Λ_q is the q-axis flux linkage and Λ_{PM} is the PM-only flux linkage.

After defining the characteristic current as $I_{ch} = \Lambda_{PM}/L_d$ and the saliency ratio $\xi = L_q/L_d$, equation 1.1 can be rewritten as follows:

$$T = \frac{3}{2} \cdot p \cdot [I_{ch} \, i_q - i_d \, i_q \cdot (\xi - 1)] \, L_d \tag{1.2}$$

Since in IPM machines $\xi > 1$, it is worth noting that i_d must be always negative in order to have the reluctance torque concordant with the PM torque. The i_q sign gives the torque direction.

Obviously, the higher the saliency ratio, the higher the reluctance torque and similarly the mutual torque component can be increased by adjusting the PM dimensions in order to vary the I_{ch} (or the PM flux linkage Λ_{PM}). Therefore, the relative weight of the two torque components is set during the machine design process. One extreme of the design space is represented by

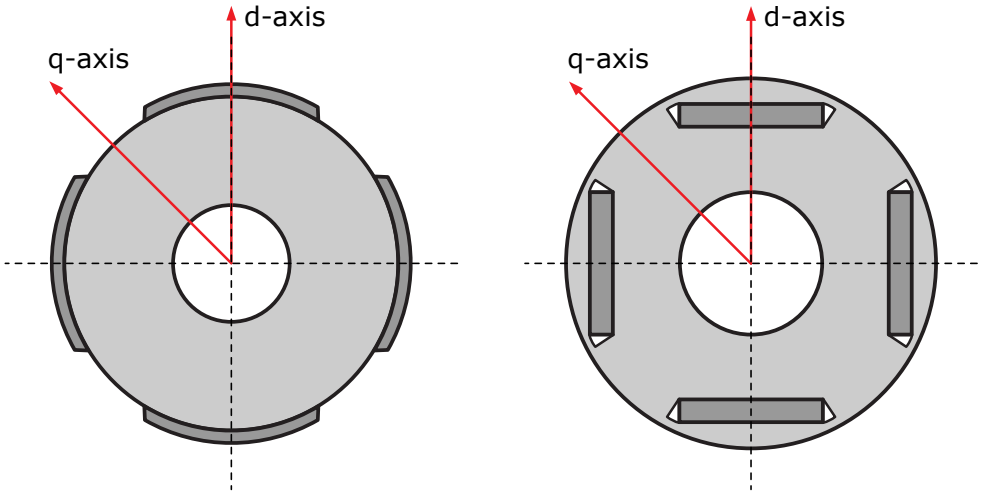

(a) SPM rotor.

(b) IPM rotor (radial magnetization).

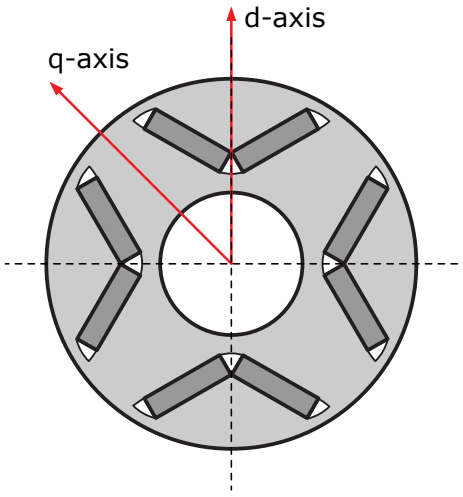

(c) V-shape IPM rotor (radial magnetization).

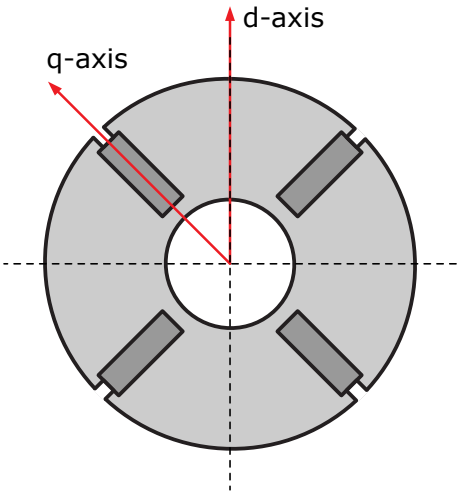

(d) Spoke-type IPM rotor (tangential magnetization).

Figure 1.2: PMSM rotor drawings with d/q-axes (adapted from [12]).

the SPM rotor topology, where $\xi = 1$ and the reluctance torque component equals zero. At the other extreme, the magnets are completely removed from

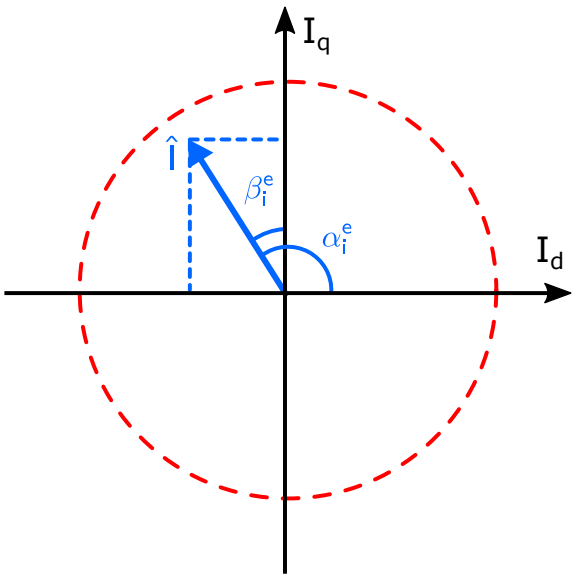

Figure 1.3: Current vector and angles convention.

the rotor, then the PM torque part entirely disappears and the motor becomes a pure synchronous-reluctance machine.

However, it should not be forgotten the importance of the L_d term in (1.2) in order to achieve the overall torque target value, because it is related to the machine size (and reluctance).

Since in an IPM motor the torque is a function of two variables (i_d, i_q), it is possible to plot a constant-torque curve with an hyperbolic shape in the dq current plane for each torque value. Finally it is necessary to define a criterion in order to associate to each torque value a single (i_d, i_q) pair. Typically the maximum torque-per-ampere control technique (MTPA) is used. This criterion says that for each torque value, the (i_d, i_q) pair to be chosen in the constant-torque locus is the one with the lowest current modulus. Therefore, MTPA (as well as every other control technique) describes a trajectory in the dq current plane.

The phasorial description of the current vector is also very common: the

magnitude $\hat{I}$ and angle α_i^e are used instead of i_d and i_q.

$$\begin{cases} i_d = \hat{I}\cos\alpha_i^e = -\hat{I}\sin\beta_i^e \\ i_q = \hat{I}\sin\alpha_i^e = \hat{I}\cos\beta_i^e \end{cases} \tag{1.3}$$

The superscript e stands for electric angles. As shown in (1.3) and Fig. 1.3, there is also another option for the current phasor angle: $\beta_i^e = \alpha_i^e - \pi/2$, or current advance angle. Typically α_i^e is more convenient for the control algorithm and the simulation of the machine while β_i^e can be useful for the analytic expressions but they are absolutely equivalent. Equations (1.2) and (1.3) yield a new torque formula:

$$T = \frac{3}{2}\cdot p\cdot\left[I_{ch}\,\hat{I}\cos(\beta_i^e) + \frac{1}{2}(\xi-1)\,\hat{I}^{\,2}\sin(2\,\beta_i^e)\right] L_d \tag{1.4}$$

By means of differentiation, the β_i^e expression (1.5) and the dq-plane relationship (1.6) for MTPA may be found.

$$\beta_i^e = \arcsin\frac{-I_{ch} + \sqrt{I_{ch}^2 + 8\,(\xi-1)^2\hat{I}^{\,2}}}{4\,(\xi-1)\,\hat{I}} \tag{1.5}$$

$$i_q = \pm\sqrt{i_d^2 - \frac{I_{ch}}{\xi-1}\,i_d} \tag{1.6}$$

The result is a slightly nonlinear locus, although for preliminary analysis the linear approximation is frequently used, if the iron magnetic saturation is not too heavy.

Unfortunately, the limits on the maximum voltage and current that can be supplied by the drive inverter restrict the available operating range in terms of the machine torque and speed. These two constraints influence substantially the control trajectory, making necessary to replace the MTPA with other control techniques, such as the flux weakening (FW), in particular operating conditions. These aspects will be discussed in the next subsections, but first a simple electric model of the IPM machine shall be examined.

The IPM motor flux linkage equations in the dq reference frame are:

$$\begin{cases} \Lambda_d = \Lambda_{PM} + L_d\, i_d \\ \Lambda_q = L_q\, i_q \end{cases} \tag{1.7}$$

and the voltage relationships are:

$$\begin{cases} v_d = R_s\, i_d + L_d \dfrac{di_d}{dt} - \omega_e\, L_q\, i_q \\ v_q = R_s\, i_q + L_q \dfrac{di_q}{dt} + \omega_e\, \left(L_d\, i_d + \Lambda_{PM}\right) \end{cases} \tag{1.8}$$

where ω_e is the rotor angular frequency in electrical rad/s. Fig. 1.4 shows the corresponding equivalent circuits.

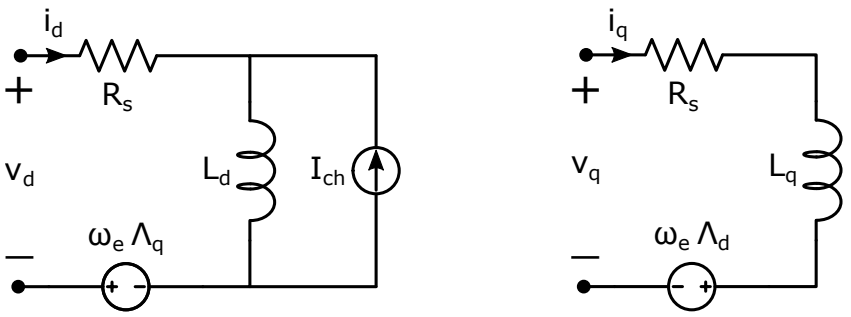

(a) d-axis. (b) q-axis.

Figure 1.4: IPM motor dq-frame equivalent circuits.

Equation (1.8) can be simplified under steady-state conditions, which means setting the di/dt terms to zero, and by neglecting the resistive voltage drops, as they are typically much smaller than the cross-coupled back-emf voltage terms. The steady-state voltage equations result:

$$\begin{cases} v_d = -\omega_e\, L_q\, i_q \\ v_q = \omega_e \cdot \left(L_d\, i_d + \Lambda_{PM}\right) \end{cases} \tag{1.9}$$

1.1.1 Control capability curves

Assuming that the maximum phase current available from the source is I_{MAX}, the current limit curve in the dq plane is a circle with the following expression:

$$\sqrt{i_d^2 + i_q^2} \leq I_{MAX} \tag{1.10}$$

The center of this circle is placed in $i_d = i_q = 0$ and the radius is I_{MAX}. All the current configurations corresponding to the points of the dq plane outside this circle are not feasible because represent an overcurrent condition.

The voltage limit can be expressed with a relationship similar to (1.10) but the resulting locus is not so straightforward.

$$\sqrt{v_d^2 + v_q^2} \leq V_{MAX} \tag{1.11}$$

where V_{MAX} is the maximum amplitude of the phase voltage fundamental.

Substituting (1.9) in (1.11) and applying the definitions for the characteristic current and saliency ratio, the voltage limit curve can be derived:

$$(i_d + I_{ch})^2 + \xi^2 \, i_q^2 \leq \left(\frac{V_{MAX}}{L_d \, \omega_e} \right)^2 \tag{1.12}$$

This equation defines an ellipse in the dq current plane that is centered on the negative d-axis at $i_d = -I_{ch}$ with major and minor radii of $V_{MAX}/(L_d \, \omega_e)$ and $V_{MAX}/(L_q \, \omega_e)$ oriented in the d- and q-axis directions respectively.

Again, the (i_d, i_q) points that fall outside this ellipse represent unfeasible control conditions. Since both the limit constraints have to be satisfied simultaneously, the acceptable operating area in the dq current plane is the intersection of the two areas defined by (1.10) and (1.12).

Assuming a three phase machine having windings arranged in the wye configuration, V_{MAX} is related to the inverter bus voltage V_{bus} in three ways, depending on the modulation technique adopted:

- $V_{MAX} = \dfrac{1}{2} V_{bus} = 0.5 \, V_{bus}$ for the sinusoidal PWM,

- $V_{MAX} = \frac{1}{\sqrt{3}} V_{bus} \simeq 0.577\, V_{bus}$ for the space-vector PWM,
- $V_{MAX} = \frac{2}{\pi} V_{bus} \simeq 0.637\, V_{bus}$ for the six-step square-wave modulation.

The most common voltage modulation in HEV and EV powertrains is the space-vector PWM as it achieves the best tradeoff between the fundamental amplitude and the distortion. Anyway, some manufacturers switch their inverter units to the six-step modulation only near the maximum speed.

While the current limit constraint is "static", the voltage limit ellipse shrinks as the rotor speed increases because of the radii inverse proportionality to ω_e. This effect, combined with the voltage limit ellipse position in relation to the current limit circle, leads to different dynamic behaviors and performances according to the I_{ch}. Therefore, the characteristic current influences the high speed operating range. Three cases are possible [16].

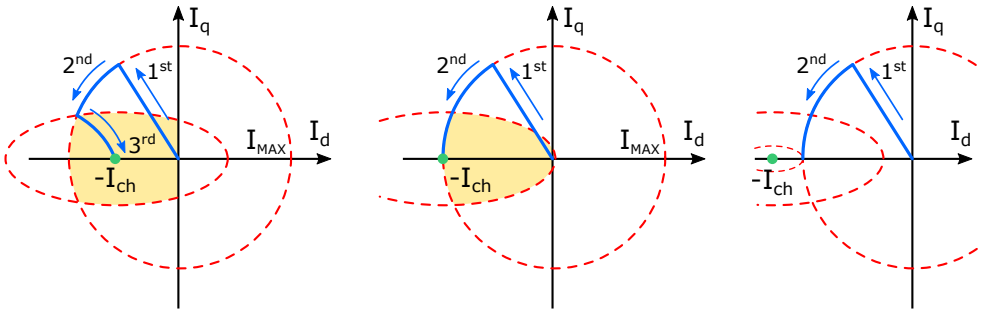

(a) $I_{ch} < I_{MAX}$ case. (b) $I_{ch} = I_{MAX}$ case. (c) $I_{ch} > I_{MAX}$ case.

Figure 1.5: Types of PMSMs operating areas.

Case 1: $I_{ch} < I_{MAX}$ When the characteristic current is smaller than the maximum current, the center of the voltage limit ellipse (the green dot in Fig. 1.5) is placed inside the current limit circle. It means that an intersection between the acceptable current area and the acceptable voltage area always exists, even for a (theoretical) infinite rotor speed (when the voltage ellipse

becomes coincident with its center). This intersection is highlighted with yellow in Fig. 1.5. It is worth noting that only the left half-plane is considered for the acceptable area, as i_d must be negative. In this case, three operating regions can be observed along the control trajectory (the blue line).

The first corresponds to the MTPA and in this interval of speeds, only the current limit constraint exerts his influence up to ω_b. The rotor speed ω_b is called base speed and represents the highest speed at which the motor can produce the maximum torque. Maximum mechanical power is also reached by the motor at ω_b. Then, the second region begins as the back-emf magnitude would exceed the V_{MAX} if the speed rises further. The FW technique uses the magnetic armature reaction to decrease the d-axis flux linkage, thus extending the motor speed range.

By substituting (1.3) in (1.9), it results that the back-emf magnitude is a function of the current advance angle. Increasing β_i^e has the effect of counteracting the back-emf growth due to the speed.

$$\begin{cases} v_d = -\omega_e \, L_q \, \hat{I} \cos \beta_i^e \\ v_q = \omega_e \cdot (\Lambda_{PM} - L_d \, \hat{I} \sin \beta_i^e) \end{cases} \tag{1.13}$$

In other words, the control trajectory in region two follows the current circle in order to stay inside the acceptable area, despite the shrinking voltage limit ellipse. By so doing, the rotor speed can reach values beyond ω_b. Since the control trajectory no longer follows MTPA, the torque decreases at the same time, hence the power remains constant as current and voltage magnitudes. Rotor saliency facilitates the FW control technique.

The region three starts when the voltage constraint radii are so small that control trajectory has to detach from the current limit circle, going towards the $(-I_{ch}, 0)$ point. Actually, it is rather a "current derating" as current modulus is lower than I_{MAX}. Since the electric volt-ampere power is lower, an undesirable mechanical power drop occurs. This matter will be developed more deeply in the next chapter.

Case 2: $I_{ch} = I_{MAX}$ This could be called the "optimal design" case for an IPM motor. Setting $I_{ch} = I_{MAX}$ provides all the useful features of case one, with special regard to MTPA and FW control techniques but without the region three drawback (see Fig. 1.5b). Unfortunately, it is not possible to satisfy the $I_{ch} = I_{MAX}$ condition with both the overload and nominal current, therefore the case two and one normally coexist in the same IPM machine respectively in overload and nominal operating conditions.

Case 3: $I_{ch} > I_{MAX}$ When the center of the voltage limit ellipse (Fig. 1.5c) is placed outside the current limit circle, an intersection between the acceptable current area and the acceptable voltage area not always exists. This means that the machine maximum speed ω_{MAX} is inherently limited. While case one and two are typical for IPM motors, the SPM machines belong to the case three due to the large effective airgap which lowers the L_d and increases the I_{ch}.

1.1.2 Dynamic curves

An example of IPM machine dynamic curves torque and power versus speed can be observed in Fig. 1.6. The MTPA and FW (or maximum torque per voltage MTPV) regions can be easily identified: the first (between 0 and ω_b) is the constant torque speed range (CTSR), whereas the second ($\omega_b - \omega_{MAX}$) is the constant power speed range (CPSR). The effects of these operating regions and of the related parameters on vehicle performances will be explained in the next sections. An additional interesting feature of the IPM motors is the overload capability on the whole speed range as can be seen in Fig. 1.6: the dashed curves are for the nominal conditions, the solid curves represent the overload conditions.

An example of SPM (Fig. 1.7) and IM (Fig. 1.8) power versus speed curves are reported for comparison [13, 14].

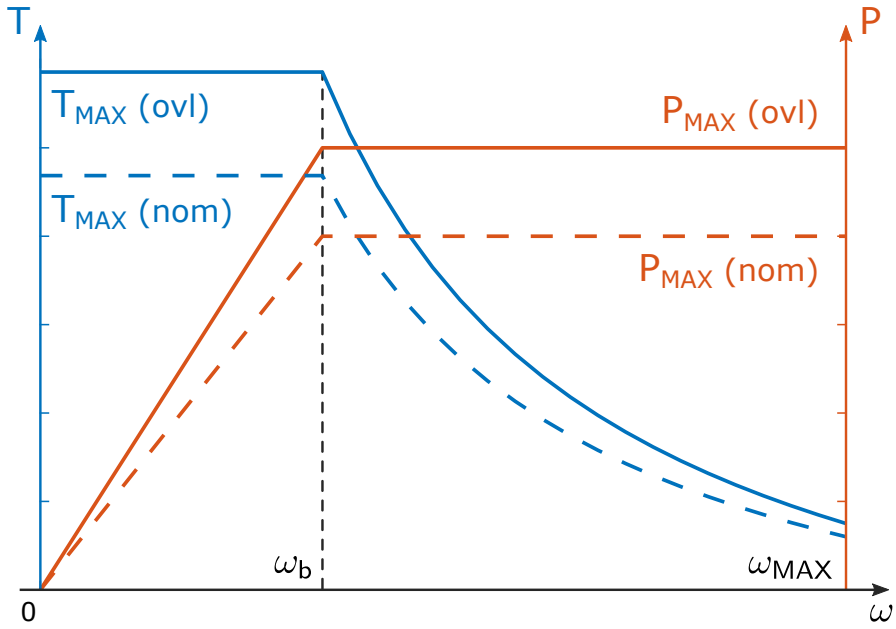

Figure 1.6: Illustrative drawing of the IPM dynamic behavior.

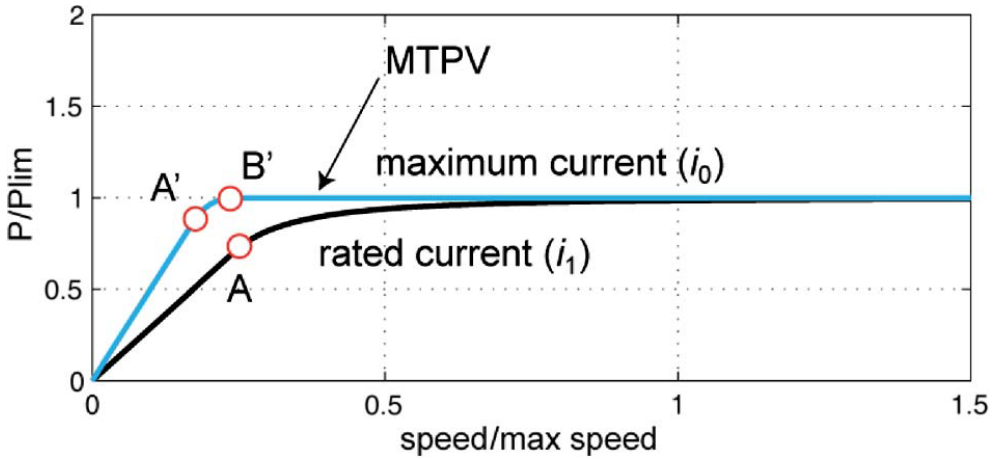

Figure 1.7: SPM power versus speed curves, for rated and overload current amplitudes [13].

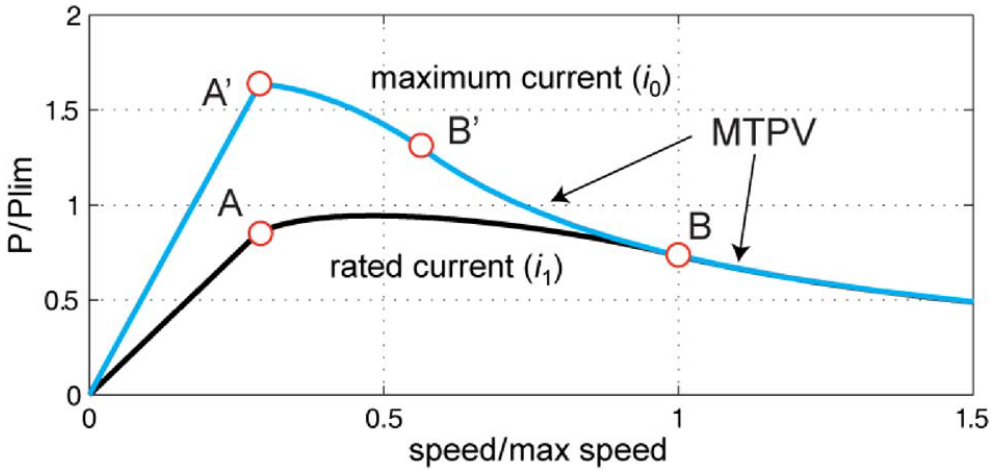

Figure 1.8: IM power versus speed curves, for rated and overload current amplitudes [13].

1.2 Longitudinal vehicle model

Generally speaking, the most common performance figures of merit related to a road vehicle are its capability to both accelerate and decelerate, and negotiate grades in a straight-line motion. These specifications are function of many vehicle parameters and, normally, specific system simulations should be used for maximum detail. However such an in-depth approach is beyond the scope of this section. Here a basic vehicle model is defined in order to identify the best characteristics for the motor and how the vehicle parameters can influence its structure.

This model [12] considers the vehicle running on a straight roadway with two-dimensional only movement. From the second law of motion, the main forces acting on the vehicle, shown in Fig. 1.9, are related in the following way:

$$F_t - F_w - F_g - F_r = a \cdot m \tag{1.14}$$

F_t is the vehicle traction force, F_w is the aerodynamic resistance force, F_g is the grading resistance force, F_r is the rolling resistance force, a is the acceleration

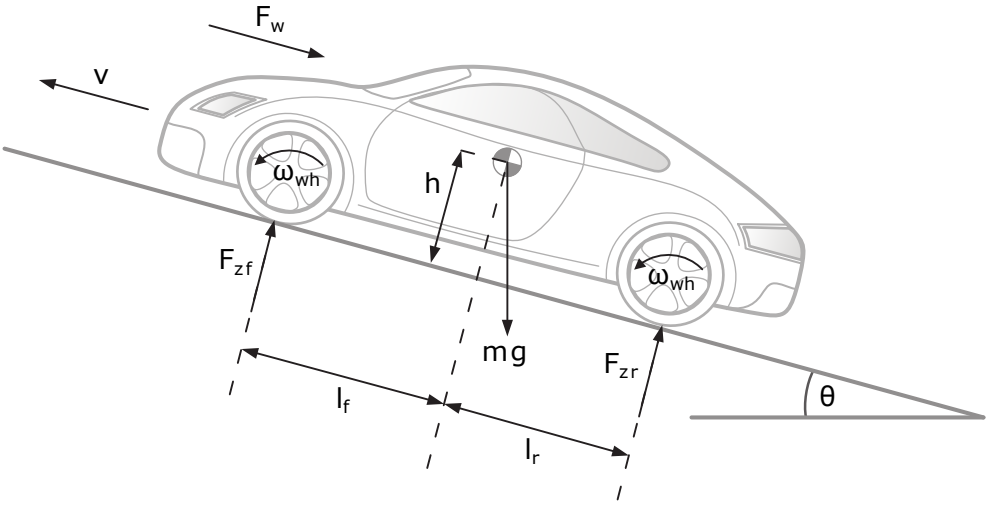

Figure 1.9: Forces acting on the vehicle (adapted from [12]).

and m is the vehicle mass.

As the car moves through the air, high-pressure areas arise in front of the vehicle and low-pressure areas behind the vehicle. Both these pressure zones act against the car motion. The aerodynamic resistance force is a function of effective vehicle frontal area, A, and the aerodynamic drag coefficient, C_d, which are highly dependent on the design of the vehicle body, the air density ρ, the vehicle longitudinal speed v and the wind speed v_w.

$$F_w = \frac{1}{2}\,\rho\,A\,C_d \cdot (v + v_w)^2 \tag{1.15}$$

The gravity force opposes the forward motion of the vehicle during grade climbing and aids the forward motion during grade descending. The grading resistance force expression is the following:

$$F_g = m\,g\,\sin(\theta) \tag{1.16}$$

where g is the gravitational acceleration $g = 9.81\,\mathrm{m/s^2}$ at sea level and θ is the road angle.

Finally, when the tire rolls, as a result of tire distortion or hysteresis, the normal pressure in the leading half of the contact patch is higher than that in the trailing half. A rolling resistance force F_r is therefore produced and this force is a function of the normal load $F_z = m\,g\,\cos(\theta)$ and the rolling resistance coefficient f_r.

$$F_r = F_z\,f_r = m\,g\,f_r\cos(\theta) \tag{1.17}$$

From the energy point of view, these expressions may be written also in a "power balance" form. As mechanical work is $W = F \cdot l$, where l is a displacement, the associated power comes from the W derivation with respect to time.

$$P = \frac{dW}{dt} = F\,\frac{dl}{dt} = F \cdot v(t) \tag{1.18}$$

As a consequence, power losses (P_w, P_g, P_r) can be associated to the forces F_w, F_g and F_r through a simple multiplication by $v(t)$. Equation 1.14 becomes:

$$P_t - P_w - P_g - P_r = a \cdot m \cdot v(t) = \frac{dE_k}{dt} \tag{1.19}$$

where $E_k = 0.5 \cdot m\,v^2(t)$ is the vehicle kinetic energy. The traction net power P_{tn} available, namely P_t minus the losses, is the vehicle kinetic energy rate of change. Actually, in EVs the kinetic energy takes two forms: the first is related to the longitudinal vehicle speed and it represents the useful energy portion, while the second is the rotational kinetic energy of the wheels and the rotor. It is a share of power not lost but stored in rotating inertial masses but it degrades the acceleration and deceleration vehicle performances anyway. A more accurate traction net power definition should be:

$$\begin{aligned} P_{tn} &= P_t - P_w - P_g - P_r - \frac{d}{dt}\left[\frac{1}{2}\left(I_{wh} + r^2\,I_{rot}\right)\omega_{wh}^2\right] \\ &= P_t - P_w - P_g - P_r - \frac{\left(I_{wh} + r^2\,I_{rot}\right)}{R^2} \cdot a \cdot v(t) \end{aligned} \tag{1.20}$$

where r is the gear ratio, I_{rot} is the rotor moment of inertia and $\omega_{wh} = v/R$, I_{wh} are the wheels speed and moment of inertia respectively. Although I_{wh}

is always larger than I_{rot} substantially, the rotor moment of inertia has to be referred to the slower shaft of the gear, by means of the r^2 factor in (1.20).

Observing (1.20), the importance of the motor P_t is clear, as a significant fraction of the power cannot contribute to the acceleration or deceleration of the EV. From (1.19) and (1.20) results:

$$P_{tn} = \frac{dE_k}{dt} \tag{1.21}$$

1.3 Acceleration time

As explained in section 1.1, the IPM motor dynamic curve consists of a constant torque speed range (CTSR), when the torque has the maximum constant value T_{MAX} and the power grows linearly with speed; and a constant power speed range (CPSR), where power reaches the maximum value P_{MAX} and torque decreases accordingly to speed. The two regions are separated by the base speed ω_b. All these parameters, together with the gearbox ratio r and the traction wheels radius R have an impact on the acceleration time, one of the vehicle basic features.

1.3.1 Constant torque speed range

In CTSR, the net maximum torque $T_{MAX\,n}$, that is the T_{MAX} minus the torque components wasted by the losses, is nearly constant, therefore also the maximum propulsive force $F_{MAX\,n}$ and the vehicle acceleration a are constant.

$$F_{MAX\,n} = \frac{r}{R}\, T_{MAX\,n} \tag{1.22}$$

$$a = \frac{F_{MAX\,n}}{m} = \frac{r \cdot T_{MAX\,n}}{R \cdot m} \tag{1.23}$$

The integral of a with respect to time yields the vehicle speed v_{CT} corre-

sponding to the motor ω_b.

$$\begin{cases} v_{CT} = \displaystyle\int_0^{t_{CT}} a\,dt = \frac{r \cdot T_{MAX\,n}}{R \cdot m}\, t_{CT} & \text{(1.24a)} \\ v_{CT} = \dfrac{R}{r}\,\omega_b & \text{(1.24b)} \end{cases}$$

The acceleration time component in CTSR results:

$$t_{CT} = \frac{R^2\,\omega_b\,m}{r^2\,T_{MAX\,n}} \tag{1.25}$$

1.3.2 Constant power speed range

In CPSR, the power can be considered as constant with reasonable approximation. Recalling (1.21),

$$\int_{t_{CT}}^{t_{CP}} P_{MAX\,n}\,dt = (t_{CP} - t_{CT})\,P_{MAX\,n} = [E_k]_{t_{CT}}^{t_{CP}} \tag{1.26}$$

where $P_{MAX\,n}$ is the maximum traction net power.

From (1.26), (1.24b) and $P_{MAX\,n} = \omega_b \cdot T_{MAX\,n}$ results:

$$\begin{aligned} t_{CP} &= \frac{m}{2\,P_{MAX\,n}}\,v_{CP}^2 - \frac{m}{2\,\omega_b\,T_{MAX\,n}} \cdot \frac{R^2\,\omega_b^2}{r^2} + t_{CT} \\ &= \frac{m}{2\,P_{MAX\,n}}\,v_{CP}^2 + \frac{R^2\,\omega_b\,m}{2\,r^2\,T_{MAX\,n}} \end{aligned} \tag{1.27}$$

A vehicle acceleration not necessarily pushes the motor in CPSR region. If a very low speed acceleration is considered, the target speed could be achieved within the CTSR and the (1.25) may be used. However, typically, the standard acceleration time used to evaluate the car performances is from 0 to $v_{CP} = 100\,\text{km/h}$ and the motor reaches the CPSR, then (1.27) has to be applied.

Equation 1.27 means that the acceleration time involves two terms: the second may be lowered by means of T_{MAX}, but normally it is limited by the tire-road adhesion together with r, while the first term can be reduced proportionally with P_{MAX}.

This demonstrates again how important is the motor power rating for the vehicle dynamic performances.

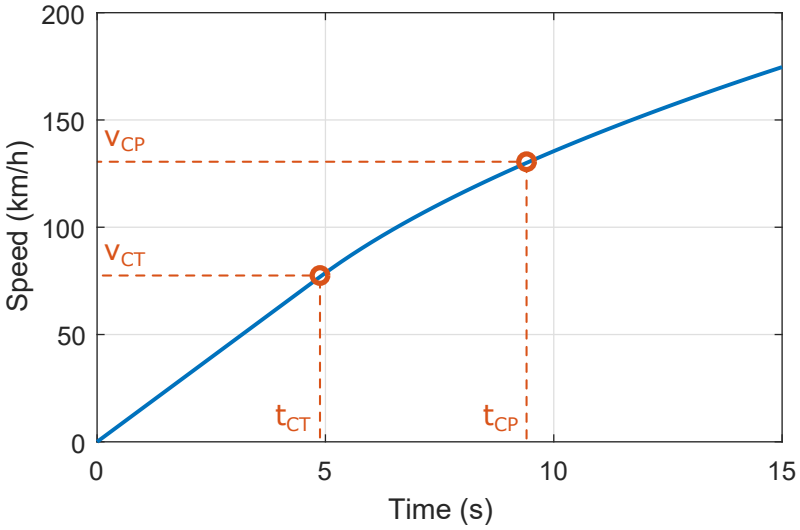

Figure 1.10: Example of a vehicle speed vs. time plot during acceleration.

1.4 Vehicle top speed

The top speed is another very common information taken into account when vehicles are compared. The top speed of a vehicle is the highest constant cruising speed that the vehicle can achieve at full power on a level road. This means that the top speed is calculated when the maximum traction power P_{MAX} and the aerodynamic and rolling losses are at equilibrium.

$$P_{MAX} = P_w + P_r \tag{1.28}$$

Since there is no vehicle acceleration and road gradient, the grading loss and every energy kinetic contributions (rotational ones included) are set to zero.

There is also another constraint involving the maximum motor speed ω_{MAX} and the gear ratio r. The following expression relates the two parameters and

the EV top speed v_{top} in km/h.

$$v_{top} = \frac{2\,\pi \cdot \omega_{MAX} \cdot 0.06}{r}\,R \tag{1.29}$$

where ω_{MAX} is in rpm and the tire radius is in m.

For example, the 175/65 R15 and 195/50 R16 are two common tire sizes whose radius is approximately 0.3 m. As well known, 15 and 16 are the rim diameters expressed in inches, 175 and 195 are the nominal width of tire in mm while 65 and 50 are the percentage ratio of height to width.

$$0.5\,(15\,\text{inch} + 2 \times 175\,\text{mm} \times 65\%) \simeq 0.5\,(16\,\text{inch} + 2 \times 195\,\text{mm} \times 50\%) = 0.3\,\text{m}$$

Assuming a $\omega_{MAX} = 10\,000$ rpm and $r = 7$, the top speed results:

$$v_{top} = \frac{2\,\pi \times 10\,000 \times 0.06}{7}\,0.3 \simeq 160\,\text{km/h}$$

In summary, for a given set of vehicle data (such as the total mass m, the tire radius R, the wheels moment of inertia I_{wh}, the rolling resistance coefficient f_r, the aerodynamic drag coefficient C_d and the frontal area A), the main motor ratings T_{MAX}, P_{MAX}, ω_b, ω_{MAX} together with the gearbox ratio r determine the EV performances. However tradeoffs and constraints exist between these parameters.

In order to reduce the acceleration time, the product $T_{MAX} \cdot r$ can be set to the tire-road adhesion limit, then it remains only to boost the P_{MAX} and reduce ω_b, remembering that $P_{MAX} = \omega_b \cdot T_{MAX}$. By increasing r, the T_{MAX} of the motor can be relaxed. A first gear ratio upper bound comes from the rotor moment of inertia referred to the wheels: I_{rot} has to be multiplied by r^2, so a too high value for the gear ratio can degrade acceleration performances.

In addition, the motor P_{MAX} must be at least larger than $P_w + P_r$ at the vehicle top speed. Finally the vehicle top speed is also function of the ratio ω_{MAX}/r and this leads to a second, usually stricter, upper bound for the gearbox ratio.

Some examples of gear ratios used in HEVs and EVs are reported in Tab. 1.1. It can be observed that HEVs (e.g., Prius and LS 600h) have lower

Table 1.1: Some examples of gear ratios for HEV and EV.

Symbol	**Prius**	**LS 600h**	**i3**	**Accord**	**Bolt**	**LEAF**
r	3.27	$1.9 \div 3.9$	9.7	8.38	7.05	7.94

values [17, 18] as they work together with the ICE, whereas the plug-in series hybrids and EVs with range extenders, such as BMW i3 [19] and Honda Accord [7], adopt rather high ratios (near 10). Battery EVs, like Chevy Bolt and Nissan LEAF, use slightly lower values (between 7 and 8). Two gear ratio values are reported in Tab. 1.1 for the LS 600h as its sophisticated Ravigneaux gear system provides two gears.

Chapter 2

State of the Art in the automotive industry

In this chapter examples of IPM motors for HEV and EV traction will be examined in order to study the most important design options and trends. Tab. 2.1 reports an overview of the main motors available on the market with their specifications [17, 18, 19].

The next sections will focus the analysis on two interesting case studies: the 2010 Toyota Prius and the 2008 Lexus LS 600h motors. Although both are IPM machines for HEVs and were developed some years ago, the design solutions adopted in these two motors are still competitive. In addition, detailed data can be found for Prius and LS 600h, thus enabling more accurate conclusions. The analysis is carried out by means of Finite Element (FE) simulations [20] and analytical methods.

Looking at Tab. 2.1 some preliminary observations may be done. All the considered motors have three phases in wye configuration. The number of pole pairs p is rather high (four or more) and the number q of slots per pole and phase is always two.

$$q = \frac{Q_s}{2p \cdot m} \tag{2.1}$$

Table 2.1: Examples of IPM traction motors for (H)EV: 2010 Toyota Prius, 2008 Lexus LS 600h (among the HEVs), 2016 BMW i3, 2014 Chevrolet Volt (series HEV or EV with range extender), 2017 Chevrolet Bolt, 2016 Nissan LEAF (Battery EV) [17, 18, 19].

Symbol	**Prius**	**LS 600h**	**i3**	**Volt**	**Bolt**	**LEAF**	**Units**
P_{max}	60	165	125	150	150	80	kW
T_{max}	207	300	250	170	360	280	N m
ω_{max}	13 500	10 230	11 400	10 000	8 810	10 390	rpm
V_{bus}	650	650	360	700	360	375	V
m	3	3	3	3	3	3	#
p	4	4	6	5	-	4	#
Q_s	48	48	72	60	-	48	#
D_e	264	200	242.1	-	-	198.12	mm
D	161.9	130.86	180	-	-	130.96	mm
g	0.73	0.89	0.7	-	-	0.5	mm
D_r	160.44	129.08	178.6	-	-	129.97	mm
D_a	51	53	-	-	-	44.45	mm
L_{stk}	50.8	135.4	132.3	-	-	151.38	mm
n_c	11	7	9	4	-	6	#
n_{pp}	1	2	6	-	-	2	#
n_{cc}	12	9	12	-	-	20	#
d_c	0.812	0.812	0.723	-	-	0.812	mm
d_c	20	20	21	-	-	20	AWG
N_{sc}	8	4	1	-	-	4	#
L_{lam}	0.305	0.28	-	-	-	0.3	mm
$PMs/2p$	2	3	2	4	-	3	#
$G_{Fe\,stat}$	10.36	15.15	13.7	-	-	-	kg
$G_{Fe\,rot}$	6.7	11.93	14.2	-	-	16.45	kg
G_{Cu}	4.93	3.59	7.1	-	-	-	kg

Since q is even, B-type windings with short coils are possible. These motors use a full-pitch single layer winding arrangement, except the Volt which has a double-layer hairpin winding. Typically, low losses thin laminations are preferred, such as M250-35A or M270-35A, as the excitation frequency is relatively high due to the maximum speed and the significant pole number. Finally, most IPM traction motors for (H)EVs use NdFeB permanent magnets.

2.1 General parameters

From the Tab. 2.1, the following parameters can be derived: the slot pitch α_s, p_s, the pole pitch τ_p, the number of slots per pole y_q, the equivalent number of turn in series per slot n_{cs} and the series conductors per phase N_s.

$$y_q = \frac{Q_s}{2p} \tag{2.2}$$

$$n_{cs} = \frac{n_c}{n_{pp}} \tag{2.3}$$

$$N_s = \frac{n_{cs} \cdot Q_s}{m} \tag{2.4}$$

$$\alpha_s = \frac{360°}{Q_s} \tag{2.5}$$

$$p_s = \frac{\pi D}{Q_s} \tag{2.6}$$

$$\tau_p = \frac{\pi D}{2p} \tag{2.7}$$

Table 2.2: General parameters.

Symbol	Prius	LS 600h	i3	Volt	Bolt	LEAF	Units
y_q	6		6		-	6	#
q	2		2		-	2	#
α_s	7.5		5	6	-	7.5	deg.
p_s	10.6	8.56	7.85	-	-	8.57	mm
τ_p	63.58	51.39	47.12	-	-	51.43	mm
n_{cs}	11	3.5	1.5	-	-	3	#
N_s	176	56	36	-	-	48	#

As shown in Tab. 2.2, some parameters, especially those related to the

stator geometry (i.e., y_q, q, α_s, p_s, τ_p) exhibit rather limited variations, while the winding related parameters (n_{cs} and N_s) have larger differences. However, the next section deals with the winding study more in depth.

Fig. 2.1 shows the CAD geometry cross sections of the Prius and LS 600h motors used for the FE simulations henceforth. These drawings are based on the data in Tab. 2.1 supplemented by Tab. 2.3.

Table 2.3: Additional details.

Symbol	**Prius**	**LS 600h**	**Units**
h_{bi}	18.27	13.44	mm
w_t	7.5	6	mm
h_s	30.9	19.25	mm
w_{so}	1.88	1.88	mm
h_m	7.16	3.05	mm
w_m	17.88	18.7	mm

In order to take into account the slotting effect on the magnetic field lines, the Carter's coefficient k_c is computed.

$$k_c = \frac{p_s}{p_s + g - \frac{3}{4} w_{so}} \tag{2.8}$$

The coefficient therefore results: $k_c = 1.0686$ for Prius and $k_c = 1.0646$ for LS 600h, so the effective airgap becomes $g' = k_c \cdot g$.

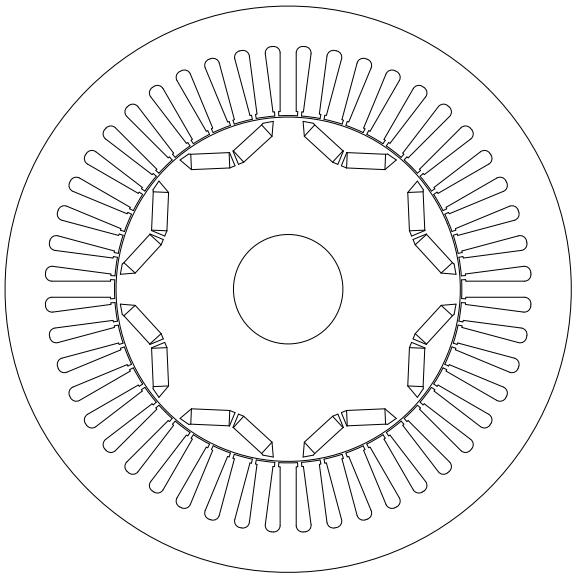

(a) Toyota Prius.

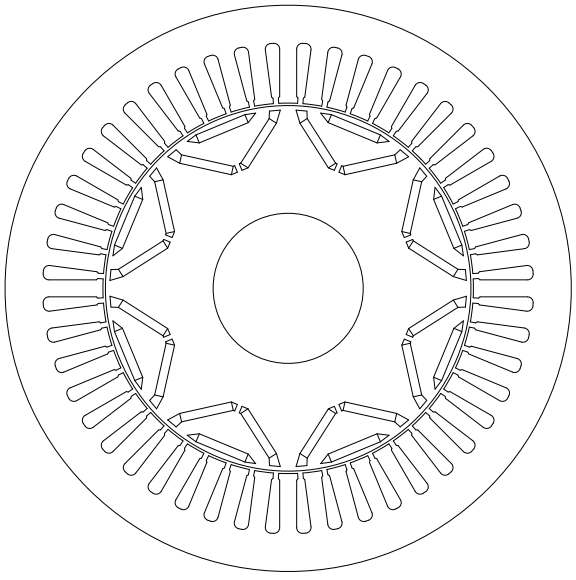

(b) Lexus LS 600h.

Figure 2.1: Scaled-down Prius and LS 600h cross section CAD geometries.

2.2 Windings

As the Prius and LS 600h motors adopt a full-pitch winding scheme, the angle of short pitch β_r^e, that is the angle in electrical degrees by which the coils can be short pitched, is $\beta_r^e = 0$ and the pitch factor [21, 15] is $k_p = 1$.

$$k_d = \frac{\sin\left(q\,\frac{\alpha_s^e}{2}\right)}{q \cdot \sin\left(\frac{\alpha_s^e}{2}\right)} \qquad (2.9) \qquad\qquad k_p = \cos\left(\frac{\beta_r^e}{2}\right) \qquad (2.10)$$

Then, the winding factor $k_w = k_d \cdot k_p$ for these two motors coincides with the distribution factor $k_d = k_w = 0.9659$. Clearly, $\alpha_s^e = p\,\alpha_s$. The two winding schemes are depicted in Fig. 2.2. Every coil is numbered in the circles, and the starting point is denoted with S as well as the end point E or the neutral N. In Fig. 2.2b and 2.3 each of the two "legs" are highlighted in red and blue respectively.

Now, the cross section surfaces of the winding have to be defined: S_{1c}, the cross section surface of the single copper wire; S_c, the cross surface of one conductor in the slot; $S_{c\,eq}$, an equivalent single serial conductor cross surface accounting for the parallel path number; and S_{Cu}, the copper part of the slot cross surface.

$$S_{1c} = \frac{\pi}{4}\,d_c^2 \qquad (2.11) \qquad\qquad S_{c\,eq} = n_{pp} \cdot S_c \qquad (2.13)$$

$$S_c = n_{cc} \cdot S_{1c} \qquad (2.12) \qquad\qquad S_{Cu} = n_c \cdot S_c \qquad (2.14)$$

Making the assumption of trapezoidal shape for the sake of simplicity, the total cross section surface of the slot S_{slot} can be found:

$$S_{slot} = w_{so}\,h_s + \frac{\pi}{Q_s}\,h_s^2 \qquad (2.15)$$

So, the ratio between (2.14) and (2.15) yields the fill factor k_{fill} of the stator slots.

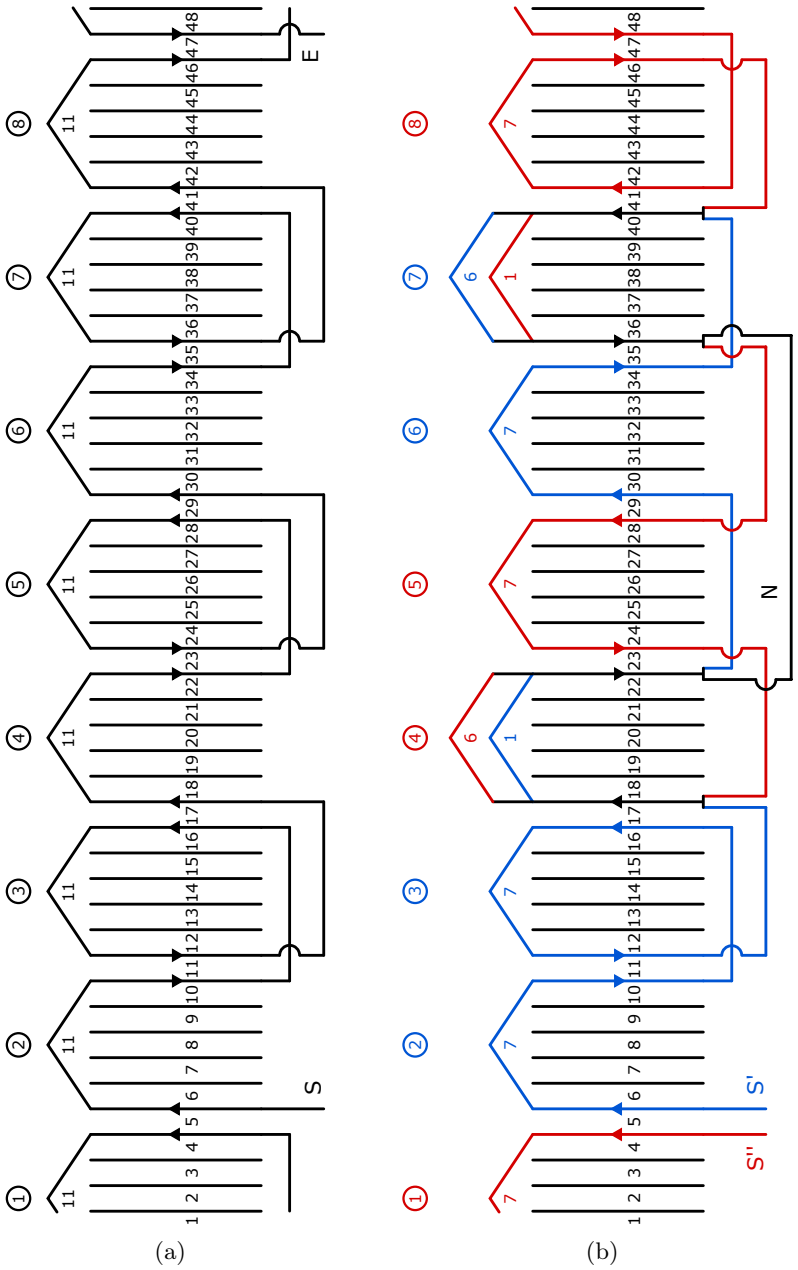

Figure 2.2: Winding arrangements of: Prius (a) and LS 600h (b).

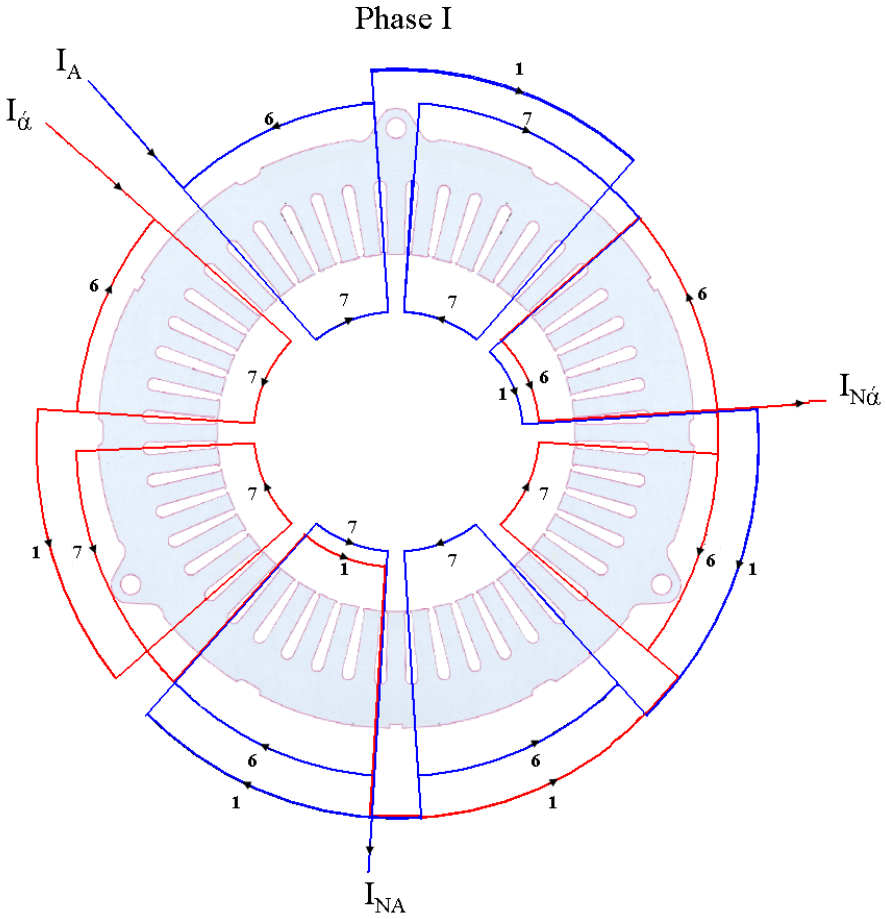

Figure 2.3: Circular winding scheme of the LS 600h [18].

$$k_{fill} = \frac{S_{Cu}}{S_{slot}} \tag{2.16}$$

At this point, all the elements necessary to study the current densities in the motor windings are available.

$$J_s = \frac{\hat{I}/\sqrt{2}}{S_{c\,eq}} \tag{2.17}$$

$$\widehat{K}_s = \frac{3\,k_w\,N_s}{\pi D}\hat{I} \tag{2.18}$$

J_s is the *surface* current density, while $\widehat{K}_s$ is the *linear* current density or electrical loading of the machine. These parameters are directly related with the motor torque capabilities and ohmic losses. Comparing the motors current densities with the standard values can also give information about how much demanding are the torque and power ratings of the machine.

Another important winding parameter is the phase resistance R_{ph}.

$$R_{ph} = \rho\,\frac{N_s\,L_c}{S_{c\,eq}} \tag{2.19}$$

Phase resistance is function of the resistivity $\rho = \rho_{20\,^\circ\mathrm{C}}\,(1 + \alpha \cdot \Delta T)$ and of the total single conductor length L_c. Copper resistivity at 20 °C is $\rho_{20\,^\circ\mathrm{C}} = 0.018\ \Omega\,\mathrm{mm}^2\,\mathrm{m}^{-1}$ and the resistance temperature coefficient $\alpha = 0.004\ ^\circ\mathrm{C}^{-1}$. The term $\Delta T = T - 20\ ^\circ\mathrm{C}$ stands for the temperature difference from 20 °C.

The length of each winding conductor ($L_c = L_{stk} + L_{ew}$) comprises an active part L_{stk} in the slots and an end-winding L_{ew} part. In order to find the analytic relationship for L_{ew}, a geometry assumption has to be made. The following expression is based on the circular assumption, which typically gives values in good agreement with the experimental results.

$$L_{ew} = \frac{\pi \cdot \tau_p}{2} \simeq 1.6 \cdot \tau_p \simeq 2.5\,\frac{D}{p} \tag{2.20}$$

Finally, the overall copper volume and mass can be estimated as follows.

$$Vol_{Cu} = Q_s\,n_{cs}\,S_{c\,eq}\,L_c \tag{2.21}$$

$$G_{Cu} = \gamma_{Cu} \cdot Vol_{Cu} \tag{2.22}$$

where $\gamma_{Cu} = 8900\ \mathrm{kg\,m^{-3}}$ is the copper volumetric mass density.

All the parameters above have been computed in Tab. 2.4.

Table 2.4: Computed winding parameters summary.

Symbol	Prius		LS 600h		Units
	$\hat{\mathrm{I}} = 120\,\mathrm{A}$	$\hat{\mathrm{I}} = 180\,\mathrm{A}$	$\hat{\mathrm{I}} = 250\,\mathrm{A}$	$\hat{\mathrm{I}} = 400\,\mathrm{A}$	
k_p	1		1		#
k_d	0.9659		0.9659		#
k_w	0.9659		0.9659		#
L_{ew}	101.2		81.8		mm
L_c	152		217.2		mm
S_{1c}	0.5179		0.5179		$\mathrm{mm^2}$
S_c	6.215		4.661		$\mathrm{mm^2}$
$S_{c\,eq}$	6.215		9.322		$\mathrm{mm^2}$
S_{Cu}	68.36		32.63		$\mathrm{mm^2}$
S_{slot}	120.58		60.44		$\mathrm{mm^2}$
k_{fill}	0.57		0.54		#
R_{ph} (@ 20 °C)	77.5		23.5		mΩ
J_s	13.6	20.5	19	30.34	$\mathrm{A\,mm^{-2}}$
$\widehat{K}_s$	120.32	180.48	98.68	157.89	$\mathrm{A\,mm^{-1}}$
Vol_{Cu}	498 740		340 150		$\mathrm{mm^3}$
G_{Cu}	4.44		3.03		kg

2.3 Magnetic analytical model

According to the angle convention depicted in Fig. 2.4, any angular position (the green vector) can be identified by means of two different angular coordinates: θ, related to the stator *abc* reference frame and θ_r, associated with the

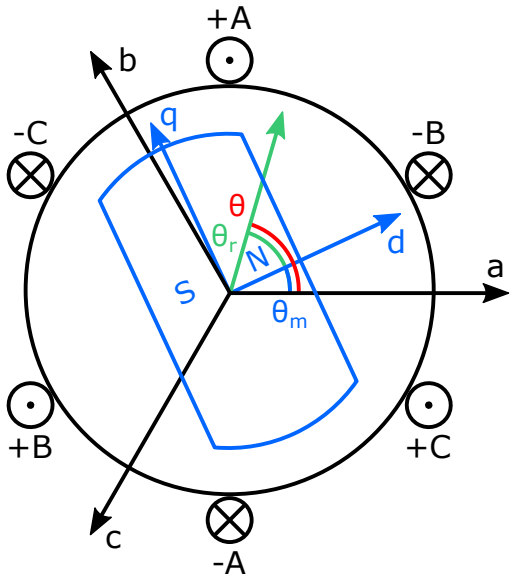

Figure 2.4: Angles convention.

rotor dq reference frame. The rotor angular position θ_m connects these two reference frames through the relationship $\theta = \theta_r + \theta_m$.

In addition, recalling the current angle α_i^e definition in Fig. 1.3, the synchronous motor three phase currents can be expressed as follows [16].

$$\begin{cases} i_a = \hat{I} \cdot \cos\left(p\,\theta_m + \alpha_i^e\right) \\ i_b = \hat{I} \cdot \cos\left(p\,\theta_m + \alpha_i^e - \dfrac{2\pi}{3}\right) \\ i_c = \hat{I} \cdot \cos\left(p\,\theta_m + \alpha_i^e - \dfrac{4\pi}{3}\right) \end{cases} \tag{2.23}$$

The machine current load therefore results

$$K_s\left(\theta_r^e\right) = \widehat{K}_s \cdot \sin\left(\theta_r^e - \alpha_i^e\right) = \widehat{K}_s \cdot \sin\left(\theta^e - \theta_m^e - \alpha_i^e\right) \tag{2.24}$$

whose modulus $\widehat{K}_s$ has been defined in (2.18). As the other machine electrical quantities, the current load can be broken down in the d-axis and q-axis terms, by setting α_i^e to 0 and $\pi/2$ respectively.

$$\alpha_i^e = 0 \quad \Longrightarrow \quad K_{sd}(\theta_r) = \widehat{K}_{sd} \cdot \sin(p\,\theta_r) \tag{2.25}$$

$$\alpha_i^e = \frac{\pi}{2} \quad \Longrightarrow \quad K_{sq}(\theta_r) = -\widehat{K}_{sq} \cdot \cos(p\,\theta_r) \tag{2.26}$$

Multiplying $\widehat{K}_s$ by $\cos\alpha_i^e$ and $\sin\alpha_i^e$ gives the $\widehat{K}_{sd}$ and $\widehat{K}_{sq}$ moduli respectively.

$$\begin{aligned} \widehat{K}_{sd}(\alpha_i^e) &= \frac{3\,k_w\,N_s}{\pi D} \cdot \hat{I}\cos\alpha_i^e \\ \widehat{K}_{sq}(\alpha_i^e) &= \frac{3\,k_w\,N_s}{\pi D} \cdot \hat{I}\sin\alpha_i^e \end{aligned} \tag{2.27}$$

In conjunction with the magnetic loading B (i.e., the airgap magnetic flux density), the electrical loading K links the motor torque with the active volume. $\widehat{B}_{gm}$ is the PM-only component of the magnetic loading, whereas $\widehat{B}_{sd}$ and $\widehat{B}_{sq}$ are respectively the d-axis and q-axis magnetic loading terms related to the stator armature reaction.

$$T = \left[\left(\widehat{B}_{gm} + \widehat{B}_{sd}\right) \cdot \widehat{K}_{sq} - \widehat{B}_{sq} \cdot \widehat{K}_{sd}\right] \left(\frac{\pi}{4} D^2 L_{stk}\right) \tag{2.28}$$

Observing (2.28) the mutual and reluctance torque components can be simply isolated.

$$\begin{aligned} T_{PM} &= \widehat{B}_{gm} \cdot \widehat{K}_{sq} \cdot \left(\frac{\pi}{4} D^2 L_{stk}\right) \\ T_{rel} &= \left(\widehat{B}_{sd}\,\widehat{K}_{sq} - \widehat{B}_{sq}\,\widehat{K}_{sd}\right) \left(\frac{\pi}{4} D^2 L_{stk}\right) \end{aligned} \tag{2.29}$$

2.3.1 Magnetic circuit in the d/q reference frame

In order to determine all the magnetic loading components, the motor magnetic circuit has to be solved. The complexity of this analysis grows with the number

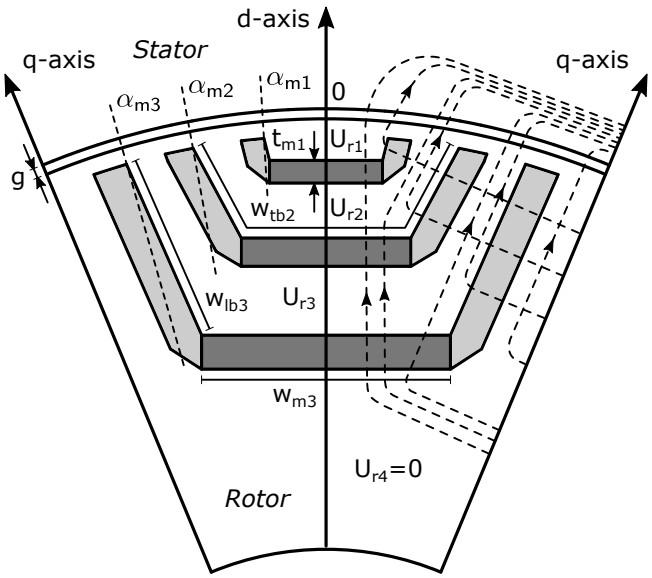

Figure 2.5: Single pole rotor magnetic circuit with multiple barriers. PMs are in dark grey, air is light grey.

of flux barriers in the rotor. However, making some simplifying assumptions including linearity, a closed-form general model based on a small set of recursive equations has been developed [22]. In particular, the proposed model describes each flux barrier with only two parameters (see Fig. 2.5): the angular width (at the airgap) $\alpha_{m\,i}$ and the ASR_i, that is an "aggregate variable" defined as $ASR_i = AS_{tb\,i}/AS_{g\,i}$, where $AS_{tb\,i} = \mu_{rec} \cdot (w_{m\,i} + 2\,w_{lb\,i})/t_{m\,i}$ is the aspect ratio of the total *i-th* flux barrier, and $AS_{g\,i} = (D/2)(2\,\alpha_{m\,i})/g$ is the aspect ratio of the airgap portion covered by $\alpha_{m\,i}$. w_m, t_m, w_{lb} and t_{lb} are respectively the width and the thickness of the PM and the lateral (air) barriers. μ_{rec} is the relative recoil permeability ($\simeq 1$ for rare-earth PMs).

In the IPM and synchronous reluctance electric machines, the presence of the n rotor flux barriers alters both the d-axis flux density distribution at the airgap related to the stator linear current density $B_{sd}(\theta_r)$ and that in no-load conditions $B_{gm}(\theta_r)$. Therefore, in order to compute the d-axis flux linkage,

inductance and the saliency ratio, it is necessary to determine the specific behavior of $B(\theta_r)$ under each rotor island.

The $B_{sd}(\theta_r)$ mathematical description needs a piecewise function due to the above considerations.

$$B_{sd}(\theta_r) = \begin{cases} B_{sd\,1}(\theta_r) & -\alpha_{m1} \leqslant \theta_r \leqslant +\alpha_{m1} \\ B_{sd\,i}(\theta_r) & -\alpha_{m\,i} \leqslant \theta_r < -\alpha_{m\,(i-1)} \\ & \text{or} \\ & +\alpha_{m\,(i-1)} < \theta_r \leqslant +\alpha_{m\,i} \\ B_{sd\,(n+1)}(\theta_r) & -\frac{\pi}{2p} \leqslant \theta_r < -\alpha_{m\,n} \\ & \text{or} \\ & +\alpha_{m\,n} < \theta_r \leqslant +\frac{\pi}{2p} \end{cases} \tag{2.30}$$

Here the n barriers are numbered from the inner to the outer, i.e. the lowest index refers to the barrier which is nearest to the surface. The $(n+1)$ terms denote the rotor areas between adjacent poles, out of the last flux barrier. Recalling [16], every $B_{sd\,i}(\theta_r)$ term in (2.30) is a function of the stator magnetic potential $U_{sd}(\theta_r)$ and the rotor island magnetic potential $U_{r\,i}$.

$$B_{sd\,i}(\theta_r) = \frac{\mu_0}{g}[U_{r\,i} - U_{sd}(\theta_r)] \tag{2.31}$$

$$B_{sd\,(n+1)}(\theta_r) = -\frac{\mu_0}{g} \cdot U_{sd}(\theta_r) \tag{2.32}$$

where μ_0 is the permeability of free space. While $U_{sd}(\theta_r)$ comes directly from the application of Ampere's law to the d-axis linear current density expression $K_{sd}(\theta_r)$ (2.25), the $U_{r\,i}$ calculation is not so straightforward.

$$U_{sd}(\theta_r) = \int K_{sd}(\theta'_r)\frac{D}{2}d\theta'_r = -\frac{\widehat{K}_{sd}D}{2p}\cos(p\,\theta_r) \tag{2.33}$$

The $U_{r\,i}$ values are the result of the balance between the magnetic flux

entering and that leaving each rotor island.

$$\begin{cases} \phi_{sd1} = \phi_{m1} + 2\,\phi_{lb1} \\ \phi_{sd1} + \phi_{sd2} = \phi_{m2} + 2\,\phi_{lb2} \\ \dots \\ \sum_{i=1}^{n} \phi_{sd\,i} = \phi_{m\,n} + 2\,\phi_{lb\,n} \end{cases} \tag{2.34}$$

The system (2.34) represents a convenient way to write the Gauss equations of the rotor, where $\phi_{sd\,i}$ is the magnetic flux flowing through the airgap portion of *i-th* island, $\phi_{m\,i}$ is the flux from the PM of the *i-th* island and $\phi_{lb\,i}$ is the flux which passes through each of two lateral segments in the *i-th* barrier. From (2.31) and (2.32), results:

$$\begin{aligned} \phi_{sd1} &= \int_{-\alpha_{m1}}^{+\alpha_{m1}} B_{sd1}(\theta'_r)\frac{D\,L_{stk}}{2}d\theta'_r \\ &= \frac{\mu_0 D\,L_{stk}}{g\cdot p}\left[U_{r1}\,\alpha^e_{m1} + \frac{\widehat{K}_{sd}D}{2p}\sin(\alpha^e_{m1})\right] \end{aligned} \tag{2.35}$$

$$\begin{aligned} \phi_{sd\,i} &= 2\cdot\int_{+\alpha_{m\,(i-1)}}^{+\alpha_{m\,i}} B_{sd\,i}(\theta'_r)\frac{D\,L_{stk}}{2}d\theta'_r \\ &= \frac{\mu_0 D\,L_{stk}}{g\cdot p}\Big\{U_{r\,i}\cdot(\alpha^e_{m\,i} - \alpha^e_{m\,(i-1)}) + \\ &+ \frac{\widehat{K}_{sd}D}{2p}[\sin(\alpha^e_{m\,i}) - \sin(\alpha^e_{m\,(i-1)})]\Big\} \end{aligned} \tag{2.36}$$

$$\begin{aligned} \phi_{sd\,(n+1)} &= 2\cdot\int_{+\alpha_{m\,n}}^{+\frac{\pi}{2p}} B_{sd\,(n+1)}(\theta'_r)\frac{D\,L_{stk}}{2}d\theta'_r \\ &= \frac{\mu_0 D^2\,L_{stk}\,\widehat{K}_{sd}}{2p^2\,g}[1 - \sin(\alpha^e_{m\,n})] \end{aligned} \tag{2.37}$$

For the PMs and the lateral segments of the *i-th* barrier expressions similar to (2.31), (2.32) and (2.36), (2.37) exist.

$$\phi_{m\,i} = \frac{\mu_{rec}\,\mu_0}{t_{m\,i}}(U_{r\,(i+1)} - U_{r\,i})\,w_{m\,i}\,L_{stk} \tag{2.38}$$

$$\phi_{lb\,i} = \frac{\mu_0}{t_{lb\,i}}(U_{r\,(i+1)} - U_{r\,i})\, w_{lb\,i}\, L_{stk} \tag{2.39}$$

where B_{rem} is the PM remanent flux density. Substituting (2.35)–(2.39) in (2.34) and adopting the proposed symbolic formalism, leads to a system of linear equations where the $U_{r\,i}$ are the unknown variables.

$$\begin{bmatrix} \alpha^e_{m1} + ASR_1\,\alpha^e_{m1} & -ASR_1\,\alpha^e_{m1} & 0 & 0 \\ \alpha^e_{m1} & \alpha^e_{m2} - \alpha^e_{m1} + ASR_2\,\alpha^e_{m2} & -ASR_2\,\alpha^e_{m2} & 0 \\ \alpha^e_{m1} & \alpha^e_{m2} - \alpha^e_{m1} & \alpha^e_{m3} - \alpha^e_{m2} + ASR_3\,\alpha^e_{m3} & -ASR_3\,\alpha^e_{m3} \\ \alpha^e_{m1} & \alpha^e_{m2} - \alpha^e_{m1} & \alpha^e_{m3} - \alpha^e_{m2} & \alpha^e_{m4} - \alpha^e_{m3} + ASR_4\,\alpha^e_{m4} \end{bmatrix} \cdot \begin{bmatrix} U_{r1} \\ U_{r2} \\ U_{r3} \\ U_{r4} \end{bmatrix} = \begin{bmatrix} -\frac{D\,\widehat{K}_{sd}}{2p}\sin(\alpha^e_{m1}) \\ -\frac{D\,\widehat{K}_{sd}}{2p}\sin(\alpha^e_{m2}) \\ -\frac{D\,\widehat{K}_{sd}}{2p}\sin(\alpha^e_{m3}) \\ -\frac{D\,\widehat{K}_{sd}}{2p}\sin(\alpha^e_{m4}) \end{bmatrix} \tag{2.40}$$

Equation 2.40 shows a four barrier example: repetitive patterns are clearly visible and the system could be written directly from the machine parameters.

As it is well known, the matrix equivalent form of a linear system $\underline{A} \cdot \underline{x} = \underline{b}$ can be decomposed in an upper $\underline{U}$ and a lower $\underline{L}$ triangular matrices by means of the LU factorization. In this way, the original system is split in two new systems which can be solved respectively with forward and backward substitution.

$$\underline{L} \cdot \underline{U} \cdot \underline{x} = \underline{b} \quad \Longrightarrow \quad \begin{cases} \underline{L} \cdot \underline{y} = \underline{b} \\ \underline{U} \cdot \underline{x} = \underline{y} \end{cases} \tag{2.41}$$

The four barrier example $\underline{A}$ matrix in (2.40) is decomposed as follows.

$$\underline{L} = \begin{bmatrix} 1 & 0 & 0 & 0 \\ P_0 & 1 & 0 & 0 \\ P_0 & P_1 & 1 & 0 \\ P_0 & P_1 & P_2 & 1 \end{bmatrix} \tag{2.42}$$

$$\underline{U} = \begin{bmatrix} (1 + ASR_1)\,\alpha^e_{m1} & -ASR_1\,\alpha^e_{m1} & 0 & 0 \\ 0 & F_0 & -ASR_2\,\alpha^e_{m2} & 0 \\ 0 & 0 & F_1 & -ASR_3\,\alpha^e_{m3} \\ 0 & 0 & 0 & F_2 \end{bmatrix} \tag{2.43}$$

where

$$P_0 = \frac{1}{1 + ASR_1} \tag{2.44}$$

$$P_i = \frac{\alpha^e_{m\,(i+1)} - \alpha^e_{m\,i} \cdot (1 - ASR_i\,P_{(i-1)})}{\alpha^e_{m\,(i+1)} \cdot (1 + ASR_{(i+1)}) - \alpha^e_{m\,i} \cdot (1 - ASR_i\,P_{(i-1)})} \tag{2.45}$$

As inductive reasoning suggests, the $\underline{L}$ and $\underline{U}$ structures are scalable with a general number of flux barriers. Therefore, combining these scaling rules with the forward and backward substitution algorithm, a recursive closed-form expression for the rotor islands magnetic potentials $U_{r\,i}$ is found.

$$U_{r1} = \frac{ASR_1}{1 + ASR_1} \cdot U_{r2} + \frac{y_1}{(1 + ASR_1)\,\alpha^e_{m1}} \tag{2.46}$$

$$U_{r\,i} = \frac{ASR_i\,\alpha^e_{m\,i}}{F_{(i-2)}} \cdot U_{r\,(i+1)} + \frac{y_i}{F_{(i-2)}} \tag{2.47}$$

$$U_{r\,n} = \frac{y_n}{F_{(n-2)}} \tag{2.48}$$

$$U'_{r\,i} = \frac{8p}{\widehat{K}_{sd}\,D\,\pi}\,U_{r\,i} \tag{2.49}$$

where

$$F_i = \alpha^e_{m\,(i+2)} \cdot (1 + ASR_{(i+2)}) - \alpha^e_{m\,(i+1)} \cdot (1 - ASR_{(i+1)}\,P_i) \tag{2.50}$$

$$y_i = -\frac{D\,\widehat{K}_{sd}}{2p}\left[\sin(\alpha^e_{m\,i}) - \sum_{l=1}^{i-1} P_{(i-1-l)} \cdot \sin(\alpha^e_{m\,(i-l)}) \cdot \prod_{u=1}^{i-2}(1 - P_u)\right] \tag{2.51}$$

Equations (2.44)–(2.45) and (2.50)–(2.51) are auxiliary expressions.

2.3.2 Expression of the saliency ratio

By means of the three formulas (2.46)–(2.48), it is possible to write the scalar magnetic potential of each rotor island, starting from the first (2.46) up to the last (2.48). For the others, $2 \leqslant i < n$, (2.47) has to be used. There is no need to carry out any matrix computation again since it is incorporated in this small set of equations. By means of recursion, this set of equations has the power to yield the solution of the rotor magnetic circuit with an unlimited number n of flux barriers. This means that knowing the $U_{r\,i}$ potentials, the $B_{sd}(\theta_r)$ and every other related machine parameter is determined (2.30), such as the d-axis flux linkage, inductance and the saliency ratio ξ. $\widehat{K}_{sd}$ is the amplitude of the full d-axis linear current density, expressed in (A/m).

$$\xi = \left\{1 + U'_{r1}\sin(\alpha^e_{m1}) + \sum_{i=2}^{n} U'_{r\,i}\,[\sin(\alpha^e_{m\,i}) - \sin(\alpha^e_{m\,(i-1)})]\right\}^{-1} \tag{2.52}$$

Applying the normalization (2.49) to the magnetic potentials, the saliency ratio ξ results in (2.52).

By means of (2.52) the motor d-axis inductance can be determined whereas the q-axis inductance is not affected by the flux barriers, so it is not function of ASR_i nor $\alpha_{m\,i}$.

$$L_d = \frac{3}{\pi}\,\mu_0 \left(\frac{k_w N_s}{2p}\right)^2 \frac{D\,L_{stk}}{g'} \cdot \frac{1}{\xi} \tag{2.53}$$

$$L_q = \frac{3}{\pi}\,\mu_0 \left(\frac{k_w N_s}{2p}\right)^2 \frac{D\,L_{stk}}{g'} \tag{2.54}$$

2.3.3 Permanent Magnet flux density distribution

So far, the equations have dealt with the current-fed motor but similar relationships can be written for the no-load condition.

$$U_{rm1} = \frac{ASR_1}{1 + ASR_1} \cdot U_{rm2} + \frac{y_{m\,1}}{(1 + ASR_1)\,\alpha^e_{m1}} \tag{2.55}$$

$$U_{rm\,i} = \frac{ASR_i\,\alpha^e_{m\,i}}{F_{(i-2)}} \cdot U_{rm\,(i+1)} + \frac{y_{m\,i}}{F_{(i-2)}} \tag{2.56}$$

$$U_{rm\,n} = \frac{y_{m\,n}}{F_{(n-2)}} \tag{2.57}$$

where

$$y_{m\,i} = \frac{B_{rem}}{\mu_0} \left[\frac{\alpha^e_{m\,i}\,w_{m\,i}}{AS_{g\,i}} - \sum_{l=1}^{i-1} P_{(i-1-l)} \cdot \frac{\alpha^e_{m\,(i-l)}\,w_{m\,(i-l)}}{AS_{g\,(i-l)}} \cdot \prod_{u=1}^{i-2} (1 - P_u)\right] \tag{2.58}$$

The main difference between the set (2.55)–(2.57) and (2.46)–(2.48) is that for the first one, (2.58) has to be used instead of (2.51). As in the previous case, the $U_{rm\,i}$ values determine the airgap flux density distribution, this time in

no-load condition.

$$B_{gm}(\theta_r) = \begin{cases} B_{gm1} = \dfrac{\mu_0}{g'} U_{rm1} & -\alpha_{m1} \leqslant \theta_r \leqslant +\alpha_{m1} \\ B_{gm\,i} = \dfrac{\mu_0}{g'} U_{rm\,i} & \begin{array}{c} -\alpha_{m\,i} \leqslant \theta_r < -\alpha_{m\,(i-1)} \\ \text{or} \\ +\alpha_{m\,(i-1)} < \theta_r \leqslant +\alpha_{m\,i} \end{array} \\ 0 & \begin{array}{c} -\frac{\pi}{2p} \leqslant \theta_r < -\alpha_{m\,n} \\ \text{or} \\ +\alpha_{m\,n} < \theta_r \leqslant +\frac{\pi}{2p} \end{array} \end{cases} \tag{2.59}$$

The amplitude of the airgap flux density fundamental tone in no-load operating conditions is:

$$\widehat{B}_{gm} = \frac{4}{\pi} \left\{ B_{gm1} \sin(\alpha^e_{m1}) + \sum_{i=2}^{n} B_{gm\,i} \left[\sin(\alpha^e_{m\,i}) - \sin(\alpha^e_{m\,(i-1)}) \right] \right\} \tag{2.60}$$

The Prius motor is a single layer IPM machine (see Fig. 2.6a), it means that the number of flux barriers n is one per pole. From the above formulas,

$$\widehat{B}_{gm} = \frac{B_{rem}}{g'} \cdot \frac{w_{m1} \cdot \frac{4}{\pi} \sin(\alpha^e_{m1})}{(1 + ASR_1)\, AS_{g\,1}} \tag{2.61}$$

$$\widehat{B}_{sd} = \frac{\mu_0}{g'} \cdot \frac{\widehat{K}_{sd} D}{2p} \left[1 - \frac{\frac{4}{\pi} \sin^2(\alpha^e_{m1})}{(1 + ASR_1)\, \alpha^e_{m1}} \right] \tag{2.62}$$

$$\widehat{B}_{sq} = \frac{\mu_0}{g'} \cdot \frac{\widehat{K}_{sq} D}{2p} \tag{2.63}$$

$$\xi = \frac{1}{1 - \frac{\frac{4}{\pi} \sin^2(\alpha^e_{m1})}{(1 + ASR_1)\, \alpha^e_{m1}}} \tag{2.64}$$

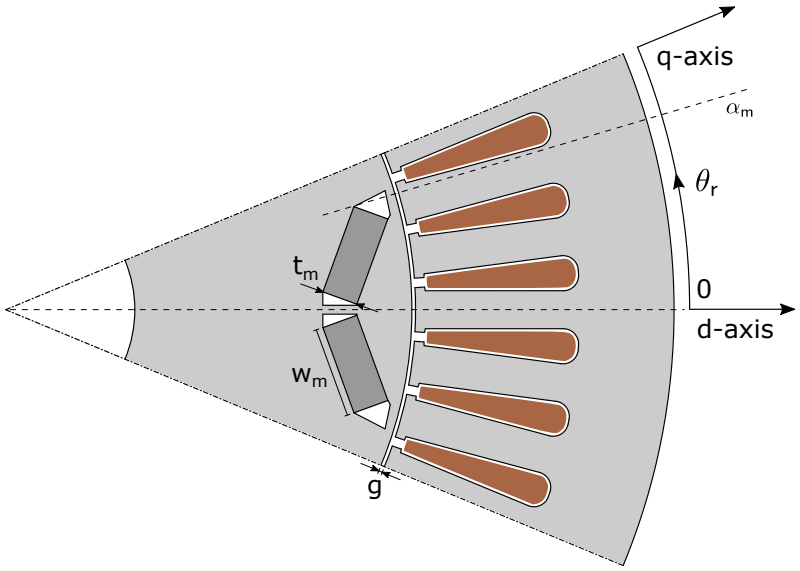

(a) Prius (single barrier).

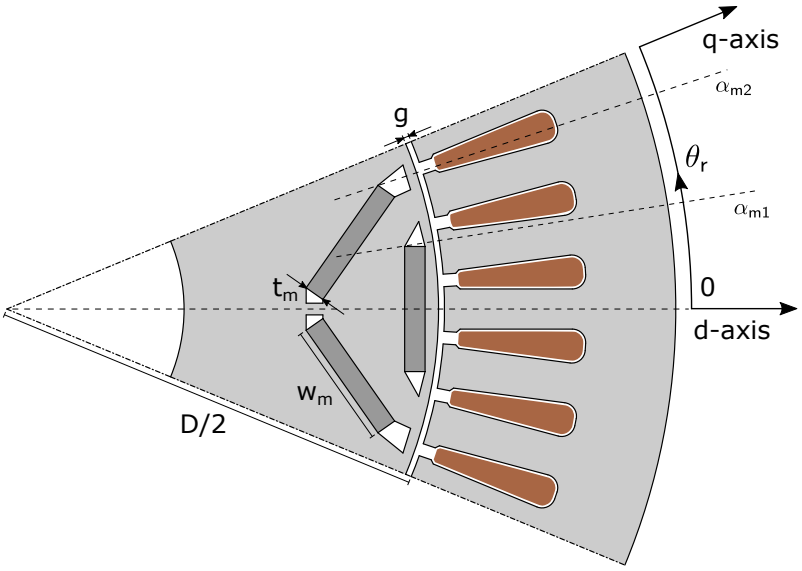

(b) LS 600h (two barriers).

Figure 2.6: One pole circular sector (illustrative drawing).

Setting $n = 2$, that is the LS 600h rotor topology (Fig. 2.6b), equations (2.46)–(2.48) take the following form.

$$U_{r1} = \frac{ASR_1}{1 + ASR_1} U_{r2} - \frac{\widehat{K}_{sd}\, D}{2p} \cdot \frac{\sin(\alpha^e_{m1})}{(1 + ASR_1)\, \alpha^e_{m1}} \tag{2.65}$$

$$U_{r2} = -\frac{\widehat{K}_{sd}\, D}{2p} \cdot \frac{\sin(\alpha^e_{m2}) - \dfrac{\sin(\alpha^e_{m1})}{1 + ASR_1}}{(1 + ASR_2)\, \alpha^e_{m2} - \dfrac{\alpha^e_{m1}}{1 + ASR_1}} \tag{2.66}$$

$$U_{rm1} = \frac{ASR_1}{1 + ASR_1} U_{rm2} + \frac{B_{rem}}{\mu_0} \cdot \frac{w_{m\,1}}{AS_{g\,1}} \frac{1}{1 + ASR_1} \tag{2.67}$$

$$U_{rm2} = \frac{B_{rem}}{\mu_0} \cdot \frac{\dfrac{\alpha^e_{m2}\, w_{m\,2}}{AS_{g\,2}} - \dfrac{\alpha^e_{m1}\, w_{m\,1}}{AS_{g\,1}} \cdot \dfrac{1}{1 + ASR_1}}{(1 + ASR_2)\, \alpha^e_{m2} - \dfrac{\alpha^e_{m1}}{1 + ASR_1}} \tag{2.68}$$

$$\xi = \left\{1 + U'_{r1} \sin(\alpha^e_{m1}) + U'_{r2} \cdot [\sin(\alpha^e_{m2}) - \sin(\alpha^e_{m1})]\right\}^{-1} \tag{2.69}$$

$$\widehat{B}_{gm} = \frac{4}{\pi} \left\{B_{gm1} \sin(\alpha^e_{m1}) + B_{gm2} \cdot [\sin(\alpha^e_{m2}) - \sin(\alpha^e_{m1})]\right\} \tag{2.70}$$

It is interesting to observe that the proposed equations are consistent also for the extreme theoretical values. For instance, in (2.65) two contributions can be recognized: the first term expresses the effect of the potential U_{r2} on the U_{r1}, whereas the second term represents its own potential (like in a single layer rotor). If the first barrier $i = 1$ was infinitely thick $t_{m1} = \infty$, then $ASR_1 = 0$ and the first term would disappear as if it was shielded by the barrier number 1. On the contrary, if the first barrier was removed $t_{m1} = 0$, then $ASR_1 = \infty$ and the second term would disappear resulting in $U_{r1} = U_{r2}$ as expected.

In other words, no trivial solution leads to the optimal rotor geometry, so its design process inherently involves a multi-objective optimization task. This topic will be discussed more deeply in the next chapter.

The current section aims to give sound theoretical basis for the performance analysis and the next chapter discusses about the main design options. The

linearity assumption prevents sufficiently accurate results to be obtained, thus the magnetic analysis has to be carried out with FE simulations [20].

The equations above give useful insights of the machine physical behavior to the designer and make possible to split the project, deferring the sizing of the specific elements while giving priority to the relative proportions of the flux barriers. First of all, the mathematical dependence of flux linkage from the aspect ratios of the flux barriers demonstrates that the effectiveness of these barriers is a function of their geometric proportions and only secondarily of the $\alpha_{m\,i}$ barrier angles as they typically appear in terms like $\sin(\alpha_{m\,i})/\alpha_{m\,i}$. On the contrary, the total harmonic distortion of the B_{gm} is mainly affected from the angles $\alpha_{m\,i}$ and the magnet widths $w_{m\,i}$, together with the B_{rem} of the selected PM. Moreover, no trivial sizing is possible in multiple barrier configurations because as evidenced by the scalar magnetic potentials $U_{r\,i}$ in each pole of the rotor, the different flux barriers influence each other and their individual effects on the overall reluctance are correlated. Hence, multi-objective optimization is mandatory. Finally, in order to reduce the B_{gm} spatial harmonics, the number of the flux barriers per pole has to be increased and the $\alpha_{m\,i}$ angles must be set properly, but if it is the saliency that needs to be improved, it may be preferable simply to increase the total thickness of the barriers instead of their number.

2.4 Performance and magnetic circuit analysis

In the following subsections, the Finite Elements Analysis (FEA) results of the two considered state-of-the-art motors, Prius and LS 600h (Fig. 2.6), are presented.

2.4.1 Magnetic characteristics

Figures 2.7–2.8 and 2.12–2.13 show the machine inductances of direct and quadrature axes, while in Figs. 2.9–2.10 the dq-frame flux linkages (including the PM magnetic flux) are illustrated. The currents amplitudes adopted for nominal and overload conditions are those reported in Tab. 2.4. Observing Figs. 2.9–2.10, the flux linkage dependency from both the i_d and i_q is clearly visible. Because of this phenomenon, called cross-saturation, there is an infinite number of possible $L_d(i_d)$ and $L_q(i_q)$ functions depending on the i_q and i_d respectively, therefore Figs. 2.12–2.13 comprise many curves. The cross-saturation effect is typical of this kind of motors since they are highly saturated.

Due to the elaborate rotor geometry, the L_q curves in Figs. 2.12b–2.13b are symmetrical, whereas L_d curves (Figs. 2.12a–2.13a) are not. For positive i_d, the rotor iron bridges initially desaturate, thus changing the machine magnetic circuit. Then, as $i_d > 0$ grows, the iron bridges saturate again with opposite sign magnetic flux. This leads to the inductance peak observable in Figs. 2.12a–2.13a. However, as explained in section 1.1, the IPM motors are always controlled with $i_d < 0$, so only the left half-plane in Figs. 2.12a–2.13a and second (motor) or third (generator) quadrants in Figs. 2.7a–2.8a are used.

As expected, it results that $L_d < L_q$ and L_q exhibits a more pronounced variation with the current, compared to L_d. The rotor flux barriers, in fact, reduce the magnetic flux related to the armature reaction along d-axis, respect to the q-axis. Additionally, in the q-axis path there is more iron, so the q-axis is more heavily affected by magnetic saturation. As a consequence of the different saturation levels along the dq-axes, the saliency ratio drops as the current

module rises. This effect gets worse increasing the saliency, hence in other words, the saliency ratio is someway "self-limited" and for this reason saturated ξ exceeds 6 very unlikely even if the number of flux barriers is increased ($\xi \simeq 10$ only with axially laminated rotors).

Table 2.5: Average saliency ratios summary.

Sal. ratio ξ	**Prius**		**LS 600h**	
	$\hat{\mathrm{I}} = 120\,\mathrm{A}$	$\hat{\mathrm{I}} = 180\,\mathrm{A}$	$\hat{\mathrm{I}} = 250\,\mathrm{A}$	$\hat{\mathrm{I}} = 400\,\mathrm{A}$
Saturated	2.25	1.96	2.59	2.36
Unsaturated	2.89		2.8	
Delta %	22.1 %	32.2 %	7.5 %	15.7 %

Table 2.5 reports a summary of the average saliency ratios simulated in maximum current conditions (saturated values) and with the 10 % of the overload maximum current (unsaturated values). Not very significant differences are detectable comparing the Prius and LS 600h values, but the high saliency range of LS 600h is larger than in Prius (see Fig. 2.11).

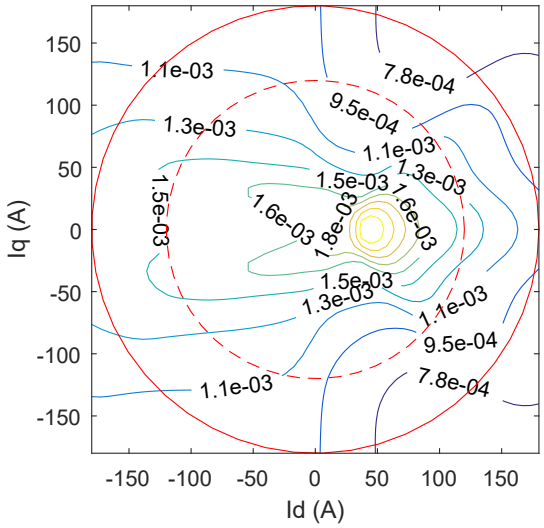

(a) L_d map (in henry).

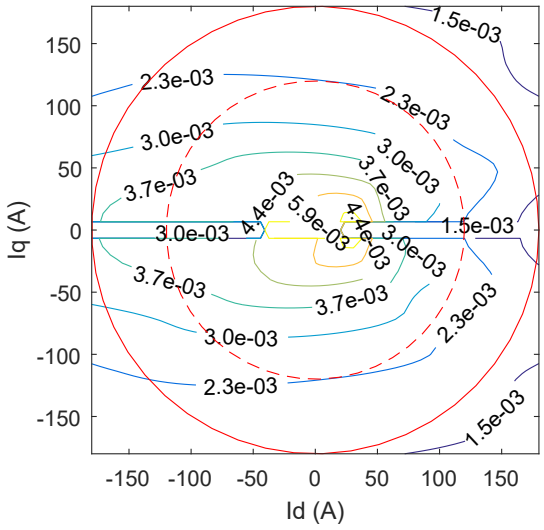

(b) L_q map (in henry).

Figure 2.7: Prius dq-frame inductances. Circles represent the current limits (solid line for overload conditions and dashed line for nominal current).

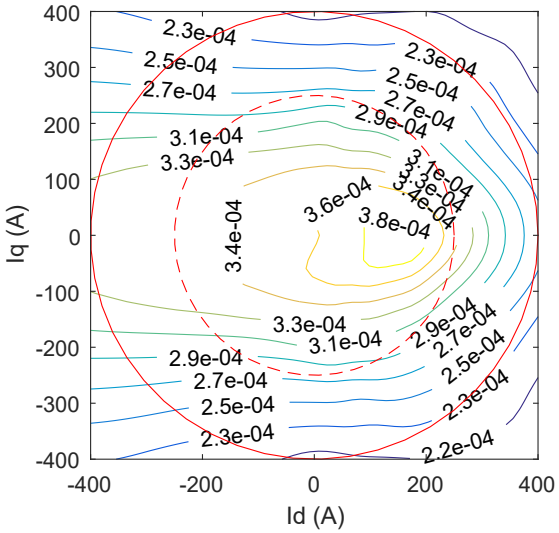

(a) L_d map (in henry).

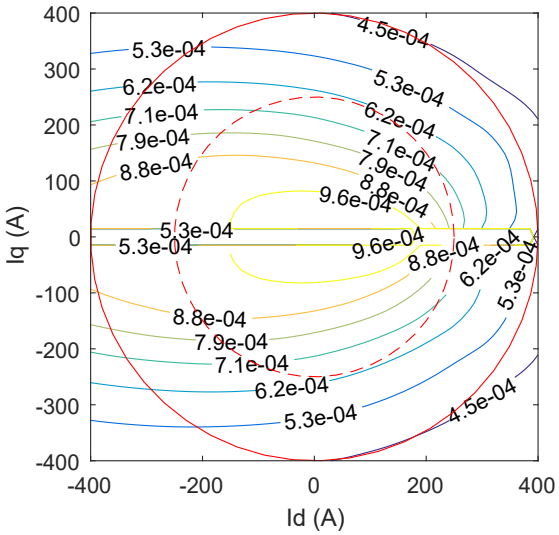

(b) L_q map (in henry).

Figure 2.8: LS 600h *dq*-frame inductances. Circles represent the current limits (solid line for overload conditions and dashed line for nominal current).

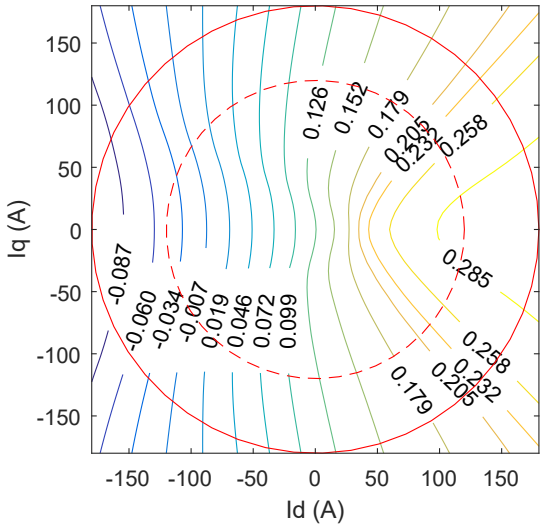

(a) Λ_d map (in V s).

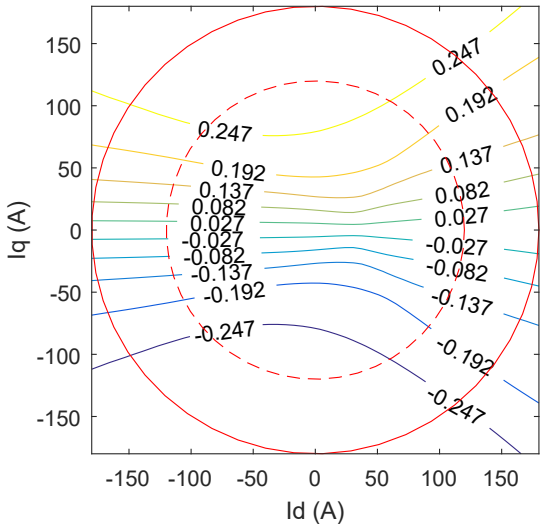

(b) Λ_q map (in V s).

Figure 2.9: Prius *dq*-frame flux linkages. Circles represent the current limits (solid line for overload conditions and dashed line for nominal current).

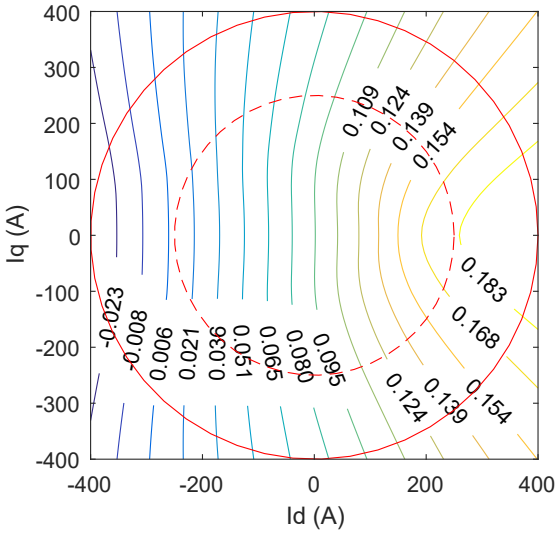

(a) Λ_d map (in V s).

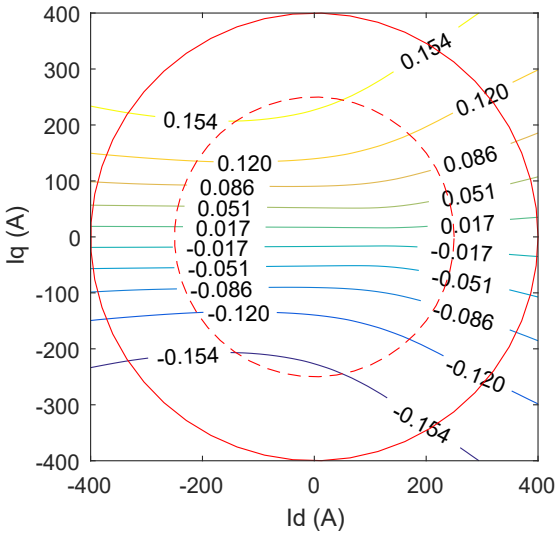

(b) Λ_q map (in V s).

Figure 2.10: LS 600h *dq*-frame flux linkages. Circles represent the current limits (solid line for overload conditions and dashed line for nominal current).

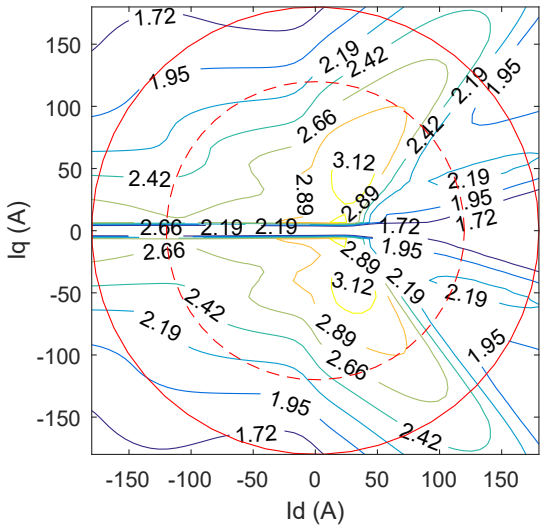

(a) Prius saliency ratio map.

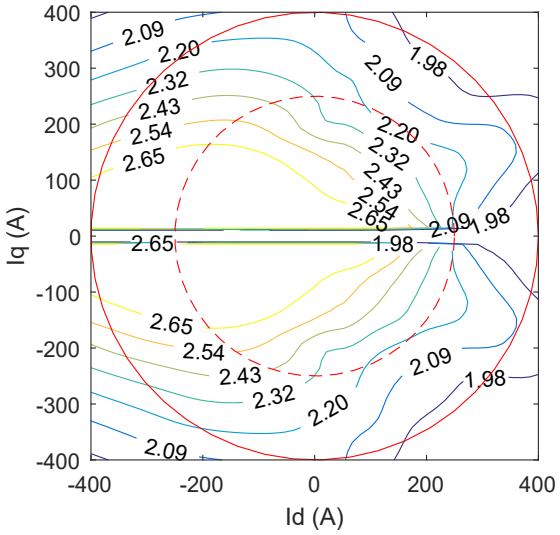

(b) LS 600h saliency ratio map.

Figure 2.11: Saliency ratio maps. Circles represent the current limits (solid line for overload conditions and dashed line for nominal current).

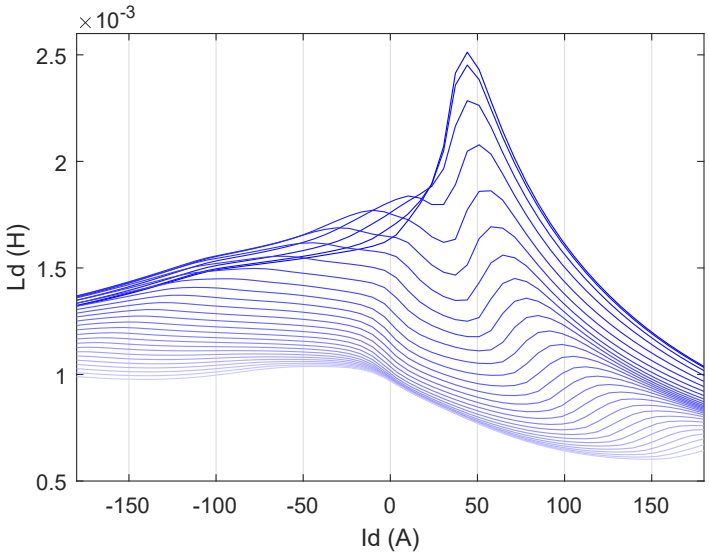

(a) L_d plot (in henry).

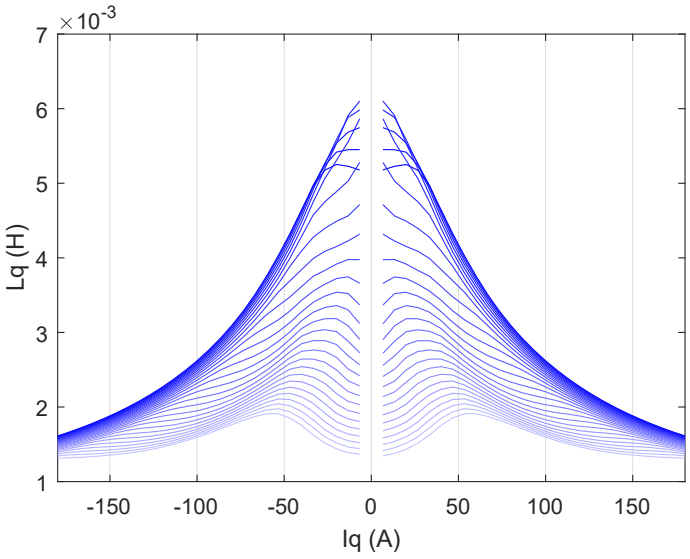

(b) L_q plot (in henry).

Figure 2.12: Prius dq-frame inductances. Color gradient shows the current dependency from the dq current not in the x-axis.

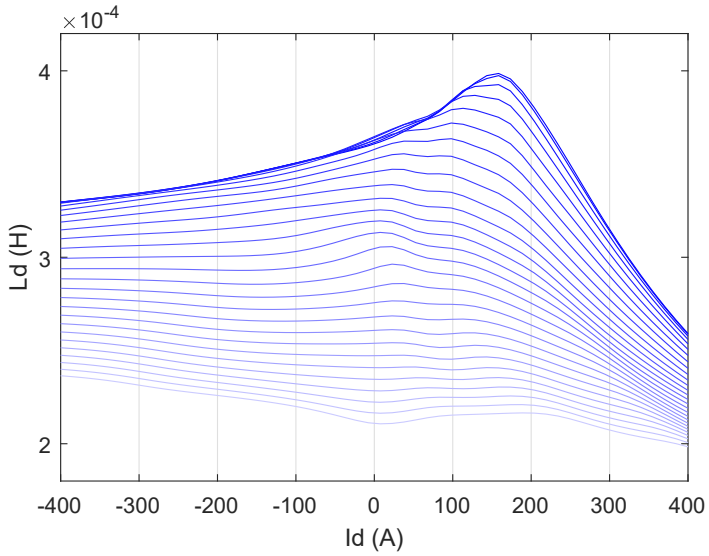

(a) L_d plot (in henry).

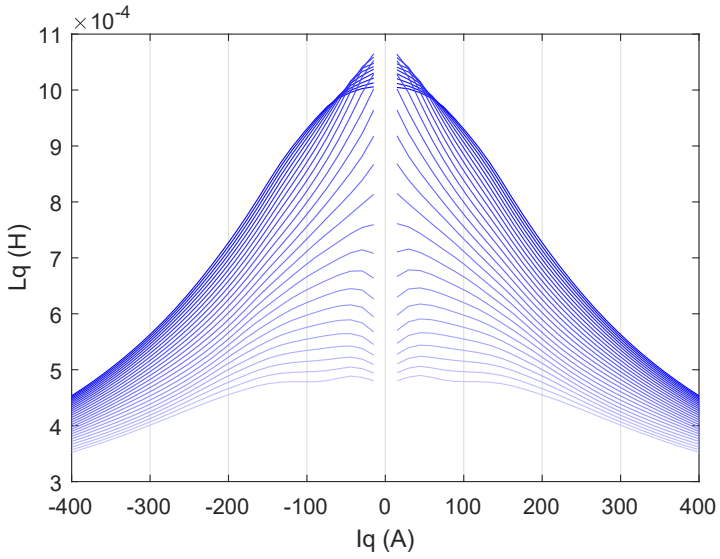

(b) L_q plot (in henry).

Figure 2.13: LS 600h *dq*-frame inductances. Color gradient shows the current dependency from the *dq* current not in the x-axis.

2.4.2 No-load characteristics

This subsection shows the no-load airgap flux density distributions B_{gm} with the related Fourier analysis up to the 40^{th} harmonic (Figs. 2.14–2.17) in order to evaluate the Total Harmonic Distortion (THD) and the open circuit back electromotive forces (EMF) of the Prius and LS 600h motors (Figs. 2.18–2.20). In Figs. 2.14a–2.17a, the fundamental tone is highlighted through the red line.

The comparison between Fig. 2.14 and 2.16 shows that with two flux barriers per pole (five discrete levels of flux density) better B_{gm} linearity is achievable than with only one flux barrier per pole (three discrete levels). The different harmonic content reflects on the motors back-emf shape. At 1 000 rpm the line back-emf amplitude of the Prius is 90 V while that of the LS 600h is 65 V, see Figs. 2.18b–2.19b. As an example, it is worth noting that although the Prius line back-emf reaches its inverter bus voltage (650 V) at 7 200 rpm (Fig. 2.20), the base speed is higher since the stator armature reaction should be taken into account.

However, Figs. 2.15 and 2.17 reveal the most important aspect of this analysis: the iron ribs, though necessary for the rotor mechanical integrity, waste a significant amount of PM flux in order to saturate. If the iron bridges were "opened", the machine performance would be improved by about 20 %, thus enabling remarkable cost savings. Unfortunately this is not possible normally (except for tangential magnetization machines, see next chapter) but careful attention must be paid to this rotor design issue as the iron bridges scale in number with the rotor flux barriers and in size (thickness) with the motor

Table 2.6: No-load airgap flux density summary.

$\widehat{B}_{gmMAX}/\widehat{B}_{gm1}$	**Prius**	**LS 600h**	**Unit**
Iron ribs closed	0.72 / 0.72	0.83 / 0.79	T
Iron ribs opened	0.96 / 0.95	1.03 / 0.97	T
Delta %	25 % / 24.2 %	19.4 % / 18.6 %	#

maximum speed.

The main results are summarized in Tab. 2.6.

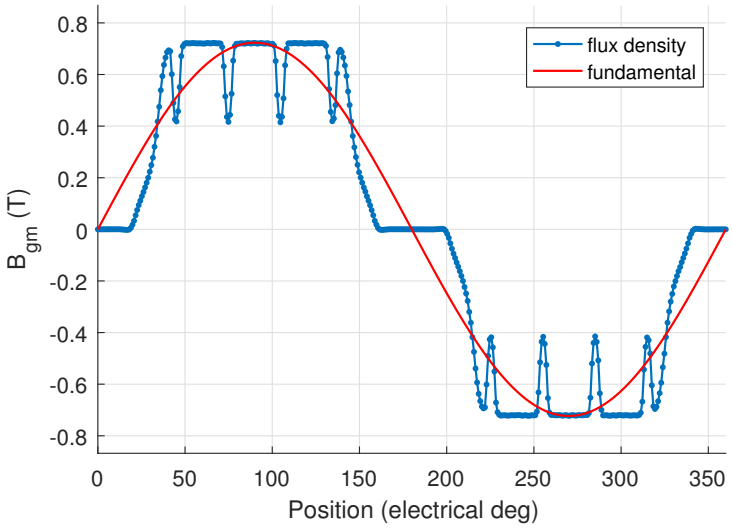

(a) Airgap flux density.

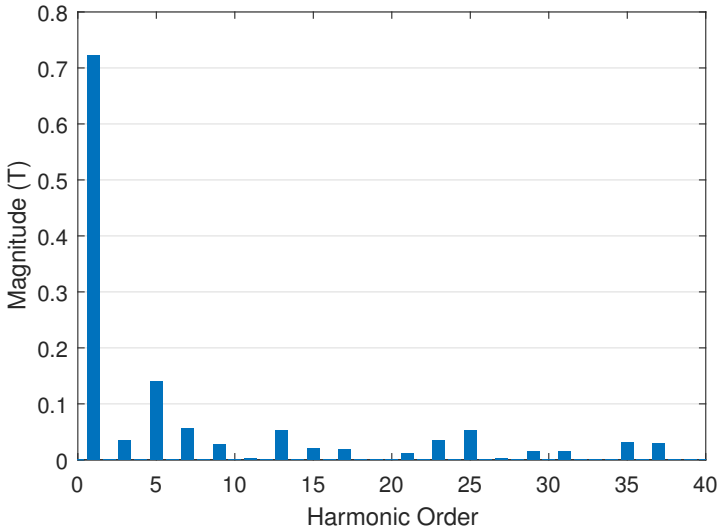

(b) B_{gm} FFT.

Figure 2.14: Prius airgap flux density at no load condition (two poles).

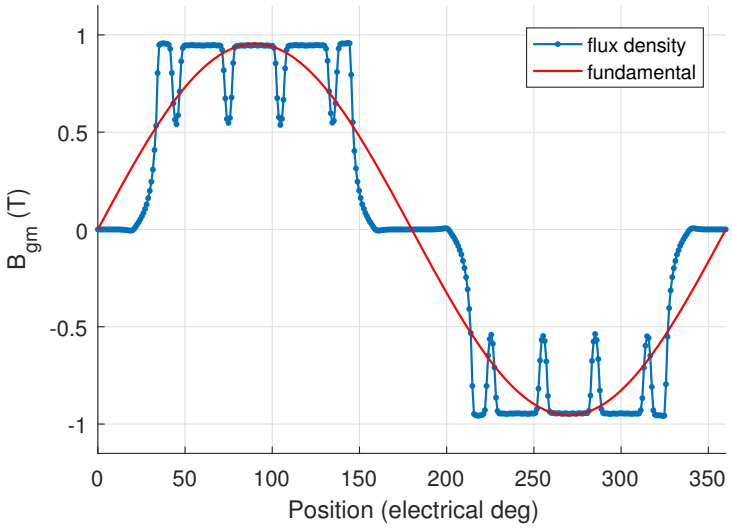

(a) Airgap flux density.

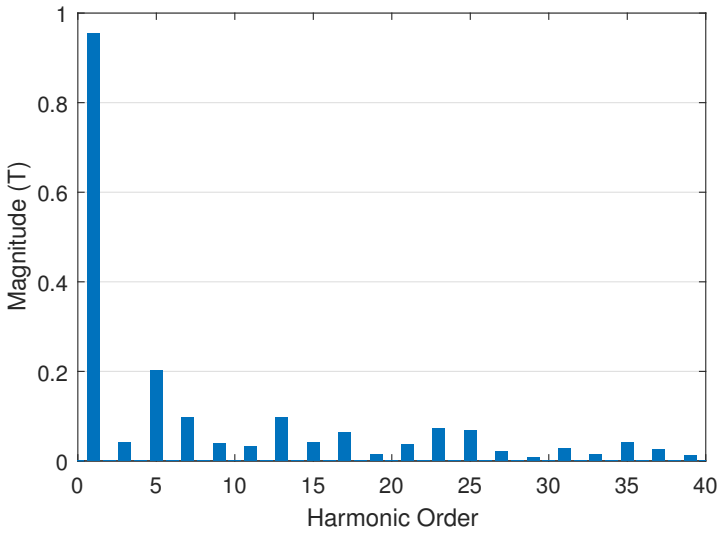

(b) B_{gm} FFT.

Figure 2.15: Prius airgap flux density at no load condition (two poles). Iron bridges open.

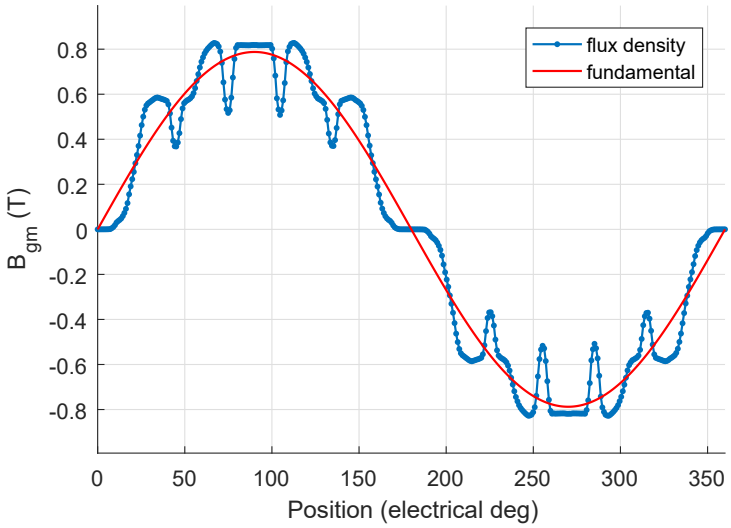

(a) Airgap flux density.

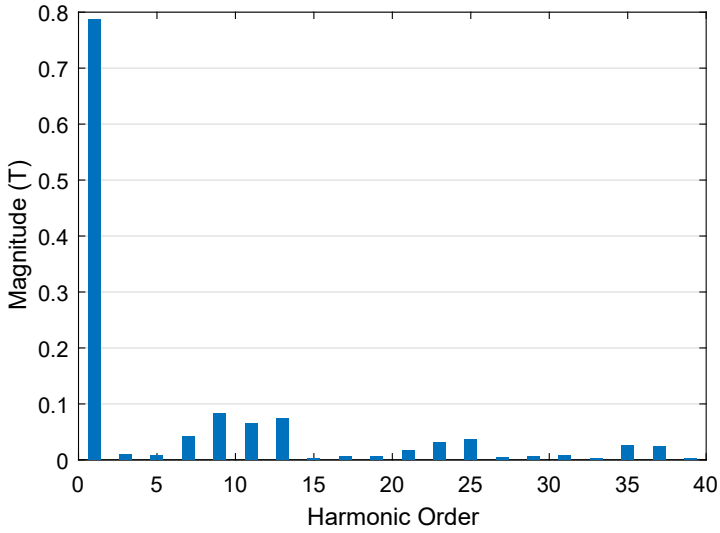

(b) B_{gm} FFT.

Figure 2.16: LS 600h airgap flux density at no load condition (two poles).

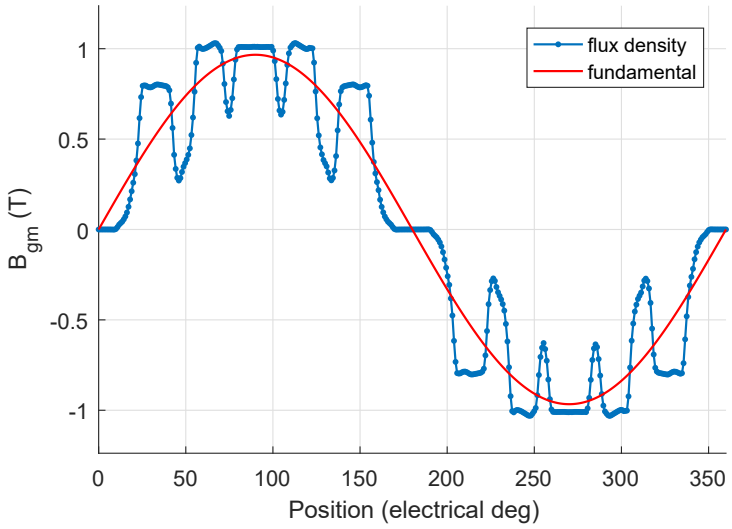

(a) Airgap flux density.

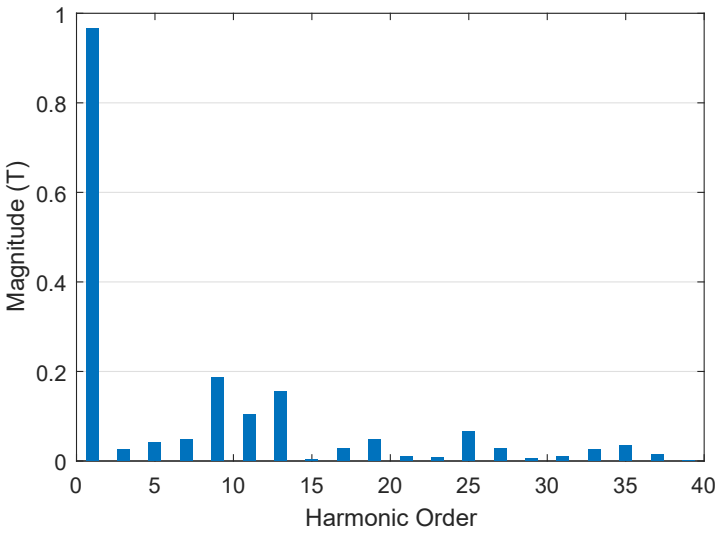

(b) B_{gm} FFT.

Figure 2.17: LS 600h airgap flux density at no load condition (two poles). Iron bridges open.

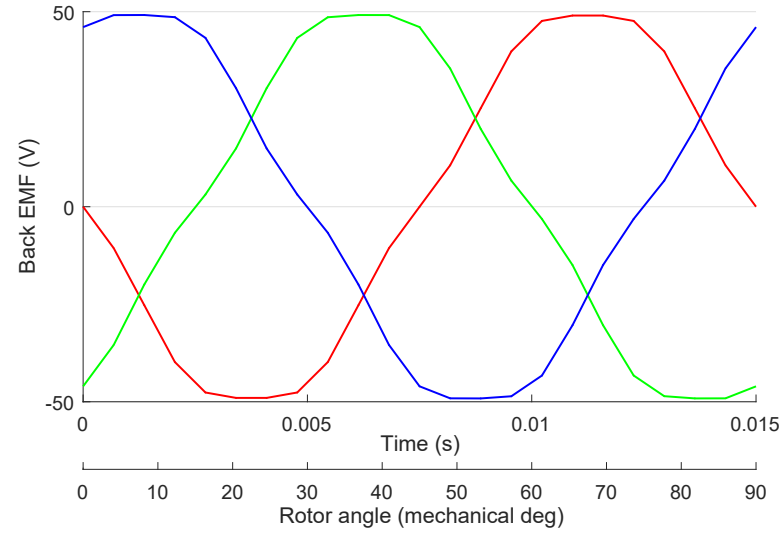

(a) Phase back EMF.

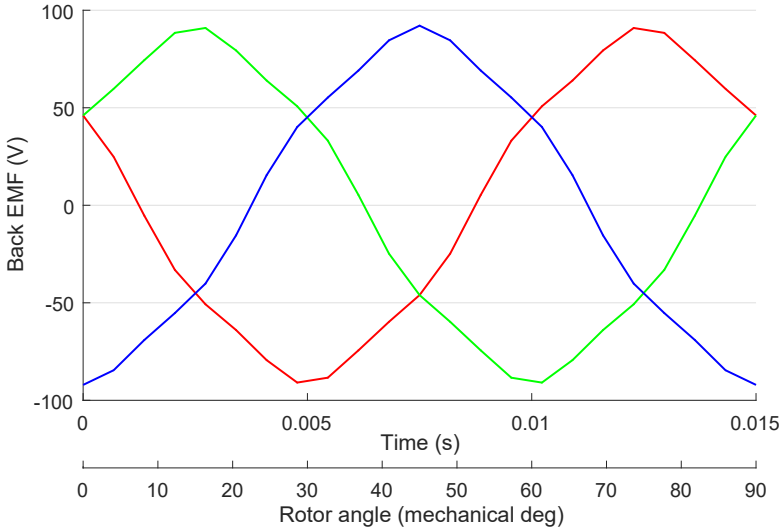

(b) Line back EMF.

Figure 2.18: Open circuit Prius back EMF at 1 000 rpm.

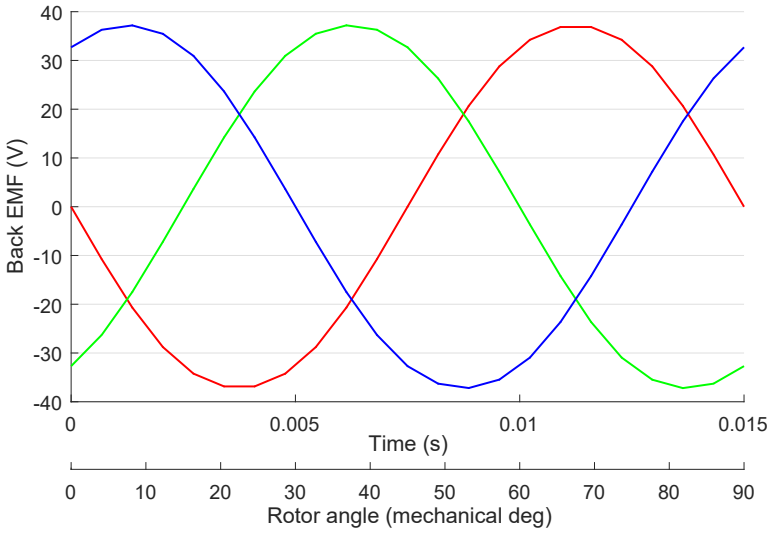

(a) Phase back EMF.

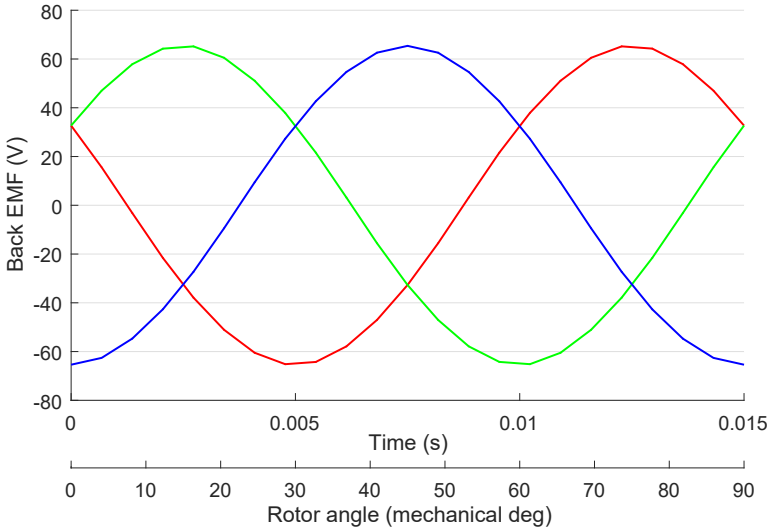

(b) Line back EMF.

Figure 2.19: Open circuit LS 600h back EMF at 1 000 rpm.

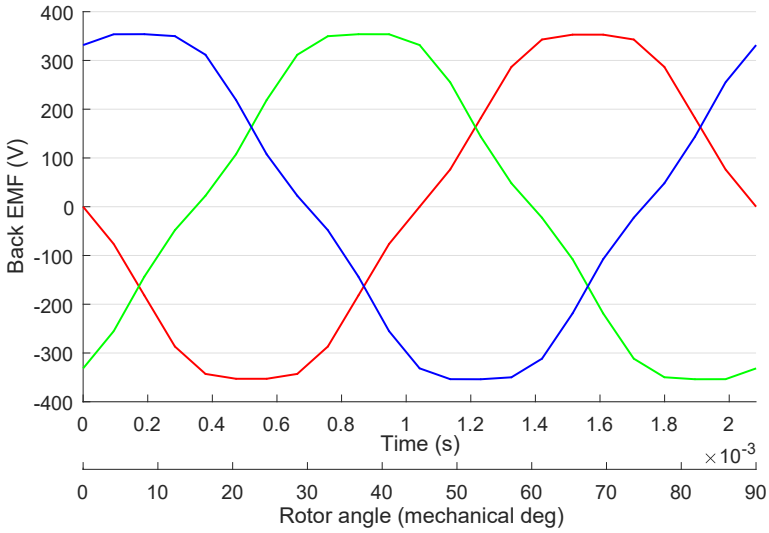

(a) Phase back EMF.

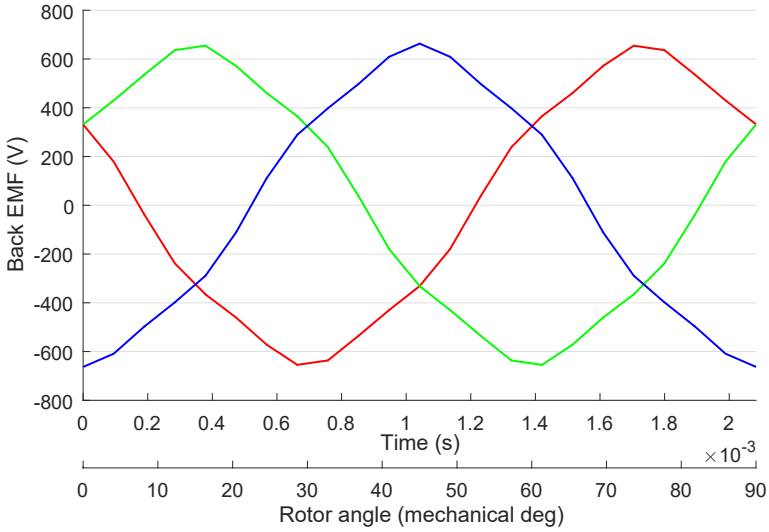

(b) Line back EMF.

Figure 2.20: Open circuit Prius back EMF at 7 200 rpm.

2.4.3 Torque analysis

In Figs. 2.21–2.24 the Prius and LS 600h motor torques are analyzed with both nominal and overload current. By means of the Maxwell stress tensor [15, 20], the PM and reluctance components of the torque are computed from the FE simulation results. Varying the current angle α_i^e in the interval 90°–180° with the current modulus set to the maximum value for the nominal and overload conditions, the maximum torque current angle can be found (see Figs. 2.21a–2.24a). The vertical bars represent the torque peak-to-peak ripple range. Also Figs. 2.21b–2.24b deal with the torque ripple by showing the maximum torque at different rotor angular positions. No skew is applied, therefore the inherent torque ripple can be examined. As can be seen, the ripple reaches rather high levels hence the real Prius and LS 600h machines make use of rotor skew very likely. However the ICE torque ripple is definitely worse than that of the IPM motor and traction applications do not have very tight constraints for the torque ripple, because of the vehicle large inertial mass.

Tables 2.7–2.9 report all the torque details. As Figs. 2.21–2.24 and Tabs. 2.7–2.9 show, in the IPM motors for HEVs and EVs propulsion, torque is composed by the mutual and reluctance components in 50 %–50 % proportion, usually.

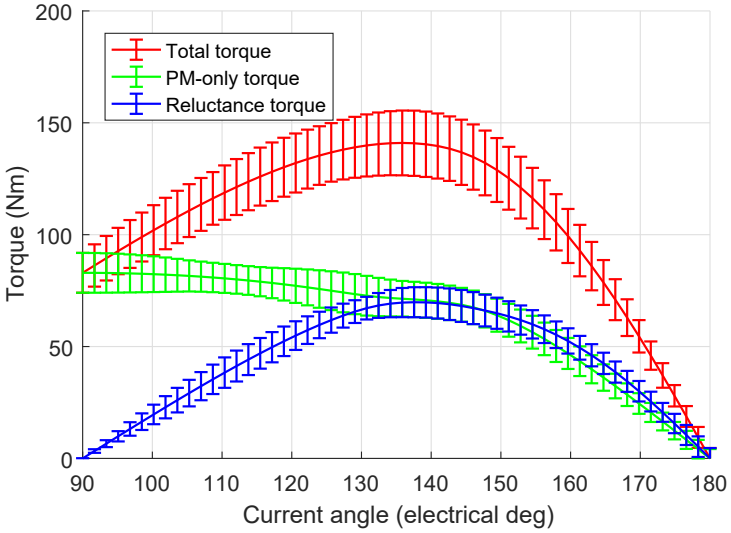

(a) Torque composition.

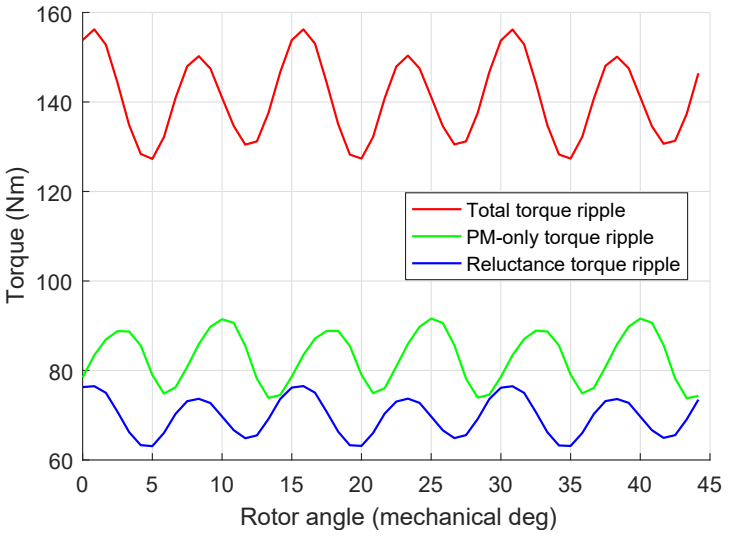

(b) Torque ripple.

Figure 2.21: Prius torque analysis with nominal current. (a) shows the torque composition. Vertical bars report the ripple. (b) illustrates torque ripple.

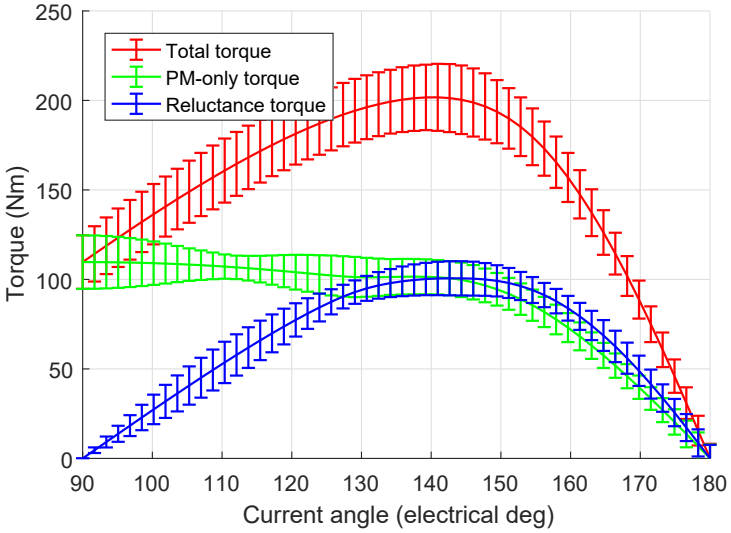

(a) Torque composition.

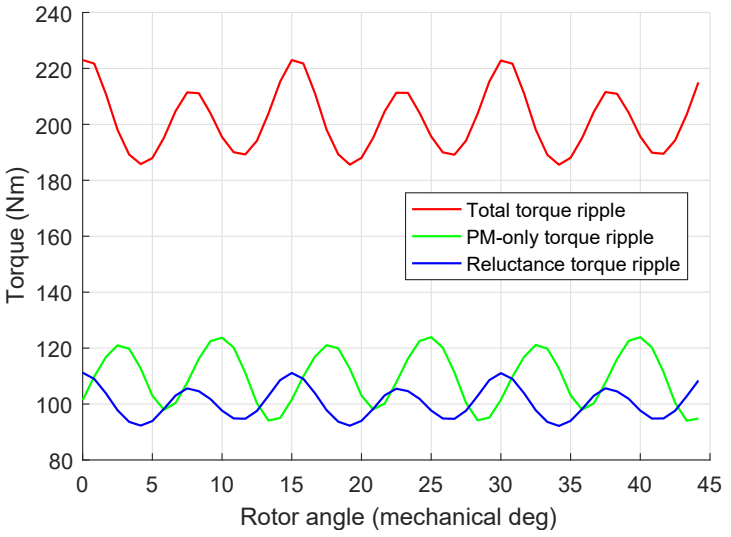

(b) Torque ripple.

Figure 2.22: Prius torque analysis with overload current. (a) shows the torque composition. Vertical bars report the ripple. (b) illustrates torque ripple.

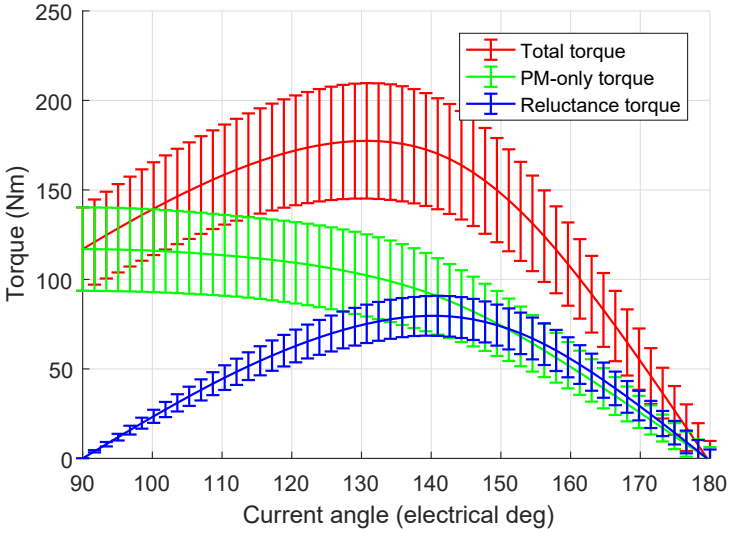

(a) Torque composition.

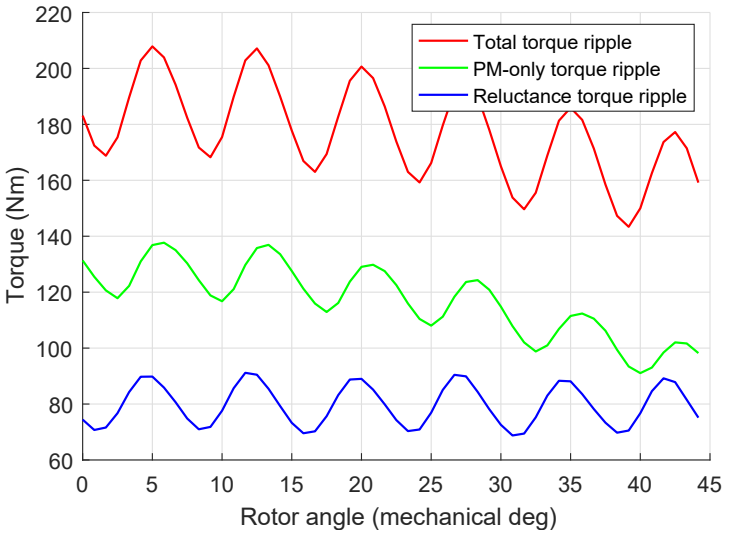

(b) Torque ripple.

Figure 2.23: LS 600h torque analysis with nominal current. (a) shows the torque composition. Vertical bars report the ripple. (b) illustrates torque ripple.

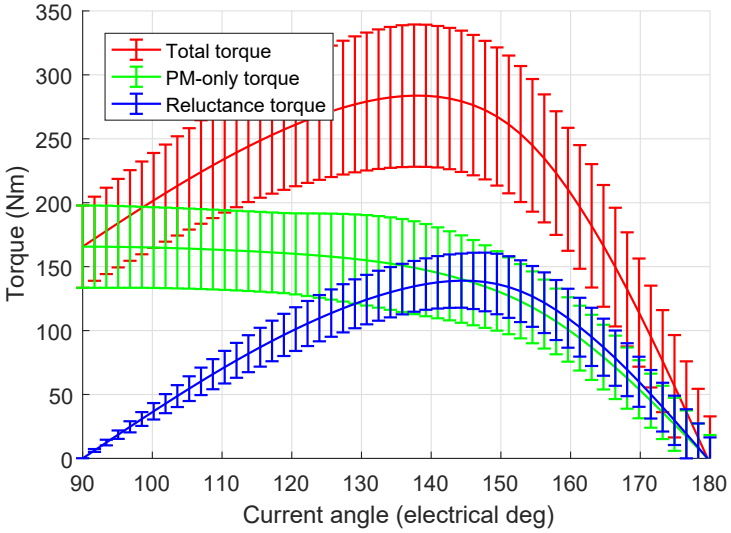

(a) Torque composition.

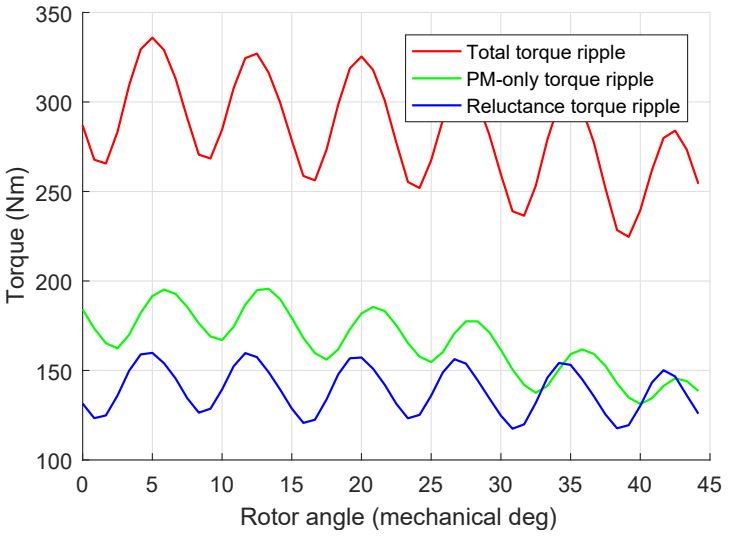

(b) Torque ripple.

Figure 2.24: LS 600h torque analysis with overload current. (a) shows the torque composition. Vertical bars report the ripple. (b) illustrates torque ripple.

Table 2.7: Torque details of Prius motor.

Component	**Nominal** (120 A)		**Overload** (180 A)	
	$\boldsymbol{T_{MAX}}$ (N m)	$\boldsymbol{\alpha^e_{iMAX}}$	$\boldsymbol{T_{MAX}}$ (N m)	$\boldsymbol{\alpha^e_{iMAX}}$
PM	82.9	90°	109.7	90°
Reluctance	69.8	137.5°	100.6	144.3°
Total	141	135.8°	201.7	140.9°

Table 2.8: Torque details of LS 600h motor.

Component	**Nominal** (250 A)		**Overload** (400 A)	
	$\boldsymbol{T_{MAX}}$ (N m)	$\boldsymbol{\alpha^e_{iMAX}}$	$\boldsymbol{T_{MAX}}$ (N m)	$\boldsymbol{\alpha^e_{iMAX}}$
PM	116.9	90°	165.6	90°
Reluctance	79.7	140.9°	139	144.3°
Total	177.4	130.8°	283.8	137.5°

Table 2.9: Maximum torque composition.

Motor	**Nominal**			**Overload**			**Units**
	$\boldsymbol{T_{PM}}$	$\boldsymbol{T_{rel}}$	$\boldsymbol{T_{tot}}$	$\boldsymbol{T_{PM}}$	$\boldsymbol{T_{rel}}$	$\boldsymbol{T_{tot}}$	
Prius	71.4	69.6	141	101.2	100.5	201.7	N m
	51 %	49 %	100 %	50 %	50 %	100 %	#
LS 600h	102.2	75.2	177.4	149.2	134.6	283.8	N m
	58 %	42 %	100 %	53 %	47 %	100 %	#

2.4.4 Dynamic curves and control

In this subsection, the dynamic properties of the Prius and LS 600h motors are studied. Figures 2.25a–2.26a illustrate the maximum torque vs speed, as well as power vs speed, curves of these two motors in both nominal (dashed line) and overload (solid line) conditions. The related control trajectories on the torque maps are depicted in Figs. 2.25b–2.26b. The MTPA and the Flux Weakening (FW) regions are clearly visible.

Observing Fig. 2.25b carefully, the Prius characteristic current seems to be about 90 A. It is a value lower than both the nominal and overload currents, therefore as the speed gets closer to the maximum, the Prius control trajectories have to enter the third region (see section 1.1.1) and the power curve exhibits a drop at high speed, as expected. On the contrary, the LS 600h power curve holds at the power rating level in the whole CPSR, since this machine needs only the FW second region to reach the maximum speed. Together with the higher base speed, this feature has been achieved by means of the two parallel paths winding as explained in section 3.4 and 3.5. A shorter CPSR is the only side effect of such technical solution.

2.4.5 Efficiency maps

Figure 2.27 shows the Prius and LS 600h efficiency maps. Both the motors exhibit remarkable efficiency levels (up to 96 %) and the LS 600h high efficiency area is wider than the Prius one.

Finally, Fig. 2.28 comprises the maps of the maximum magnetic flux density in the two machine cores. The FW effect is evident.

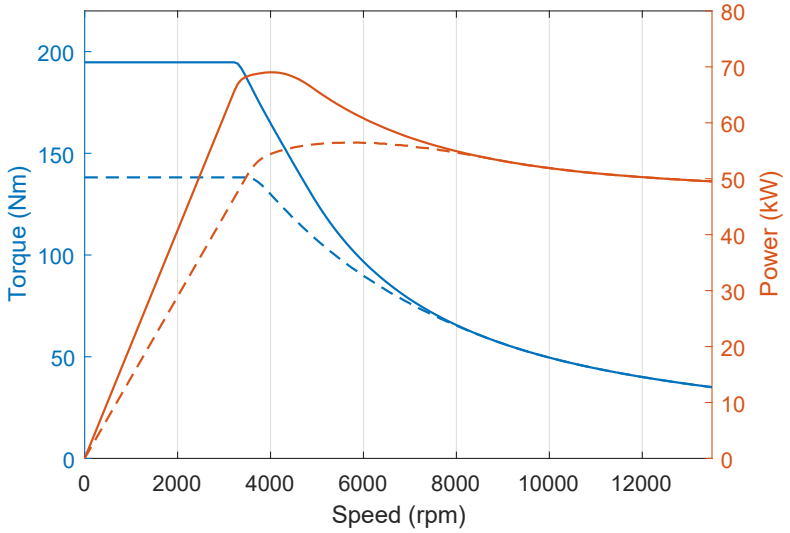

(a) Dynamic curves.

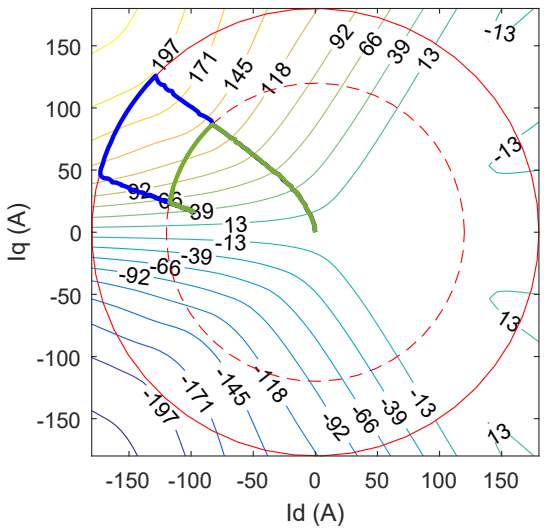

(b) Control trajectories on the torque map (N m).

Figure 2.25: Prius max. torque and power vs. speed (a) with control trajectories (b). Solid and blue line for overload, dashed and green for nominal.

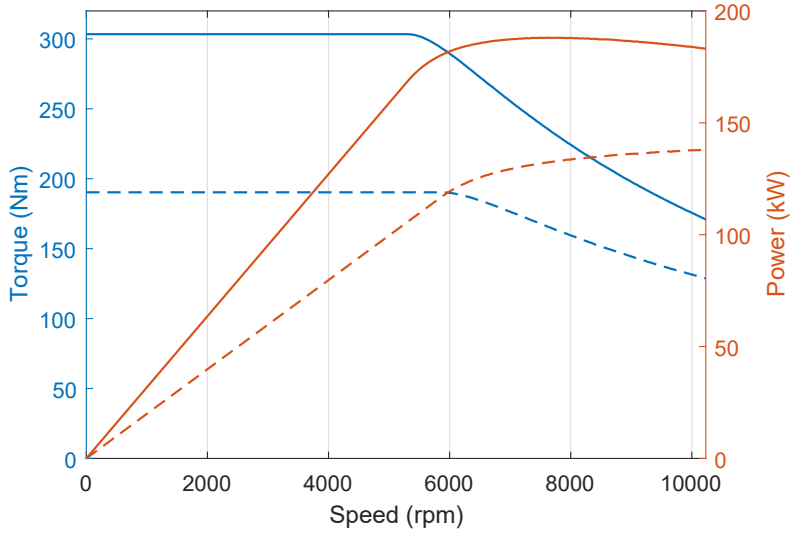

(a) Dynamic curves.

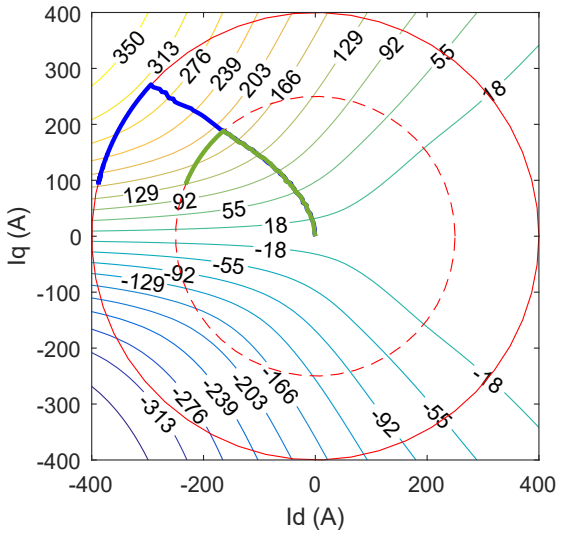

(b) Control trajectories on the torque map (N m).

Figure 2.26: LS 600h max. torque and power vs. speed (a) with control trajectories (b). Solid and blue line for overload, dashed and green for nominal.

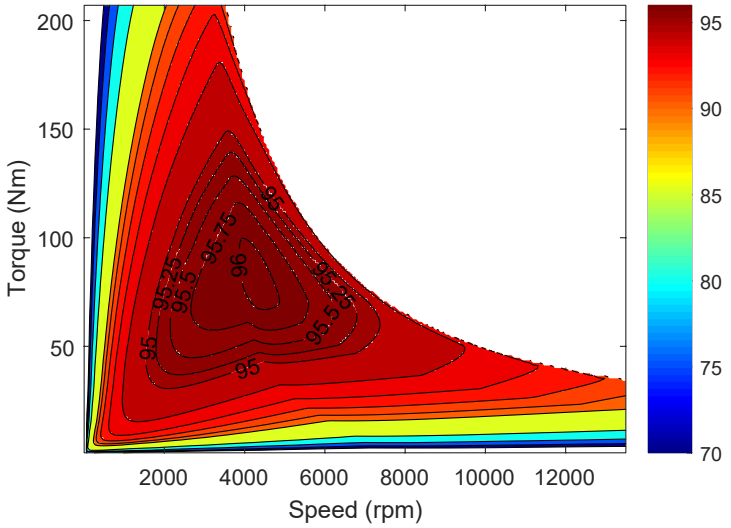

(a) Prius.

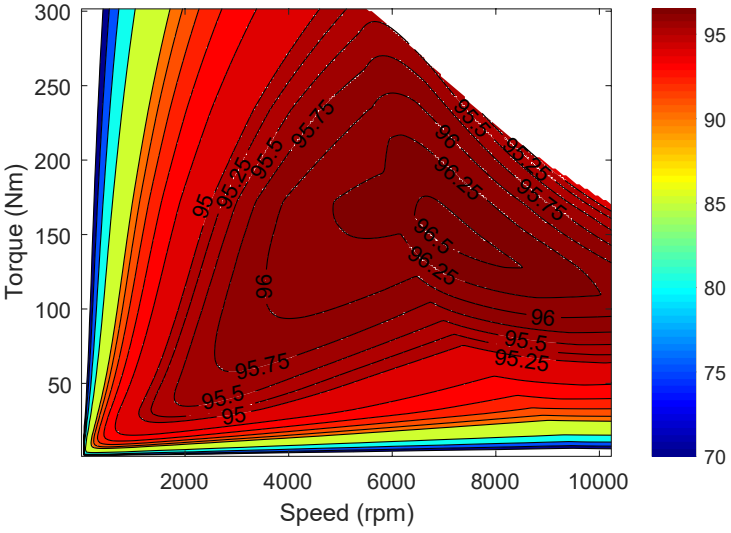

(b) LS 600h.

Figure 2.27: Efficiency maps in percentage.

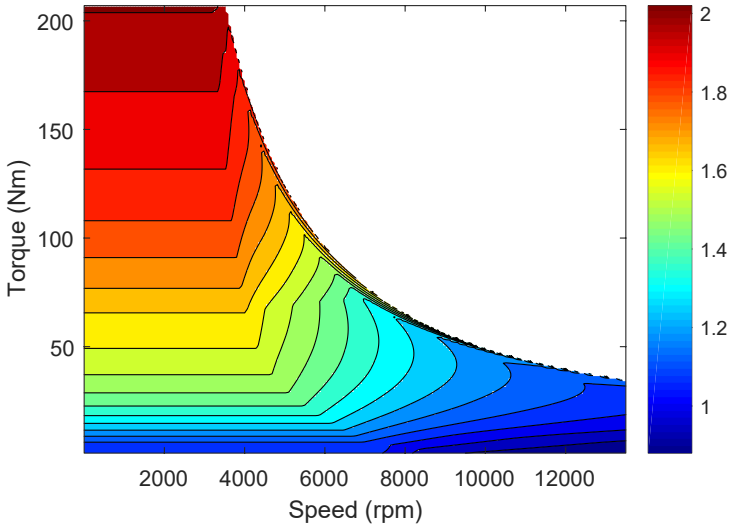

(a) Prius.

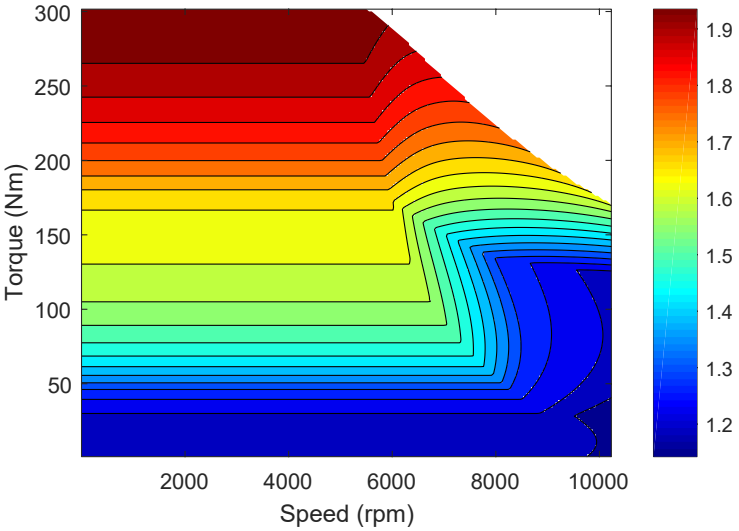

(b) LS 600h.

Figure 2.28: Maximum B (T) in the machine core maps.

Chapter 3

IPM motors design guidelines for EVs and tradeoffs

In this chapter the main design options along with the typical parameters state-of-the-art values are discussed in order to achieve the most important features of an IPM traction motor. The recent industrial and research trends in this field are also discussed highlighting their limits. Then, the analytical equations explained in chapter 2 are used in a design perspective.

Among the main issues addressed in this chapter, the PM mass reduction coming from the adoption of specific rotor topologies together with the performance enhancement through geometry optimization will be studied with particular attention.

Finally, design guidelines are proposed taking into account the several IPM machine tradeoffs.

3.1 Electrical and magnetic loading

Looking at (2.28), it can be observed that the key to the machine torque density maximization are the electrical and magnetic loading. Increasing the $\widehat{K}_s$ and $\widehat{B}_{gm}$ terms enables to reduce the motor active volume. As reported by (2.62)–(2.63), the $\widehat{B}_{sd}$ and $\widehat{B}_{sq}$ terms are function of $\widehat{K}_{sd}$ and $\widehat{K}_{sq}$, therefore it is a duty of the control loop to use always the right current angle α_i^e to feed the motor properly. The saliency ratio ξ maximization contributes to the reluctance torque without enlarging the motor. This objective can be obtained increasing the flux barriers thickness and number but some drawbacks may occur and will be discussed in section 3.6.

Obviously, all the design parameters mentioned above have unavoidable limits. The $\widehat{K}_s$ magnitude is conditioned by the current density level in the windings. This can lead to heat dissipation issues. Typical values of J_s and $\widehat{K}_s$ in machines with passive dissipation are 4–7 $\mathrm{A\,mm^{-2}}$ and 40–50 $\mathrm{A\,mm^{-1}}$ respectively. For this reason, the electric motors for automotive traction applications usually are oil or water cooled, hence pushing the electrical loading to significantly higher limits (see Tab. 2.4).

Generally, to raise the $\widehat{B}_{gm}$ value in an IPM machine, large amounts of expensive rare-earth PM such as NdFeB or SmCo are used. This has a negative impact on the motor cost, making it less competitive on the market. In addition, a high $\widehat{B}_{gm}$ results in a larger PM flux linkage and characteristic current, thus making the motor less suitable to flux weakening. Moreover, $\widehat{B}_{gm}$, $\widehat{B}_{sd}$ and $\widehat{B}_{sq}$ are overall subject to the magnetic saturation limit of the lamination, which typically is about 2 T. Increasing the number of flux barriers makes it also possible to lower the total harmonic distortion (THD) of the no-load air-gap flux density distribution. This can help to achieve a higher fundamental magnitude $\widehat{B}_{gm}$.

3.2 Number of poles

Typically, the number of pole pairs p in an IPM motor for HEV or EV traction is relatively high. These machines have nowadays eight poles (Toyota/Lexus) or more, as in the BMW i3 with twelve poles.

Increasing p allows reducing both the "ancillary" parts of the machine: the end-windings and the yokes of the stator and rotor. These elements are necessary to close the winding electric circuit and the iron magnetic path in accordance with the Gauss law, but are not involved directly in the torque generation process. Therefore in good designs, it is desirable to reduce the end-windings and the yokes at minimum. Shorter end-windings lead to lower leakage inductances [15] and ohmic losses, while smaller stator and rotor yokes produce less iron losses and give lighter machines. In addition, the bill of material is lowered.

The airgap flux density distribution can be discretized teeth by teeth $B_g(k)$. Assuming for simplicity the rotor d-axis aligned with a stator slot (in Fig. 2.6 the rotor is aligned with a tooth but the conclusions generality holds anyway), $B_g(k)$ can be expressed as follows.

$$\begin{aligned} B_g(k) &= \frac{1}{\alpha_s^e} \int_{(k-1)\,\alpha_s^e}^{k\,\alpha_s^e} \left[\left(\widehat{B}_{gm} + \widehat{B}_{sd} \right) \cdot \cos\theta + \widehat{B}_{sq} \cdot \sin\theta \right] \mathrm{d}\theta \\ &= \frac{1}{\alpha_s^e} \left[\left(\widehat{B}_{gm} + \widehat{B}_{sd} \right) \cdot \sin\theta \Big|_{(k-1)\,\alpha_s^e}^{k\,\alpha_s^e} - \widehat{B}_{sq} \cdot \cos\theta \Big|_{(k-1)\,\alpha_s^e}^{k\,\alpha_s^e} \right] \end{aligned} \tag{3.1}$$

where k is the tooth index.

The magnetic flux in the k-th tooth is given by a simple *flux tube* [15] equation.

$$\phi_{th}(k) = B_g(k) \cdot p_s \cdot L_{stk} \tag{3.2}$$

Since the magnetic flux of each pole splits in two halves and each half goes to one of the two adjacent poles through the stator yoke, or the back-iron, the flux in each back-iron circular segment results:

$$\phi_{bi}(n) = \sum_{k=1}^{n} \phi_{th}(k) \quad \text{with } n = 1 \dots \frac{y_q - 1}{2} \tag{3.3}$$

n is the back-iron segment index.

Each of the segments in which the stator yoke is divided links two adjacent teeth. The back-iron height h_{bi} expression is:

$$h_{bi} = \frac{D_e - D}{2} - h_s - h_{so} \tag{3.4}$$

where h_{so} is the slot opening height and the flux density therefore results:

$$B_{bi}(n) = \frac{\phi_{bi}(n)}{h_{bi}\, L_{Fe}} \tag{3.5}$$

where $L_{fe} = L_{stk} \cdot k_{pack}$ and k_{pack} is the stacking factor.

In no-load conditions, the magnetic flux in the back-iron grows from the middle of each pole to the median point between two poles, as each yoke segment collects the flux of all the preceding teeth. When the motor is powered, the back-iron works in the same way but the flux distribution is shifted depending on the α_i^e. The h_{bi} has to be large enough to avoid an excessive iron saturation, so the maximum $B_{bi}(n)$, occurring at $n = (y_q - 1)/2$, must not exceed 2 T. Increasing p, the number of slots (and teeth) per pole y_q is reduced (2.2), hence less teeth flux is gathered (3.3) and the h_{bi} constraint is relaxed. The same happens for the rotor yoke.

Finally, recalling (2.20), the end-winding reduction is shown.

The obvious limit to the pole number rise is the control loop feasibility as the maximum electric frequency increases with p. In addition, if q drops below 1, the machine becomes fractional slot and slightly more attention should be paid in the design.

3.3 Torque composition

As shown in Tab. 2.9 the total torque in the IPM motors for electric powertrains usually consists of PM and reluctance components almost equally. Over the years, both industry and research have tried to replace some part of the mutual torque with more reluctance or even to remove almost completely the PMs from the rotors as in synchronous reluctance (SynREL) motors or PM-assisted SynREL. However, the efforts to replace magnet torque with reluctance torque almost invariably lead to increases in the machine mass and volume [23].

Assuming the theoretical limit condition $\xi \to \infty$, from (2.29), the maximum PM-only and reluctance-only torques result:

$$\begin{aligned} T_{PM-MAX} &= \widehat{B}_{gm}\, \widehat{K}_{sq} \left(\frac{\pi}{4} D^2 L_{stk}\right) \\ T_{rel-MAX} &= -\widehat{B}_{sq}\, \widehat{K}_{sd} \left(\frac{\pi}{4} D^2 L_{stk}\right) \end{aligned} \tag{3.6}$$

since from (2.62)

$$\widehat{B}_{sd} = \frac{\mu_0}{g'} \cdot \frac{\widehat{K}_{sd} D}{2p} \cdot \frac{1}{\xi} \to 0 \tag{3.7}$$

Now, applying the (1.3) angle convention to (2.27) and substituting the (2.63), the (3.6) becomes:

$$\begin{aligned} T_{PM-MAX} &= \widehat{B}_{gm}\, \widehat{K}_{s} \left(\frac{\pi}{4} D^2 L_{stk}\right) \\ T_{rel-MAX} &= \left(\frac{\mu_0}{g'} \cdot \frac{\widehat{K}_s\, D}{4p}\right) \widehat{K}_{s} \left(\frac{\pi}{4} D^2 L_{stk}\right) \end{aligned} \tag{3.8}$$

obviously the maximum torque current angle β_i^e is $0°$ for T_{PM-MAX} and $45°$ for $T_{rel-MAX}$. In order to achieve $T_{rel-MAX}$ values comparable to the T_{PM-MAX}, the following condition must be met:

$$\frac{\mu_0}{g'} \cdot \frac{\widehat{K}_s\, D}{4p} = \widehat{B}_{gm} \tag{3.9}$$

Using the free space permeability $\mu_0 = 4\,\pi \cdot 10^{-7}\,\mathrm{H\,m^{-1}}$ together with approximate standard values for $\widehat{B}_{gm} \simeq 1\,\mathrm{T}$ and $g' \simeq 1\,\mathrm{mm}$ in (3.9) results:

$$\widehat{K}_s \cdot (\pi\, D) = p \cdot 10^4 \tag{3.10}$$

a rather high value, especially with the typical pole pairs numbers $p \geq 4$.

It means that in order to replace the PM torque with the reluctance component, the armature reaction has to produce the missing airgap PM flux density $\widehat{B}_{gm}$ by means of higher current linear density $\widehat{K}_s$ levels, with more ohmic losses as a consequence, or by enlarging the motor inner diameter D. The machine torque density results then compromised as expected.

On the other hand, machines relying only on the mutual torque, as happens in the SPM motors, could have a too limited speed range [16]. For this reason, the two torque components should be someway balanced in the IPM traction motors. This concept will be discussed with more detail in the next section.

3.4 Characteristic current

As seen in the section 1.1.1, the main limit to the IPM motor speed is represented by the back-emf whose rise progressively nulls the phase voltage drop necessary to the voltage source inverter to drive the motor. In order to extend the machine speed range, the flux weakening control technique has been developed. The FW algorithm consists in compensating the back-emf growth due to the increasing speed, see (1.13), by gradually shifting the current angle α_i^e towards π or, in the equivalent form, $\beta_i^e \to \pi/2$. This is the description of the "region 2" control trajectory.

When the maximum power is requested to the motor in the CPSR, the FW trajectory has to lie on the current limit circumference as shown in Fig. 1.5, and $\hat{I} = I_{ch} = I_{MAX}$.

In this particular operating conditions, approximating the trigonometric functions with their Taylor first order polynomials (3.11), the torque (1.4) equation becomes the following (3.12).

$$\begin{cases} \sin(\beta_i^e) \simeq 1 \\ \cos(\beta_i^e) \simeq -\beta_i^e + \dfrac{\pi}{2} \\ \sin(2\,\beta_i^e) \simeq -2\,\beta_i^e + \pi \end{cases} \tag{3.11}$$

$$T \simeq \frac{3}{2} \cdot p \cdot I_{MAX}^2 \left(\frac{\pi}{2} - \beta_i^e\right) \xi\, L_d \tag{3.12}$$

Making similar considerations for the voltage equations (1.13), leads to the conclusions:

$$\begin{cases} v_d \simeq -\omega_e\, L_q\, I_{ch}\, \cos(\beta_i^e) \\ v_q \simeq \omega_e \cdot [\Lambda_{PM} - L_d\, I_{ch}\, \sin(\beta_i^e)] \to 0 \end{cases} \tag{3.13}$$

$$\sqrt{v_d^2 + v_q^2} \simeq \omega_e\, L_q\, I_{ch} \left(\frac{\pi}{2} - \beta_i^e\right) \tag{3.14}$$

Examining the voltage modulus equation (3.14) and the (3.12), it can be observed that both the torque and the phase voltage decrease proportionally to the difference between $\pi/2$ and β_i^e. In this way, as the speed ω_e rises, β_i^e must take values closer and closer to $\pi/2$ in order to keep the voltage modulus lower than V_{MAX}. Doing so, according to (3.12), the torque is reduced with the same rate at which ω_e grows and the output mechanical power $P = (\omega_e/p) \cdot T$ remains constant at the maximum value.

That is a very desirable feature of the FW region 2 but sometimes, if $I_{ch} < I_{MAX}$, this technique may be not sufficient to reach the maximum speed. In this case, $\hat{I}$ must be reduced as the terms related to the inductances L_d and L_q in (1.13) are the next source of back-emf after Λ_{PM}, and those terms are proportional to $\hat{I}$. The control trajectory enters the FW region 3 and detaches from the current limit circumference, since $\hat{I} \to I_{ch}$. Unfortunately, the reluctance torque component is a quadratic function of $\hat{I}$. It means that the torque reduction rate in region 3 is much higher than in region 2, hence at high speeds a mechanical power output drop can be observed [19].

Equation 1.28 says that EVs need a not negligible propulsion power not only to achieve but also to hold the maximum speed. Although SynREL and PMASynREL are cost effective solutions and, if properly designed, can achieve the same peak performances of IPM motors, their I_{ch} cannot be equal to I_{MAX}. Therefore, their high speed performances are substantially lower than what IPM motors can do. In addition, the electrical powertrain machines are used not only for traction but also for braking, then the power high speed drop due to the region 3 would compromise the regenerative decelerating EV capabilities while driving on highways, for instance.

This problem, together with the lower machine density, explains why the synchronous reluctance motors have not been successful among the EV manufacturers. Currently, the Chevy 2016 Volt powertrain is the only example of PMASynREL motor available on the automotive market [24]. However, the Voltec Gen2 made by GM is a rather complex hybrid propulsion unit which is composed by an ICE and two electric motors: the ferrite-based PMASynREL (motor A) and a NdFeB-based IPM (motor B). The motor A ratings (48 kW and 118 N m) are substantially lower than those of the motor B (87 kW and 280 N m), and the motor A role is only to support the motor B. Therefore it cannot be defined a "full-PMASynREL solution".

On the contrary, if the PM flux linkage is too high, as in the SPM motors, the I_{ch} would exceed the maximum inverter current I_{MAX} and the machine FW capabilities could be poor. Again, a balanced mix of PM and reluctance, or saliency, is the right choice.

3.5 Parallel paths

In section 3.4 the consequences of a reduction in the machine PM amount have been discussed. If the PM volume is decreased, the I_{ch} is lowered and the output power falls at high speed. The only way to reduce the amount of PM, as well as the flux linkage Λ_{PM}, without this drawback, is by keeping I_{ch} unchanged but this is possible only decreasing L_d. The most used technique to obtain this result is increasing the number of the winding parallel paths n_{pp}, which means to modify the equivalent number N_s of series conductors per phase [19]. As an example, the hairpin windings typically have $n_{pp} > 1$, so the following analysis applies also to such kind of winding.

$$\phi_{PM} = \widehat{B}_{gm} \frac{D\, L_{stk}}{p} \qquad (3.15) \qquad\qquad \Lambda_{PM} = \phi_{PM} \frac{k_w\, N_s}{2} \qquad (3.16)$$

Equations 3.15 and 3.16 express the PM magnetic flux and the related flux linkage respectively. From (2.3) and (2.4) it can be observed that N_s as well as Λ_{PM} are inversely proportional to n_{pp}, while the (2.53) shows that L_d is inversely proportional to the square of n_{pp}. For instance, if n_{pp} is set to 2, as for the LS 600h, the Λ_{PM} would scale down by a factor of 2 whereas L_d by a factor of 4, making I_{ch} twice as well. Therefore, the $\widehat{B}_{gm}$ could be halved keeping I_{ch} constant.

$$\begin{aligned} T_{PM} &= \frac{3}{2} \cdot p \cdot \left[I_{ch}\, \hat{I} \cos(\beta_i^e) \right] L_d \\ T_{rel} &= \frac{3}{2} \cdot p \cdot \left[\frac{1}{2} (\xi - 1)\, \hat{I}^{\,2} \sin(2\beta_i^e) \right] L_d \end{aligned} \qquad (3.17)$$

In this case the current modulus $\hat{I}$ must be doubled in order to keep the torque almost unvaried. Looking at (3.17), the reluctance component T_{rel} depends quadratically on $\hat{I}$, so a double current modulus can fully compensate the L_d reduction. On the contrary, T_{PM} is only proportional to $\hat{I}$ and the PM torque decrease can be only limited by doubling the current modulus. In theory, the relative weight of T_{rel} would double compared to T_{PM}, but the consequent

variation of the current angle β_i^e can mitigate this rise. In conclusion, the high speed performances of the motor do not change despite the PM reduction but the machine torque density decreases to some extent.

Contrarily to what one normally expects, the motor ohmic losses do not grow with the above-mentioned current increase, as the phase resistance R_{ph} is inversely proportional to the square of n_{pp}.

$$R_{ph} = \rho \, L_c \, \frac{Q_s \, n_c}{m \cdot n_{pp}^2 \, S_c} \tag{3.18}$$

However, the power converter current rating needs to be increased accordingly and this impacts its cost. At the same time, with fixed system power rating, the nominal voltage of both the motor and converter is downscaled by n_{pp}, then the insulation system can be reduced.

In addition, the voltage limit ellipse in the current dq plane is enlarged, the major and minor radii being $V_{MAX}/(L_d \, \omega_e)$ and $V_{MAX}/(L_q \, \omega_e)$ respectively. V_{MAX} is divided by n_{pp} but both L_d and L_q are divided by n_{pp}^2, therefore the base speed moves towards a higher value.

3.6 Rotor geometry design

This section deals with the rotor geometry design issues. In the industrial sectors characterized by a high technology competition, the rush for maximum performance results frequently in multi-objective optimization problems.

3.6.1 Multi-objective optimization

Finding the optimal rotor geometry of a high performance IPM motor involves several variables and has a significant influence on the overall characteristics of the motor. The design process of the rotor geometry inherently includes many tradeoffs, so a good balance between the performance figures of merit is rather difficult. A multi-objective optimization [25] is further complicated due to the particularly demanding design constraints of the automotive industry. The optimization algorithms are computationally-intensive, as the fitness functions have to be evaluated repeatedly. Multiple FE simulations would require an unreasonable time to process. In this context, a computationally-efficient physical model of the motor is mandatory [26].

The magnetic model described in section 2.3 is used to perform an automatic multi-objective optimization, trying to identify the Pareto front numerically [22]. This allows to locate the case study (Lexus LS 600h motor) within the solution space, thus determining its distance from the Pareto front and its possible improvements.

Since it is based on a small set of recursive formulas, its functionality can be easily extended to a variable number of flux barriers. In order to validate the effectiveness of the proposed model providing objective functions suitable for IPM rotor design optimization, the LS 600h motor has been considered as a benchmark. Moreover, given the possibility of the analytical model to handle a variable number of flux barriers, it is possible to exploit other rotor designs. It is reasonable to assume that Lexus develops its electric motors optimizing the machine parameters with commercial applications and proprietary software. Therefore, in order to assess the presented model validity, the LS 600h design

optimality has been checked. Then a third flux barrier has been introduced to test also the new model generality.

The optimization algorithm adopted in the first part of this section is the multi-objective Genetic Algorithm (GA). For motor optimization problems, Evolutionary Algorithms and GA are today well-established, yet still competitive approaches [27, 26]. The study of solutions with an increased number of barriers, and the subsequent expansion of optimization variables, highlighted some limits of the GA algorithm used. Namely, it is difficult for the algorithm to find a good initial population when the number of variables and constraints is relatively high (approximately greater than 20). To overcome these limitations, a different approach to determine the Pareto front was devised. It uses the multi-objective goal attainment minimizer provided by MATLAB, empowered by a multidimensional sweep of the attainment weighting parameters and a Monte Carlo generation of the starting points. Further improvement of a selection of Pareto points is obtained by means of a second optimization round, using the interior-point algorithm of `fmincon`.

The presented approach is compared against other motor optimization workflows, such as that of the *SyR-e* toolbox [28], which is focused on PMASynREL topologies. It uses a Multi Objective Differential Evolution (MODE) algorithm, but each fitness function evaluation requires the execution of a FEA analysis through the software *FEMM* [29]. SyR-e embodies an analytical model as well, but it is used only for a preliminary sizing of the machine, and it deals only with maximum torque and power factor of the machine.

3.6.2 Objective functions

Three different optimization tasks were run, each of them with four objective functions to be minimized:

- reciprocal of motor saliency (ξ^{-1}), because the saliency ratio is related to the reluctance component of the torque;
- absolute distance of the no-load airgap flux density fundamental (B_{gm1})

from a reasonable target value, which is set at 1 T (approximately half of the magnetic saturation level in laminations) to avoid an excessive saturation of the machine iron core with the armature reaction;

- the Total Harmonic Distortion (THD) of the airgap flux density distribution due to PM $B_{gm}(\theta_r)$, as the harmonic amplitudes may increase the back-emf, thus limiting further the achievable speed, and may raise the saturation level of the iron without a remarkable torque gain;

- the magnet cross-section area, in order to contain the manufacturing costs (with a given length of the stack L_{stk}, PM cross-section area determines the magnet volume).

Commonly, the torque ripple is also taken into account for the optimal design of an electric motor but in this specific application it has a lower priority. Anyway, a lower THD of the $B_{gm}(\theta_r)$ also helps to relieve the torque ripple.

Both saliency and B_{gm1} contribute to the machine torque, however the two torque components have different "quality", so a balanced composition enables the machine to achieve better performances. A higher level of PM torque, associated with B_{gm1}, typically improves the machine density but reduces the flux weakening capability as well as the CPSR. Conversely, too much reluctance torque makes the machine larger and heavier but enhances the overload factor together with the maximum attainable speed. For these reasons, saliency and B_{gm1} have been considered as two distinct objective functions.

3.6.3 Test of the method effectiveness

The first optimization run had only three degrees of freedom to process (barrier angles α_{m1}, α_{m2} and magnet thickness t_m), assuming the shorter barrier to be orthogonal to the radius and the longer one to have a double width ($w_{m2} = 2\,w_{m1}$) as it is in the LS 600h "modular" geometry (see Fig. 2.6b). The second optimization used six free variables (α_{m1}, α_{m2}, w_{m1}, w_{m2}, t_{m1}, t_{m2}). Results of these processes are shown in Fig. 3.1–3.3.

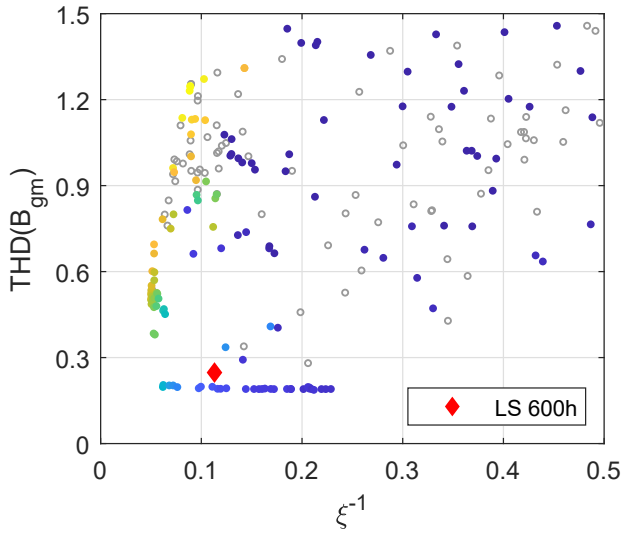

(a) Two barriers, constrained, xy plane.

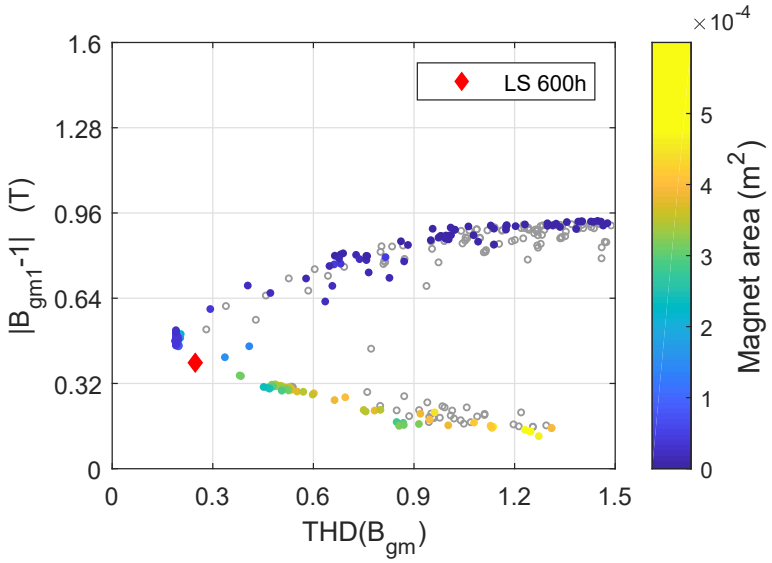

(b) Two barriers, constrained, yz plane.

Figure 3.1: Multivariate Pareto plots for two flux barriers and three decision variables.

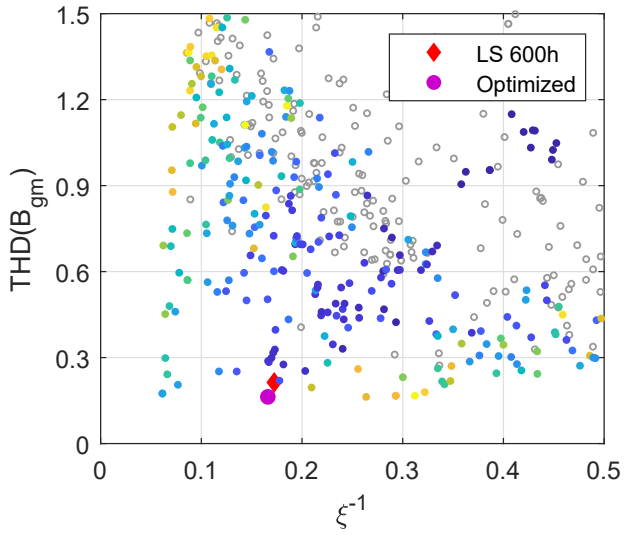

(a) Two barriers, unconstrained, xy plane.

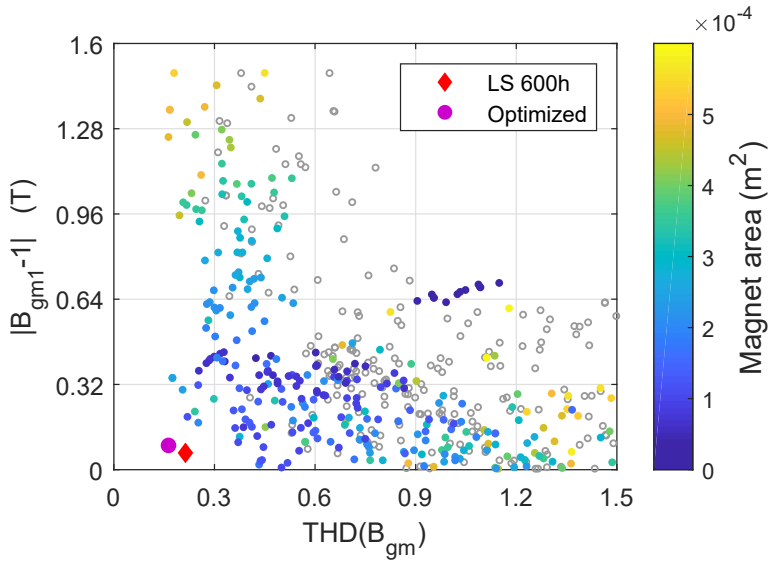

(b) Two barriers, unconstrained, yz plane.

Figure 3.2: Multivariate Pareto plots for two flux barriers and six decision variables.

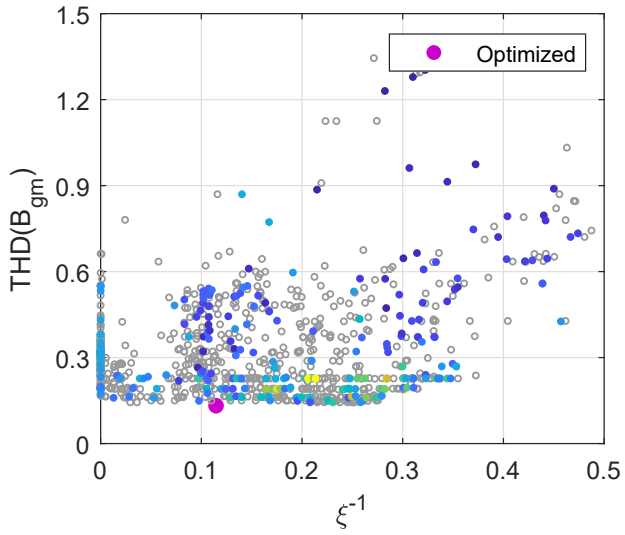

(a) Three barriers, unconstrained, xy plane.

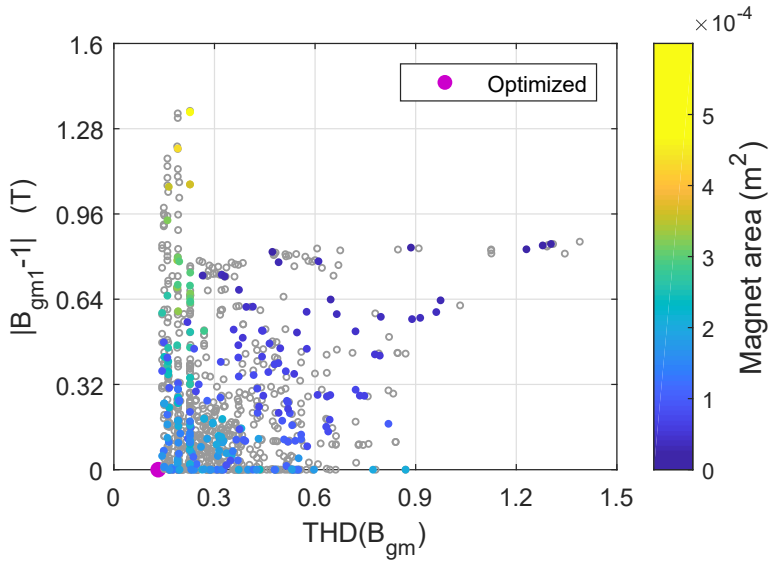

(b) Three barriers, unconstrained, yz plane.

Figure 3.3: Multivariate Pareto plots for three flux barriers and twelve decision variables.

Table 3.1: FE simulation results for LS 600h rotor geometry variations. For the saliency, both saturated ($\hat{I}$ = 400 A) and not saturated values are reported. The PM area is considered per pole.

	Saliency ratio	$\mathbf{B_{gm\,1}}$ (T)	**THD ($\mathbf{B_{gm}}$)**	**Area $_{\mathbf{PM}}$** (10^{-4}m^2)
LS 600h	2.36 ÷ 2.79	0.79	0.1912	1.71
$-\Delta\alpha_{m1}$ (9.5 deg.)	2.21 ÷ 2.55 *(−6.4% ÷ −8.6%)*	0.74 *(-6.3%)*	0.2314 *(+21%)*	1.56 *(-8.8%)*
$+\Delta\alpha_{m1}$ (9.5 deg.)	2.32 ÷ 2.96 *(−1.7% ÷ +6.1%)*	0.82 *(+3.8%)*	0.1935 *(+1.2%)*	1.86 *(+8.8%)*
$-\Delta t_{m1}$ (33%)	2.25 ÷ 2.69 *(−4.7% ÷ −3.6%)*	0.78 *(-1.3%)*	0.1932 *(+1%)*	1.52 *(-11.1%)*
$+\Delta t_{m1}$ (33%)	2.40 ÷ 2.85 *(+1.7% ÷ +2.1%)*	0.79 *(±0%)*	0.1903 *(-0.5%)*	1.9 *(+11.1%)*
$-\Delta\alpha_{m2}$ (5 deg.)	2.30 ÷ 2.88 *(−2.5% ÷ +3.2%)*	0.78 *(-1.3%)*	0.1980 *(+3.6%)*	1.71 *(±0%)*
$+\Delta\alpha_{m2}$ (5 deg.)	2.30 ÷ 2.59 *(−2.5% ÷ −7.2%)*	0.80 *(+1.3%)*	0.2052 *(+7.3%)*	1.71 *(±0%)*
$-\Delta w_{m2}$ (27%)	2.05 ÷ 2.70 *(−13.1% ÷ −3.2%)*	0.61 *(-22.8%)*	0.2750 *(+43.8%)*	1.41 *(-17.5%)*
$+\Delta w_{m2}$ (27%)	2.33 ÷ 2.55 *(−1.3% ÷ −8.6%)*	0.95 *(+20.2%)*	0.2297 *(+20.1%)*	2.02 *(+18.1%)*
$-\Delta t_{m2}$ (33%)	2.21 ÷ 2.55 *(−6.4% ÷ −8.6%)*	0.73 *(-7.6%)*	0.1944 *(+1.7%)*	1.34 *(-21.6%)*
$+\Delta t_{m2}$ (33%)	2.42 ÷ 2.95 *(+2.5% ÷ +5.7%)*	0.83 *(+5.1%)*	0.1955 *(+2.2%)*	2.08 *(+21.6%)*

The first optimization, with only three design parameters, showed that the case study is almost located on the Pareto front, thus it cannot be improved appreciably using the available degrees of freedom (see Fig. 3.1a and 3.1b). The FE simulation results reported in Tab. 3.1 agree with this conclusion, as no geometry variation achieves better performances for all the objectives. The percentage deviations from the reference values (LS 600h), are annotated in brackets.

Moving to six parameters, the results of Fig. 3.2a and 3.2b are obtained. Differently from before, the LS 600h motor can be improved by choosing the optimized solution, that exploits the possibility to have different magnet widths and thicknesses. The optimized solution dominates the case study, with a major improvement on the flux density THD.

3.6.4 Validation of the model generality and performance

In order to validate the proposed recursive magnetic model universality, a new rotor geometry optimization process has been carried out, increasing the flux barriers number to three. All the other machine parameters are the same as in the LS 600h. Fig. 3.3a-3.3b show the achieved Pareto front and the selected optimal design (Fig. 3.4a). Comparing the solutions in Fig. 3.1a-3.2b to those in Fig. 3.3a-3.3b, a higher scattering level can be observed as GAs belong to the global optimization algorithms category. The goal-attain solutions lower scattering explains graphically the higher effectiveness to converge which this algorithm exhibits.

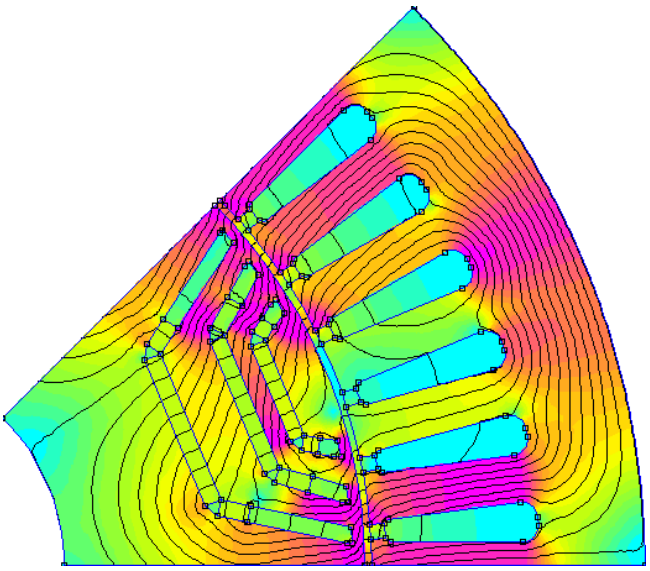

(a) Optimal design.

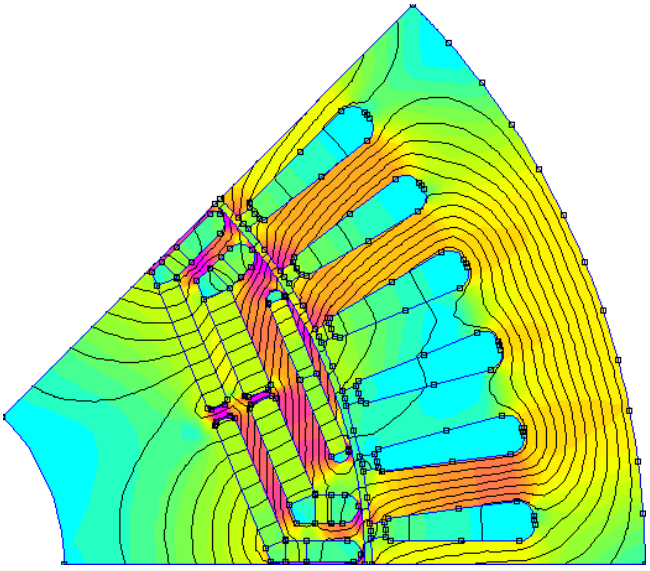

(b) SyR-e design.

Figure 3.4: FE simulations of the three barrier motors cross-sections.

Table 3.2: FE simulation results for the three barrier rotor geometry optimization. For the saliency, both saturated ($\hat{I} = 400$ A) and not saturated values are reported. The PM area is considered per pole.

	Saliency ratio	$\mathbf{B_{gm\,1}}$ (T)	**THD ($\mathbf{B_{gm}}$)**	**Area $_{\mathbf{PM}}$** (10^{-4}m^2)
Optimal	2.19 ÷ 2.77	0.67	0.1741	1.49
$-\Delta\alpha_{m1}$ (7 deg.)	2.08 ÷ 2.56	0.68	0.1949	1.49
$+\Delta\alpha_{m1}$ (7 deg.)	2.28 ÷ 2.74	0.66	0.1681	1.49
$-\Delta\alpha_{m2}$ (7 deg.)	2.16 ÷ 2.54	0.67	0.2255	1.49
$+\Delta\alpha_{m2}$ (7 deg.)	2.1 ÷ 2.75	0.67	0.1713	1.49
$-\Delta\alpha_{m3}$ (7 deg.)	2.12 ÷ 2.61	0.67	0.2124	1.49
$+\Delta\alpha_{m3}$ (7 deg.)	2.09 ÷ 2.68	0.67	0.1576	1.49
$-\Delta w_{fb1}$ (14%)	2.29 ÷ 2.84	0.68	0.1753	1.49
$+\Delta w_{fb1}$ (14%)	2.12 ÷ 2.62	0.66	0.1732	1.49
$-\Delta w_{fb2}$ (8%)	2.19 ÷ 2.8	0.68	0.1755	1.49
$+\Delta w_{fb2}$ (14%)	2.16 ÷ 2.52	0.66	0.1940	1.49
$-\Delta w_{fb3}$ (14%)	2.09 ÷ 2.48	0.67	0.2145	1.49
$+\Delta w_{fb3}$ (14%)	2.2 ÷ 2.77	0.67	0.1785	1.49
$-\Delta t_{m1}$ (50%)	2.13 ÷ 2.71	0.67	0.1708	1.32
$+\Delta t_{m1}$ (50%)	2.06 ÷ 2.48	0.7	0.1888	2.23
$-\Delta t_{m2}$ (50%)	2.02 ÷ 2.58	0.62	0.1513	1.04
$+\Delta t_{m2}$ (50%)	2.13 ÷ 2.64	0.71	0.1854	2.06
$-\Delta t_{m3}$ (50%)	1.79 ÷ 2.24	0.57	0.1897	0.74
$+\Delta t_{m3}$ (50%)	2.21 ÷ 2.89	0.7	0.1515	1.78
$-\Delta w_{m1}$ (20%)	2.12 ÷ 2.57	0.65	0.1812	1.42
$+\Delta w_{m1}$ (20%)	2.19 ÷ 2.52	0.83	0.2121	1.79
$-\Delta w_{m2}$ (20%)	2.17 ÷ 2.46	0.58	0.1633	1.31

continued on next page

continued from previous page

	Saliency ratio	$\mathbf{B_{gm\,1}}$ (T)	**THD ($\mathbf{B_{gm}}$)**	**Area $_{\mathbf{PM}}$** ($10^{-4}\mathrm{m}^2$)
$+\Delta w_{m2}$ (20%)	$2.12 \div 2.48$	0.8	0.2058	1.72
$-\Delta w_{m3}$ (20%)	$2.18 \div 2.83$	0.51	0.1704	1.19
$+\Delta w_{m3}$ (20%)	$2.18 \div 2.6$	0.74	0.1487	1.6
$-\Delta\alpha_{m1}$ (57%) $-\Delta w_{fb1}$ (55%) $-\Delta w_{m1}$ (47%)	$2.09 \div 2.61$	0.65	0.1824	1.33
$-\Delta w_{fb2}$ (6%) $-\Delta w_{fb3}$ (16%)	$2.1 \div 2.51$	0.68	0.1809	1.49
$+\Delta w_{fb3}$ (40%) $+\Delta w_{m3}$ (116%)	$2.04 \div 2.16$	0.98	0.2625	2.16
$w_{m1} = w_{m2} = 0$ $+\Delta w_{m3}$ (92%) $+\Delta t_{m3}$ (33%)	$2.2 \div 2.9$	0.65	0.5356	2.39
$+\Delta w_{m1}$ (23%) $+\Delta w_{m2}$ (32%) $+\Delta w_{m3}$ (92%)	$2.3 \div 2.7$	1.14	0.1840	2.29
SyR-e Optimal	$2.09 \div 2.97$	0.98	0.1877	2.64

Tab. 3.2 reports the FE simulation results for the optimal design (Fig. 3.4a) together with 29 geometry variations. Among the possible configurations in the Pareto front, an optimal design has been selected giving priority to the PM usage reduction but also other choices could be reasonable. In addition, another optimal design (Fig. 3.4b) returned from SyR-e has been included in this table for comparison. The available objectives in that toolbox, however, are different: B_{gm} THD is not present and saliency as well as $B_{gm\,1}$ are incorporated in the torque objective. This time, to cover a broader range of possible cases, a higher priority has been given to the machine performance relaxing the PM volume

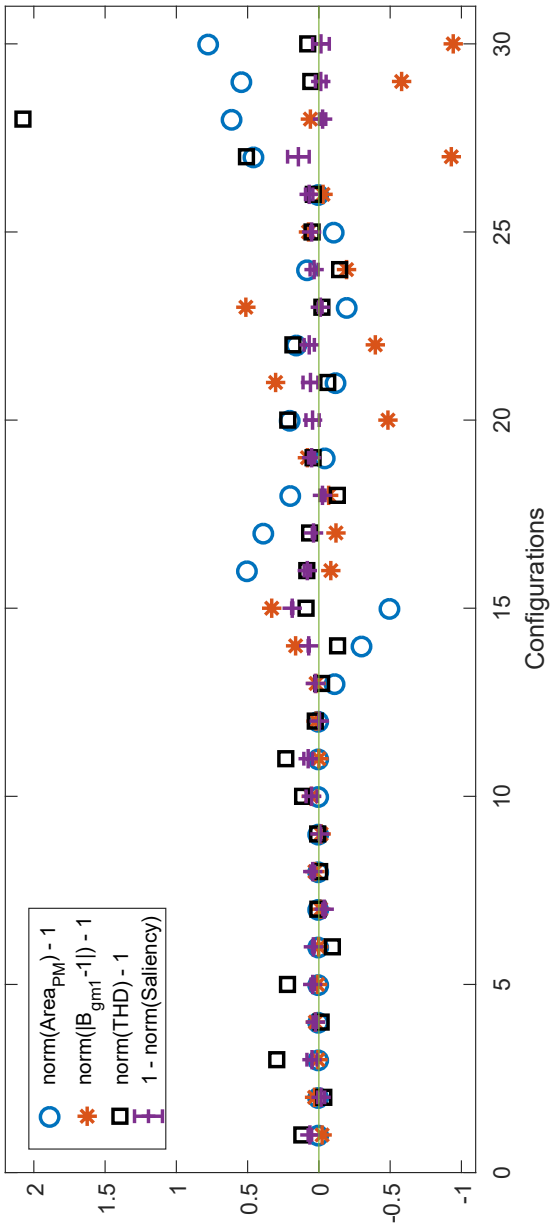

Figure 3.5: Tab. 3.2 results overview. Data are normalized on the basis of the optimal design and rearranged to assist the comparison.

constraint.

Taking the optimal design as reference, the Tab. 3.2 data can be normalized and rearranged for better understanding as in Fig. 3.5, instead of adding the percentage deviations. The 30 rotor configurations in the table are numbered from top to bottom. Every marker above the zero threshold refers to a function objective result worse than the optimum, whereas the markers below identify results better than the optimal design. The saliency ratio markers show both the saturated and unsaturated values. Three considerations can be made.

No geometry variation yields better performances for all the four objectives, so the optimal design belongs indeed to the Pareto front.

Every configuration whose $B_{gm\,1}$ gets closer to 1 T, uses more PM. This is partially expected but it means that the possible $B_{gm\,1}$ improvements from THD(B_{gm}) reduction, obtained adding barriers, are lost to saturate the new rotor bridges introduced. The three barriers optimal design $B_{gm\,1}$ equals that of the LS 600h rescaled accordingly to the respective PM amounts.

The 27^{th} configuration confirms that longer barriers have a low impact on the saliency, unless the thickness is increased proportionally. If too many barriers are introduced, feasibility problems could arise.

These observations suggest that there is limited scope for high number of barriers in automotive traction motors; however, increasing the number of flux barriers can be very useful in other application fields.

The convenience of the presented approach, based on a parameterized analytical model combined with general-purpose optimizers, was evaluated by the computational effort needed to reach the solution, along with the "quality" of the solution itself (assumed to be proportional to the total number of the objective function evaluations). The benchmark is represented by the FEA-based SyR-e toolbox, that is expected to give more accurate outputs (as it takes into account also the iron magnetic nonlinearity) at the expense of increased computational time. The results of this analysis are reported in Tab. 3.3.

Table 3.3: Computational effort comparison.

Algorithm	time (s)	func. eval.
Pareto front search	21	65 378
Pareto refinement	4	9 256
`fmincon`	0.14	403
SyR-e (FEA based)	13 750	3 788

3.7 Spoke-type IPM motors

IPM motors typically make use of expensive rare-earth permanent magnets and, as the emerging economies will increase the demand for these materials, prices will rise further making rare-earth-based solutions less competitive. Researchers have proposed different solutions: synchronous reluctance motors, replace rare-earth PM with ferrite, but probably the most immediate option is the design optimization to reduce the PM mass.

In this section, a saliency enhanced spoke-type rotor geometry is proposed in order to replace the Prius rotor with a 28 % reduction in the PM mass [30]. This approach is studied with a specific analytical model (similar to that presented in section 2.3) and extensive Finite Element simulations.

There are two main options for the IPM rotor geometry: radial or tangential magnetization. Both have pros and cons but the former is usually preferred. However in this case, the rotor mechanical integrity relies on posts and bridges which, if not saturated, would compromise the magnetic anisotropy. Bridge saturation results in a flux leakage that can reach up to 25 % of the PM flux (see Tab. 2.6). An interesting feature of the IPM motor with tangential magnetization, also known as "spoke-type" motor, is the opportunity to open partially the rotor bridges instead of saturating them with flux, and then to use more efficiently the PMs. In this way, the total amount of PM can be significantly reduced without sacrificing the performances [31].

Obviously, the mechanical integrity requires other solutions. This issue has

been tackled thoroughly in [32] and [33] both in structural terms and from the materials point of view with the support of Jaguar Land Rover Ltd. In the solution proposed by [32], [33], the rotor is composed by the ferromagnetic poles (without any mechanical role) and a nonmagnetic rotor hub with the sole purpose of providing mechanical integrity by means of a fir-tree assembly. Another possible approach [34], relies on axial bolts that retain the rotor poles radially and suitable plates at the ends of the rotor which restrain the bolts radially and tangentially. Despite a more complex rotor construction, both these techniques enable the design to achieve simultaneously the magnetic and mechanical optimal performances with no need of high speeds tradeoff.

3.7.1 Conventional saliency optimization

By means of the symbolic convention presented in section 2.3, the saliency ratio ξ of the spoke-type geometry (see Fig. 3.6) results as follows:

$$\xi = \frac{1}{1 - \frac{\frac{4}{\pi}}{(1 + 4 \cdot ASR)\,\frac{\pi}{2}}} \qquad (3.19)$$

$$AS_g = \frac{\pi D}{2p\,g} \qquad (3.20)$$

The ASR and flux barrier aspect ratio symbols have the same meaning as in subsection 2.3.1 but the peculiarities of this rotor topology shall be taken in account. First of all, no lateral (air) barrier is present, then $w_{lb} = 0$ and the $AS_{tb} = \mu_{rec} \cdot w_m / t_m$ expression results simpler. Secondarily, the AS_g has to be redefined according to (3.20). Comparing the (3.19) with (2.64), it should be pointed out that in (3.19) the ASR is multiplied by 4. This means that in the spoke-type geometry, the same flux barrier is 4 times less effective than in the radial magnetization configuration. In spoke-type IPM motors, therefore, the achievable saliency, which is related to the reluctance torque, is lower than in radial magnetization motors. That is one of the reasons why radial magnetization is more widespread among the IPM motors commercially available today. In addition, (3.19) has only one degree of freedom (ASR), whereas in (2.64)

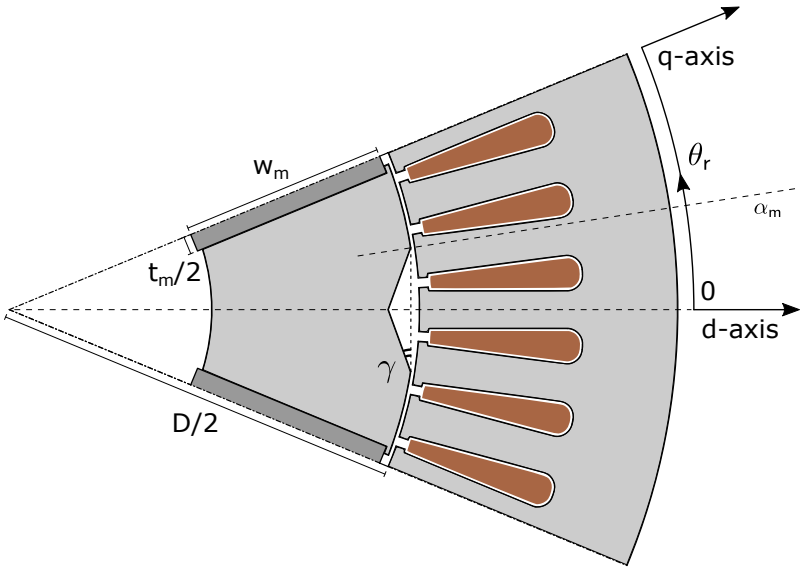

Figure 3.6: One pole circular sector of a spoke-type motor with V-hole.

the independent variables are two: α_m and ASR.

By means of the magnetic potential drops introduced along the d-axis, flux barriers reduce locally the potential difference across the airgap, and so the magnetic flux decreases as well as the L_d inductance, or in other words, the d-axis reluctance rises.

3.7.2 Rotor shaping

Another technique to achieve the same result, and therefore to increase the saliency, might be shaping the rotor surface properly; namely, thickening the airgap locally around the d-axis. As shown in Fig. 3.6, a V-shape hole is introduced whose width and depth are set by α_m and by γ respectively. This technique can be used in conjunction with the flux barrier effect of the PMs, enhancing the saliency and providing two additional degrees of freedom for the design. But this particular rotor configuration deserves more discussion together with a detailed geometric and magnetic analysis (Fig. 3.7).

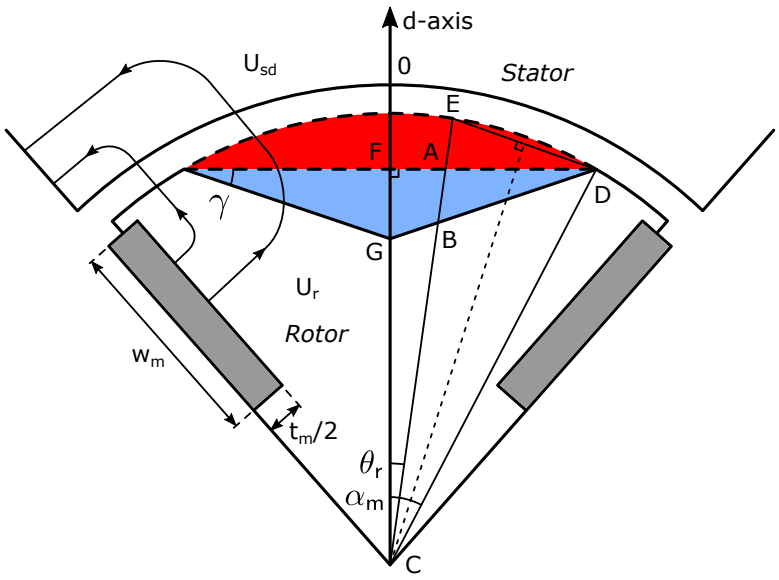

Figure 3.7: Airgap geometry study.

The V-holes airgap expansion term $\Delta g(\theta_r)$ involves radially a circular segment $\Delta g_\circ(\theta_r)$ —red area in Fig. 3.7— and a triangular portion $\Delta g_\triangledown(\theta_r)$ —blue area in Fig. 3.7. θ_r is the mechanical angular coordinate.

$$\Delta g(\theta_r) = \Delta g_\circ(\theta_r) + \Delta g_\triangledown(\theta_r) \tag{3.21}$$

After some trigonometric calculations and applying the sine law to the ADE triangle, $\Delta g_\circ(\theta_r) = \overline{\mathrm{AE}}$ results as follows (3.22).

$$\Delta g_\circ(\theta_r) = \frac{D}{2}\left[1 - \frac{\cos(\alpha_m)}{\cos(\theta_r)}\right] \tag{3.22}$$

Using again the sine law with ABD and then with ACD triangles, yields the $\Delta g_\triangledown(\theta_r) = \overline{\mathrm{AB}}$ expression (3.23).

$$\Delta g_\triangledown(\theta_r) = D\sin(\gamma)\cdot\frac{\sin(\alpha_m - |\theta_r|)}{\cos(\gamma) + \cos(\gamma + 2\,|\theta_r|)} \tag{3.23}$$

As expected, $\Delta g(\pm\alpha_m) = 0$ since $g(\theta_r)$ is a continuous function, and $\Delta g_\triangledown(0)$ equals the geometric height of the V-hole triangular part. In order

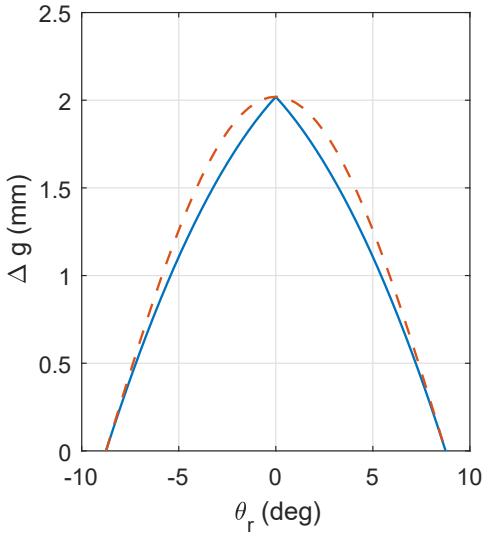

Figure 3.8: Solid blue line: $\Delta g(\theta_r)$ - Dashed red line: cosine approximation.

to proceed with the analysis, (3.21) can be approximated by a cosine function (Fig. 3.8), being an even function. Hence the airgap thickness $g(\theta_r)$ can be expressed through a piecewise function (3.24). Finally, as the magnetic analysis is based on definite integrals over the pole pitch, (3.24) can be approximated further (3.25) by the average value of the airgap variation $\overline{\Delta g}$.

$$g(\theta_r) \simeq \begin{cases} g + \dfrac{D}{2}\left[1 - \cos\left(\alpha_m\right) + \tan(\gamma)\sin\left(\alpha_m\right)\right]\cos\left(\dfrac{\pi}{2}\cdot\dfrac{\theta_r}{\alpha_m}\right) & -\alpha_m \leqslant \theta_r \leqslant +\alpha_m \\ g & \text{elsewhere} \end{cases} \tag{3.24}$$

$$g(\theta_r) \simeq \begin{cases} g + \dfrac{D}{\pi}\left[1 - \cos\left(\alpha_m\right) + \tan(\gamma)\sin\left(\alpha_m\right)\right] = g + \overline{\Delta g} & -\alpha_m \leqslant \theta_r \leqslant +\alpha_m \\ g & \text{elsewhere} \end{cases} \tag{3.25}$$

Since the IPM rotor structure is anisotropic, the magnetic circuit analysis has to be divided along the d-axis and the q-axis.

Following the field lines in Fig. 3.7, by means of Ampere's law the magnetic field H across the airgap (3.26) and PM (3.27) can be expressed in terms of the respective differences between the magnetic potentials U.

$$H_{sd}(\theta_r) \cdot g(\theta_r) = U_r - U_{sd}(\theta_r) \qquad (3.26) \qquad H_m \cdot \frac{t_m}{2} = -U_r \qquad (3.27)$$

While the stator potential U_{sd} is given by Ampere's law, the rotor potential U_r has to be determined.

$$U_{sd}(\theta_r) = \int K_{sd}(\theta'_r)\frac{D}{2}d\theta'_r = -\frac{\widehat{K}_{sd}D}{2p}\cos(p\,\theta_r) \qquad (3.28)$$

where $K_{sd}(\theta_r) = \widehat{K}_{sd} \cdot \sin(p\,\theta_r)$ is the d-axis linear current density. Recalling the constitutive relations for the air and magnets, the equations (3.26) and (3.27) become:

$$B_{sd}(\theta_r) = \frac{\mu_0}{g(\theta_r)}\left[U_r - U_{sd}(\theta_r)\right] \qquad (3.29)$$

$$B_m = -\frac{2\,\mu_{rec}\,\mu_0}{t_m}\,U_r \qquad (3.30)$$

thus providing the flux densities B expressions. The magnetic flux of the stator relative to a single pole can be found through integration of (3.29).

$$\begin{aligned}
\phi_{sd} &= 2\int_0^{\frac{\pi}{2p}} B_{sd}(\theta'_r)\frac{D\,L_{stk}}{2}d\theta'_r \\
&= \int_0^{\frac{\alpha^e_m}{p}} B_{sd}(\theta'_r)D\,L_{stk}\,d\theta'_r + \int_{\frac{\alpha^e_m}{p}}^{\frac{\pi}{2p}} B_{sd}(\theta'_r)D\,L_{stk}\,d\theta'_r \\
&= \frac{\mu_0 D\,L_{stk}}{(g+\overline{\Delta g})\cdot p}\left[U_r\,\alpha^e_m + \frac{\widehat{K}_{sd}D}{2p}\sin(\alpha^e_m)\right] + \\
&+ \frac{\mu_0 D\,L_{stk}}{g\cdot p}\left\{\left(\frac{\pi}{2} - \alpha^e_m\right)U_r + \frac{\widehat{K}_{sd}D}{2p}\left[1 - \sin(\alpha^e_m)\right]\right\}
\end{aligned} \qquad (3.31)$$

Now, Gauss law can be used in order to find the rotor magnetic potential U_r expression.

$$\phi_{sd} = 2\,\phi_m = 2\,w_m\,L_{stk}\,B_m \qquad (3.32) \qquad U_r = \frac{\widehat{K}_{sd}\,D}{2p}\cdot U'_r \qquad (3.33)$$

It is also possible to identify a geometry-related factor U'_r in (3.33) given by

$$U'_r = -\frac{1-\dfrac{\sin(\alpha^e_m)}{1+\dfrac{g}{\overline{\overline{\Delta g}}}}}{\dfrac{\pi}{2}\,(1+4\,ASR)-\dfrac{\alpha^e_m}{1+\dfrac{g}{\overline{\overline{\Delta g}}}}} \qquad (3.34)$$

For the q-axis analysis almost the same steps can be repeated but in this case, there is not the U_r term as the PMs have negligible influence on the q-axis armature reaction field. Therefore the equations change as follows.

$$U_{sq}(\theta_r) = \int K_{sq}(\theta'_r)\frac{D}{2}d\theta'_r = -\frac{\widehat{K}_{sq}D}{2p}\sin(p\,\theta_r) \qquad (3.35)$$

$$H_{sq}(\theta_r)\cdot g(\theta_r) = -U_{sq}(\theta_r) \qquad (3.36)$$

$$B_{sq}(\theta_r) = -\frac{\mu_0}{g(\theta_r)}\cdot U_{sq}(\theta_r) \qquad (3.37)$$

where $K_{sq}(\theta_r) = -\widehat{K}_{sq}\cdot\cos(p\,\theta_r)$ is the q-axis linear current density. Computing the d/q-axis flux $\phi_{sd/q}$ from the fundamental term of the $B_{sd/q}$ distribution, the saliency ratio ξ expression results:

$$\phi_{sd} = \frac{2\,D\,L_{stk}}{\pi}\int_{-\frac{\pi}{2p}}^{+\frac{\pi}{2p}} B_{sd}(\theta'_r)\cos(p\,\theta'_r)d\theta'_r \qquad (3.38)$$

$$\begin{aligned}\phi_{sq} &= \frac{2\,D\,L_{stk}}{\pi}\int_{-\frac{\pi}{2p}}^{+\frac{\pi}{2p}} B_{sq}(\theta'_r)\sin(p\,\theta'_r)d\theta'_r \\ &= \frac{\mu_0\,\widehat{K}_{sq}\,L_{stk}}{2\,g}\left(\frac{D}{p}\right)^2\left[1-\frac{2\,\alpha^e_m-\sin(2\,\alpha^e_m)}{\pi\left(1+\dfrac{g}{\overline{\overline{\Delta g}}}\right)}\right]\end{aligned} \qquad (3.39)$$

$$\xi = \frac{1 - \dfrac{2\,\alpha_m^e - \sin(2\,\alpha_m^e)}{\pi\left(1 + \dfrac{g}{\overline{\Delta g}}\right)}}{1 - \dfrac{2\,\alpha_m^e + \sin(2\,\alpha_m^e)}{\pi\left(1 + \dfrac{g}{\overline{\Delta g}}\right)} + \dfrac{4\,U_r'}{\pi}\left[1 - \dfrac{\sin(\alpha_m^e)}{1 + \dfrac{g}{\overline{\Delta g}}}\right]} \tag{3.40}$$

As expected, the degrees of freedom are three: α_m, ASR and $g/\overline{\Delta g}$.

Although this model is based on a general linearity assumption, it has been implemented considering also the magnetic saturation effect [35]. By means of an iterative algorithm, the airgap is virtually expanded in order to incorporate the magnetic voltage drops in the iron paths along d-axis and q-axis. Two saturation factors are defined, $k_{sat\,d}$ and $k_{sat\,q}$, to take into account the different flux magnitude in the d-axis and q-axis, then the airgap is increased locally on the basis of these factors. Since the q-axis magnetic flux is larger than the d-axis one, also $k_{sat\,q} > k_{sat\,d}$, so this effect tends to counteract the rotor magnetic anisotropy and limits the maximum achievable saliency ratio.

3.7.3 FEA validation

The proposed model has been validated by means of a comparison with FEM simulations. Fig. 3.9 collects the cross-sections of all the nine rotor geometries examined in this work. The color-map denotes the flux density level: from 10^{-3} T (cyan) to 2 T (magenta). As shown in Tab. 3.4, the results are in good agreement both for the saliency ratio and the reluctance torque T_{rel}, except for higher α_m, due to the cosine approximation (Fig. 3.8). In the first six considered geometries, only the V-holes are varied keeping the PM reference aspect ratio AS_{tb} unchanged, then in the last three the width and thickness of the PMs are modified and the AS_{tb} relative changes are reported. Moreover, Fig. 3.10 illustrates the model estimation of the saliency ratio setting $\gamma = 5°$ and sweeping α_m and AS_{tb}. The combined effect of the V-holes and PM flux barriers can be observed as well as the presence of an optimal α_m angle (when

Table 3.4: Simulation results for model validation. $\hat{I} = 150\ A$ and $\gamma = 5°$. The selected design equivalent to the Prius motor is highlighted in yellow.

Test		Analytic		FEM				
α_m^e (deg)	AS_{tb} (relative)	Saliency	T_{rel} (N m)	Saliency	T_{rel} (N m)	$B_{gm\,1}$ (T)	$B_{gm\,3}$ (T)	Fig. #
5	×1	1.63	77	1.6	67.7	1	0.33	3.9a–3.15a
20	×1	1.66	77.4	1.7	70	0.95	0.46	3.9b–3.15b
35	×1	1.78	80	1.8	73	0.84	0.65	3.9c–3.15c
50	×1	1.92	72.4	1.9	74.5	0.71	0.74	3.9d–3.15d
65	×1	1.64	25.7	2	68.2	0.56	0.66	3.9e–3.15e
80	×1	1.16	3	1.7	49.6	0.43	0.39	3.9f–3.15f
35	×1/0.25	1.24	36	1.4	42.2	1.32	0.9	3.9g–3.15g
35	×1/2.5	2	78	2.1	72.7	0.83	0.58	3.9h–3.15h
35	×1/1.75	1.98	84	1.9	65	1	0.69	3.9i–3.15i

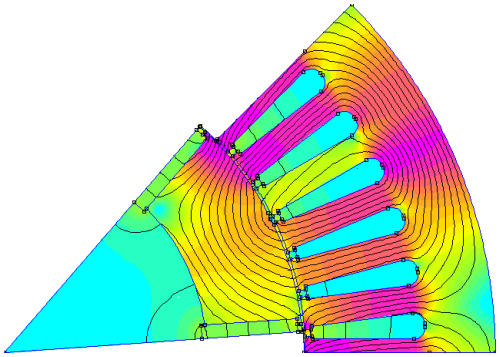

(a)

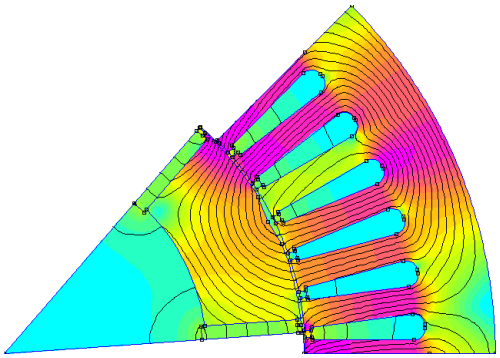

(b)

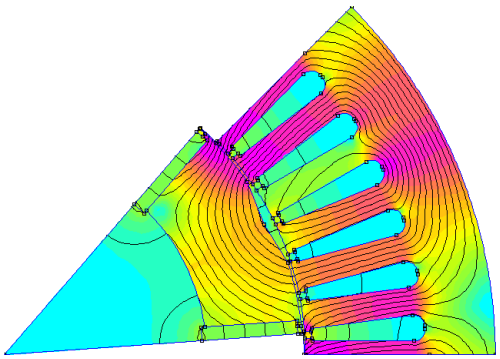

(c)

Figure 3.9: Cross-sections of the rotor geometries analyzed with FEA. The color-map displays the flux density: from 10^{-3} T - cyan, to 2 T - magenta.

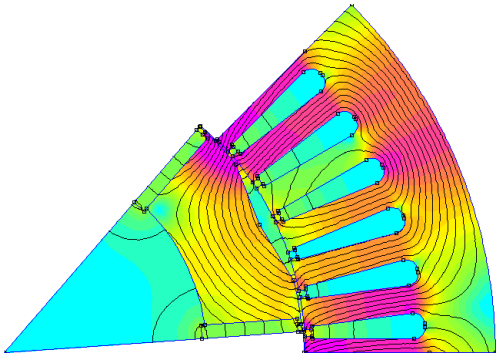

(d)

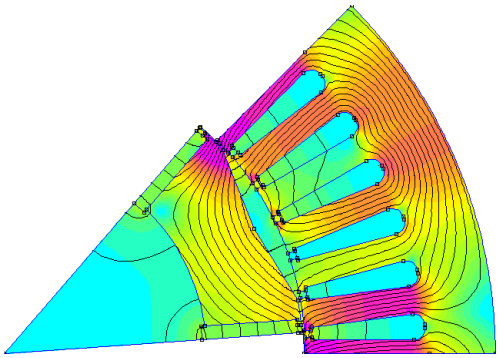

(e)

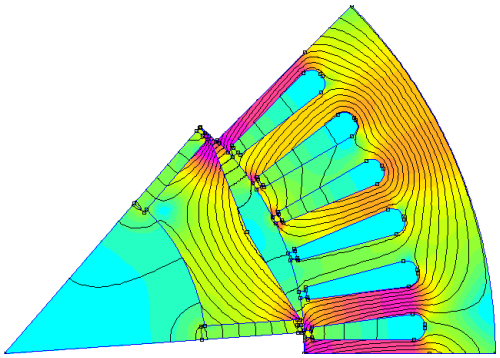

(f)

Figure 3.9: Cross-sections of the rotor geometries analyzed with FEA (Cont.).

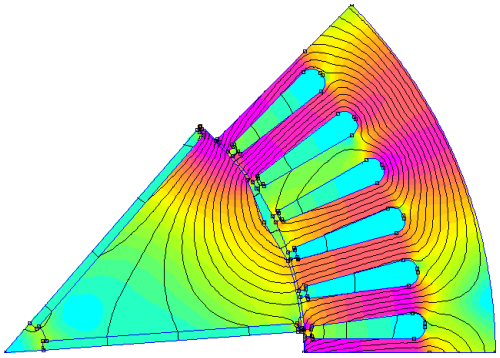

(g)

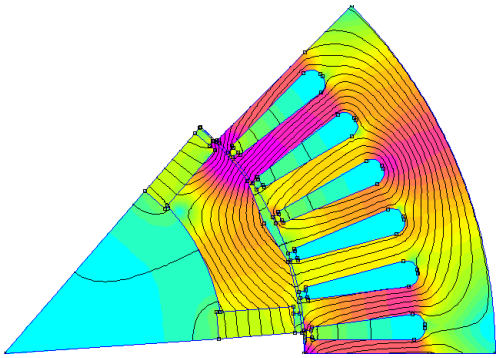

(h)

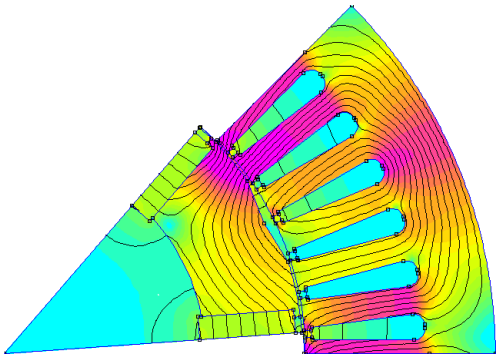

(i)

Figure 3.9: Cross-sections of the rotor geometries analyzed with FEA (Cont.).

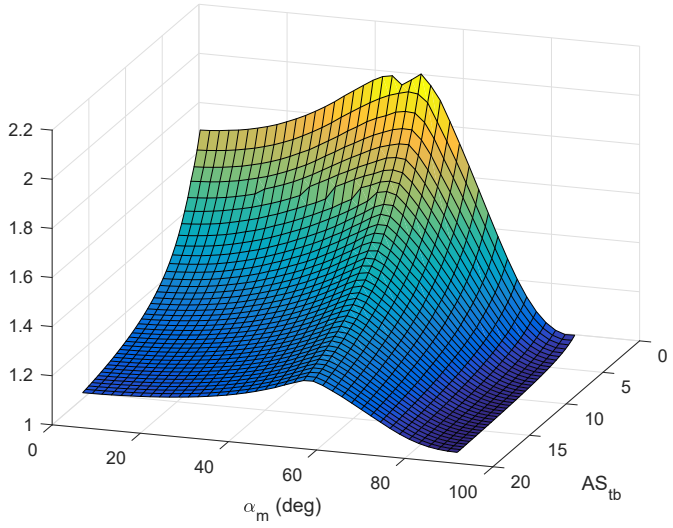

Figure 3.10: Saliency ratio estimated by the model.

too large α_m is used, not only d-axis reluctance is increased but also the q-axis one). Looking at (3.39), it is possible to distinguish the square brackets term, which can decrease ϕ_{sq} as $\overline{\Delta g}$ rises. This demonstrates that too wide V-holes at the airgap, although located on the d-axis, might have an undesirable influence on the q-axis flux also, as can be seen in Figs. 3.9e–3.9f.

3.7.4 Selected design

By means of the analytic model presented above, it has been possible to design a spoke-type rotor, with open bridges and airgap V-shape holes ($\alpha_m^e = 35°$ and $\gamma = 5°$), equivalent to the Prius motor but with PM mass reduced by about 28 %. Its main technical data are highlighted in Tab. 3.4. The two motors have been simulated by means of FEA using a 150 A current (that is the average between the nominal and overload currents) and Figs. 3.11–3.13 compare the performances obtained. Figs. 3.11a–3.11b show the torque maps of the two motors including also the control trajectory for MTPA (Maximum Torque per

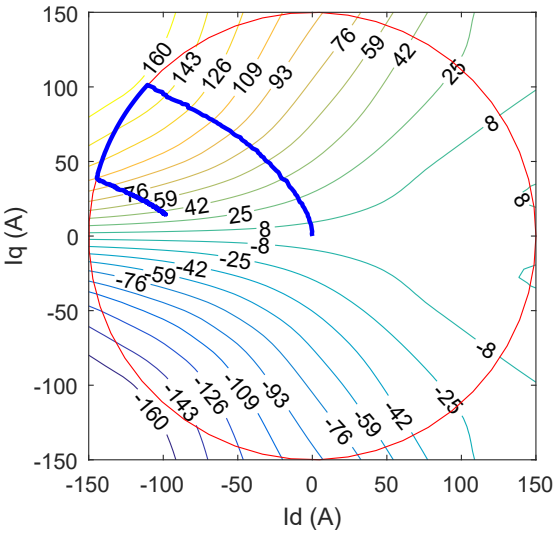

(a) Spoke-type.

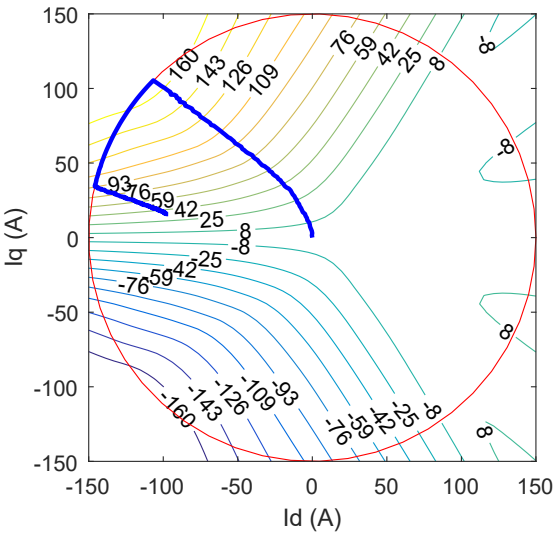

(b) Prius.

Figure 3.11: Torque maps comparison.

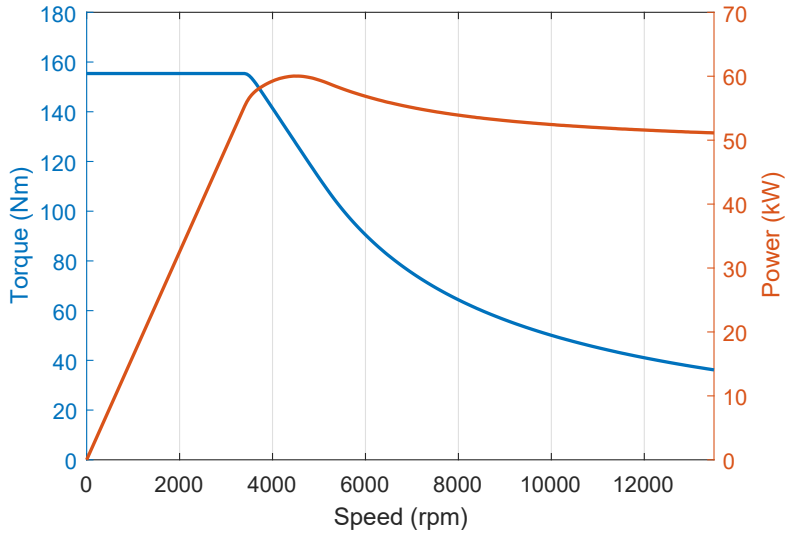

(a) Spoke-type.

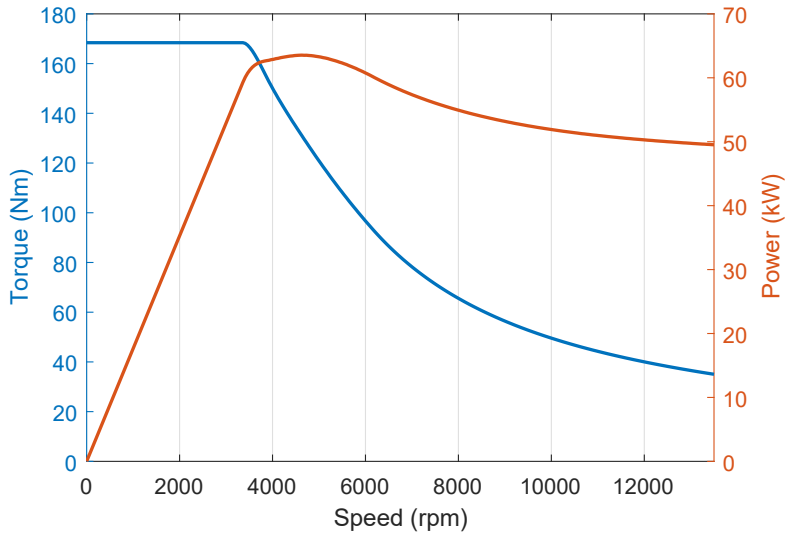

(b) Prius.

Figure 3.12: Dynamic curves comparison.

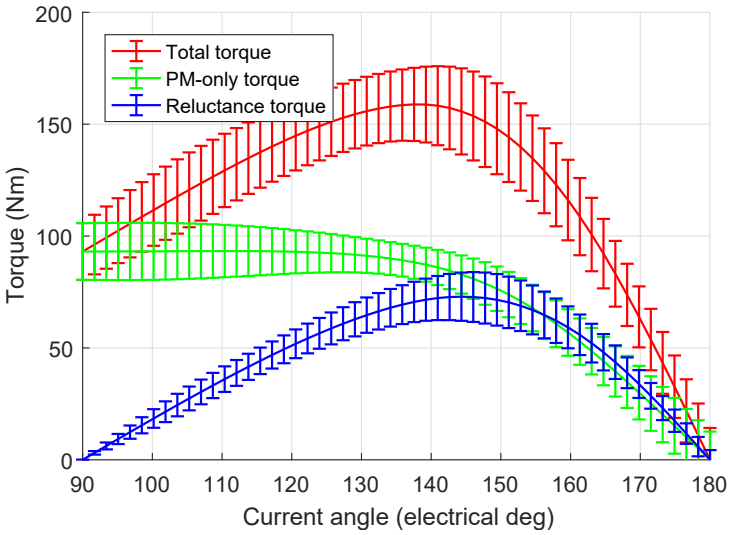

(a) Spoke-type.

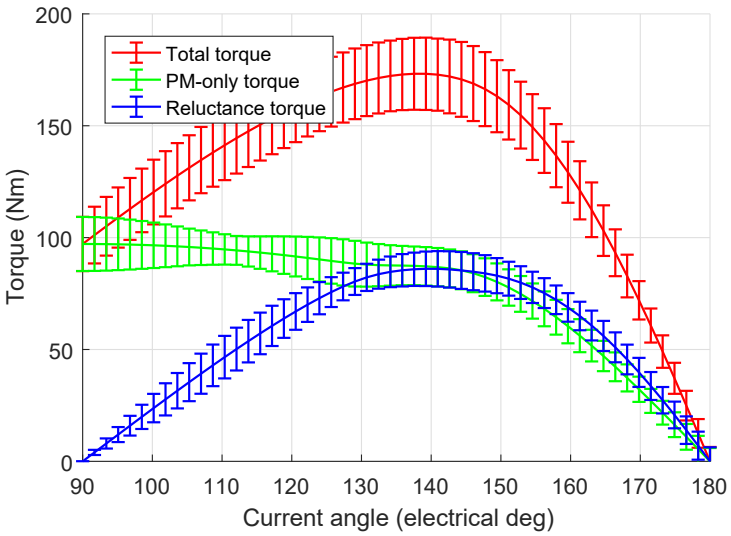

(b) Prius.

Figure 3.13: Torque analysis comparison.

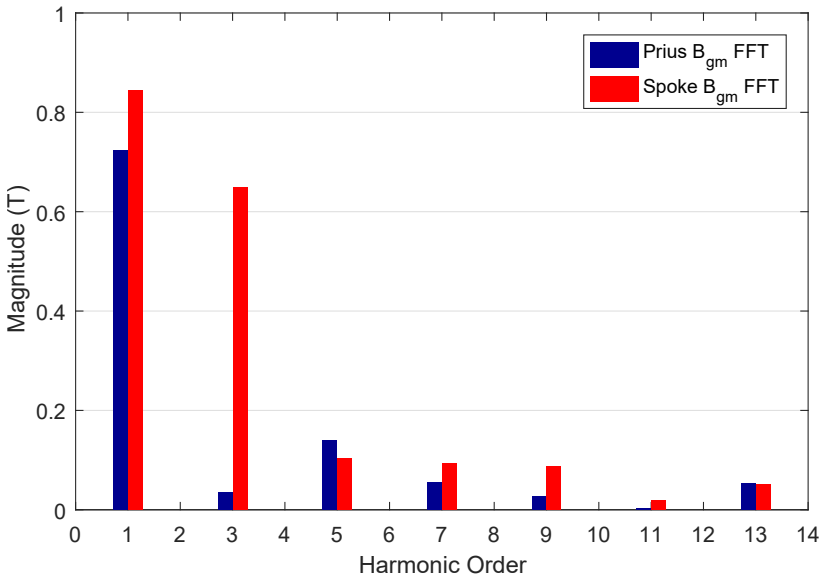

Figure 3.14: Airgap B distortion in no-load condition.

Ampere) and flux weakening, followed by the two maximum torque (and power) - speed curves (Fig. 3.12a–3.12b). As can be observed, the maximum torque and power curves are nearly the same as well as the control trajectories (only in the low speed range, the Prius maximum torque exhibits a slightly higher value). These results are confirmed also by the torque composition analysis (Fig. 3.13a–3.13b). Vertical bars show the torque ripple amplitude without any skewing technique.

Unfortunately, this particular rotor shape has a detrimental effect on the airgap flux density distortion in no-load condition. Looking at the Fig. 3.14 and Tab. 3.4, the third harmonic $B_{gm\,3}$ rises significantly and this increases the magnetic saturation of the motor without any torque gain. This drawback leads also to iron losses significantly higher than usual, especially near the maximum speed, as illustrated in Fig. 3.15. The iron losses have been computed with the Steinmetz equation assuming laminations M250-35A for the stator and rotor core of the machines considered in the analysis, and taking into account the

first nine harmonics of the magnetic flux density B in the iron. The results might be somewhat overestimated, due to the lack of accurate data for the specific losses at higher frequencies, but it is worth noting that, as expected, the iron losses vary accordingly to the $B_{gm\,3}$ (and $B_{gm\,1}$, the fundamental tone) values reported in Tab. 3.4.

Despite the pronounced losses which occur when the speed approaches the top value, the maximum efficiency achievable by most of these machines lies between 95 % and 96.5 %: a very reasonable level. Moreover, the extent of the high-efficiency area observable in the efficiency maps of Fig. 3.16 is adequate, though focused around the lower speeds (up to 7 000 rpm). In conclusion, the spoke-type rotor topology with open bridges and V-holes can provide a useful alternative to the conventional radial magnetization IPM motors for automotive traction applications, although only the low-medium speed range should be used, where the efficiency holds at acceptable levels.

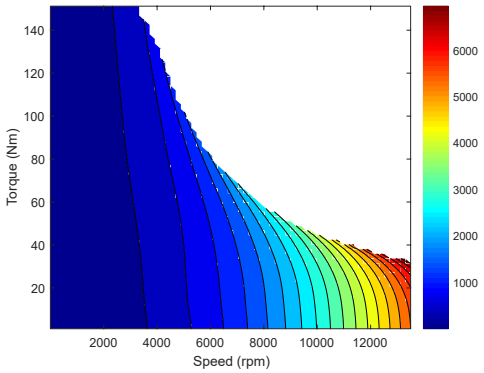

(a)

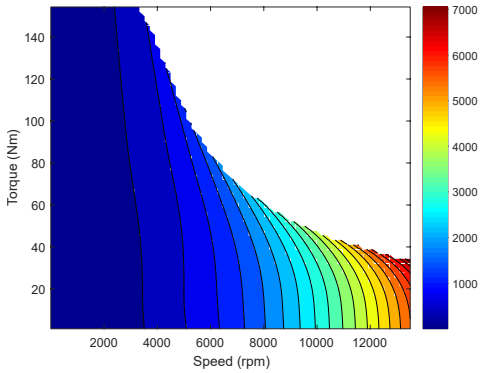

(b)

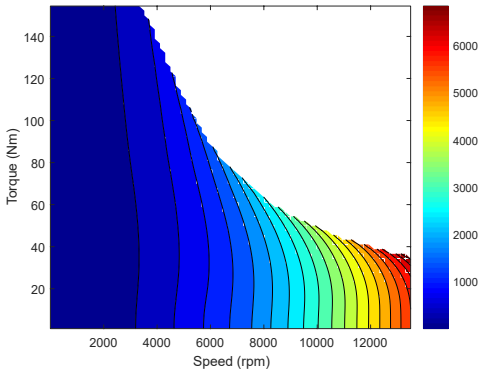

(c)

Figure 3.15: Iron losses maps in watts of the considered configurations.

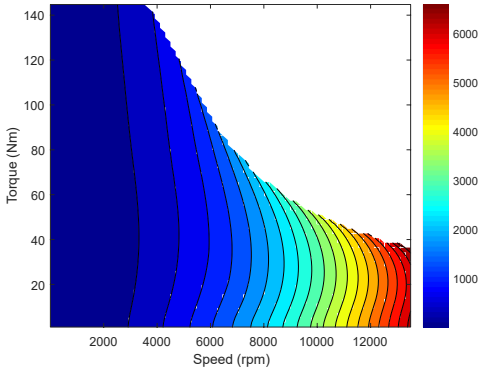

(d)

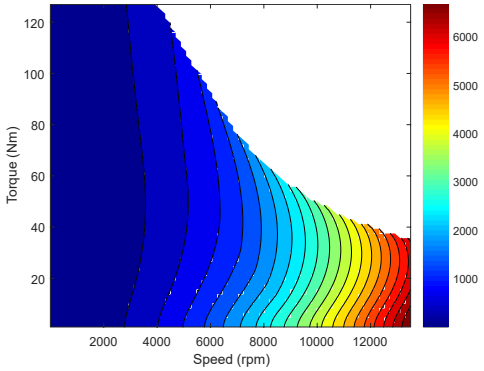

(e)

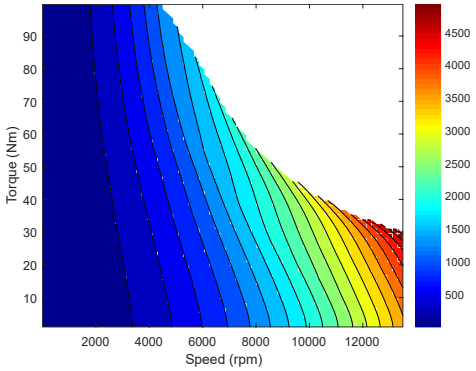

(f)

Figure 3.15: Iron losses maps in watts of the considered configurations (Cont.).

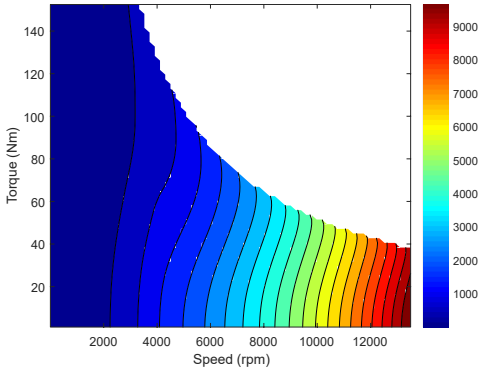

(g)

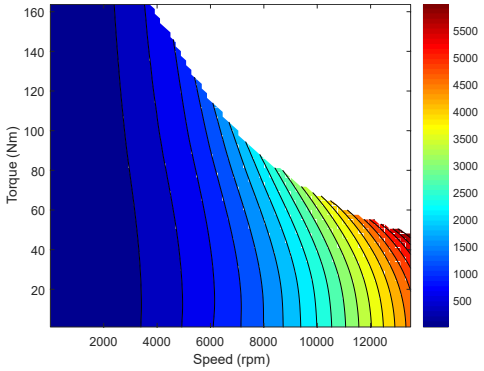

(h)

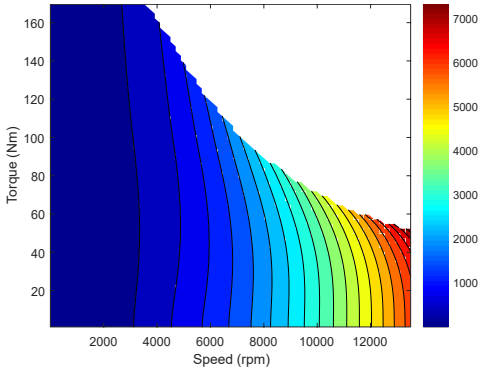

(i)

Figure 3.15: Iron losses maps in watts of the considered configurations (Cont.).

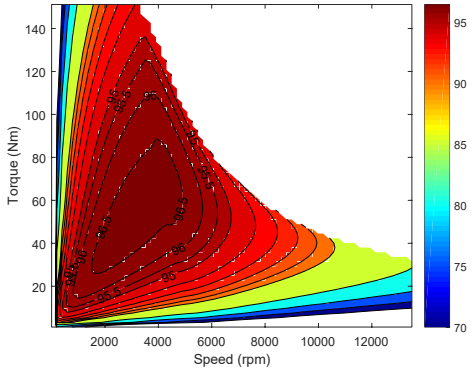

(a)

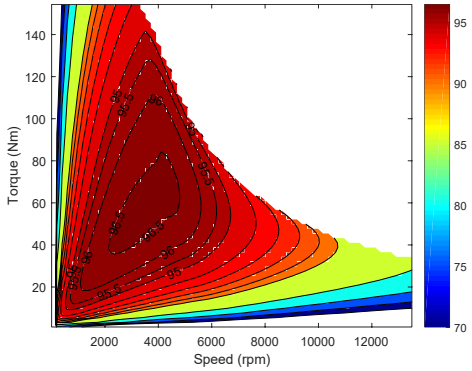

(b)

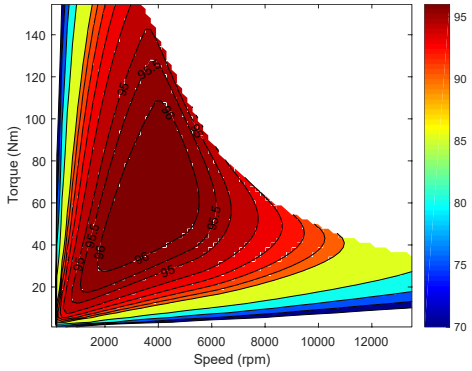

(c)

Figure 3.16: Efficiency maps (in %) of the considered configurations.

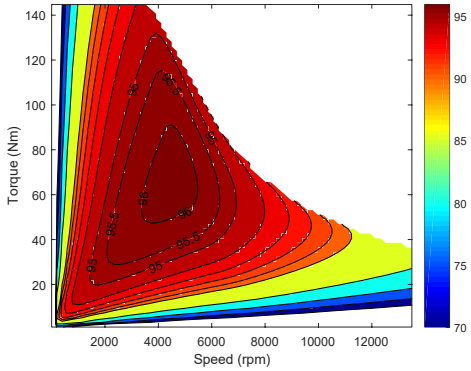

(d)

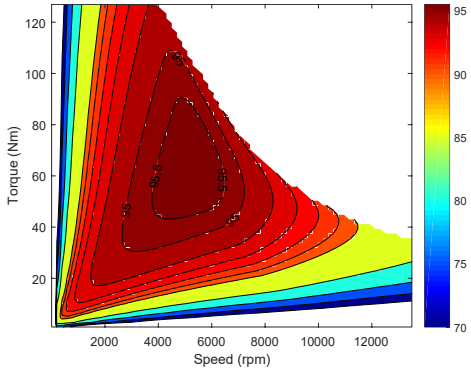

(e)

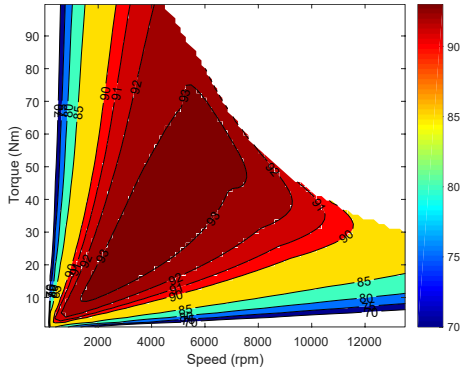

(f)

Figure 3.16: Efficiency maps (in %) of the considered configurations (Cont.).

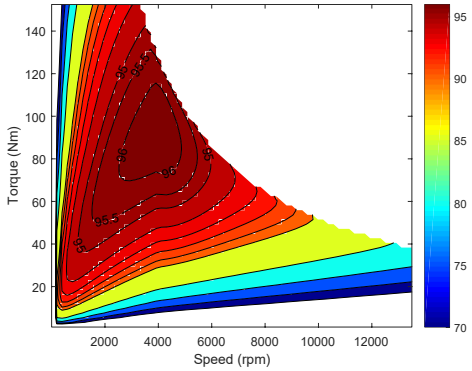

(g)

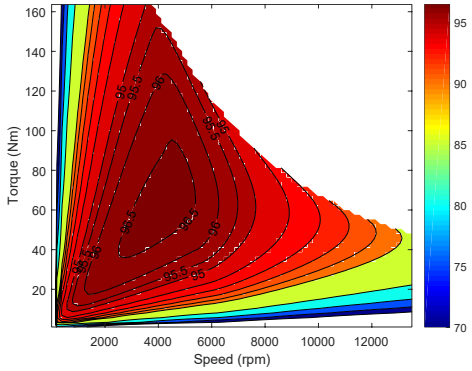

(h)

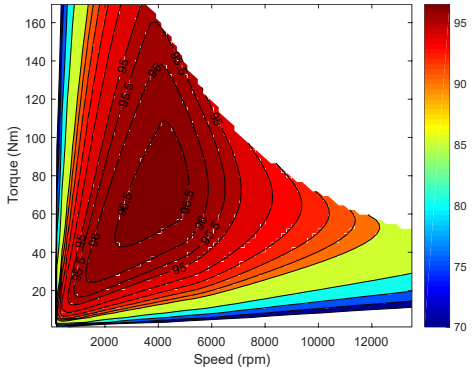

(i)

Figure 3.16: Efficiency maps (in %) of the considered configurations (Cont.).

Chapter 4

New prototype design

After a detailed analysis of the industrial state-of-the-art carried out in chapter 2, and an in-depth discussion of the main design options for the EV traction IPM motors (see chapter 3), here a new prototype design will be described.

The prototype technical specifications come from a possible student formula racing application and are reported in Tab. 4.1. According to the rules, the overall maximum power of the vehicle must not exceed 80 kW. Then, in order to provide the car with an electronic differential, the powertrain will consist of two independent motors. Each motor nominal power P_{nom} is therefore 40 kW and the overload power P_{max} has been set to 70 kW in order to make possible *torque vectoring*. Vehicle dynamic simulations returned the remaining prototype specifications taking into account the vehicle characteristics (e.g.:

Table 4.1: Prototype motor specs.

Symbol	**Value**	**Units**	**Symbol**	**Value**	**Units**
P_{max}	70	kW	P_{nom}	40	kW
T_{max}	160	N m	T_{nom}	80	N m
ω_{max}	20 000	rpm	V_{bus}	600	V
r	10	#	m	3	#

mass, top speed). Despite its original mission, the prototype specifications are also compatible to multi-purpose vehicle modular powertrains.

In the next sections, the most important design steps will be summarized, then additional information about the particular winding scheme will be provided and finally the electromagnetic, dynamic, thermal and mechanical performances will be assessed by means of Finite Element simulations.

4.1 Preliminary design

In order to maximize the machine torque density, the number of pole pairs p is set to 5. If the number of slots per pole and phase was 2 as usual, the motor diameter would be rather large, so $q = 1.5$ has been chosen thus leading to a total number of slots $Q_s = 45$ lower than that of the Prius and LS 600h. As a consequence, the winding scheme must change from a single layer full pitch to a double layer short pitch. This arrangement has a winding factor $k_w = 0.9452$ for the fundamental, as it will be shown in the next section.

Looking at Tab. 2.2, the slot pitch p_s is a relatively "stable" parameter even with various machines configurations, therefore setting $p_s = 8.5\,\mathrm{mm}$, the prototype inner diameter can be found:

$$D = \frac{p_s\, Q_s}{\pi} = \frac{8.5 \times 45}{\pi} = 121.7\,\mathrm{mm}$$

The maximum current amplitude $\hat{I}$ selected to feed this motor is 180 A. For traction applications, the electrical machines typically adopt water cooling systems, and it enables to use rather high electric loading levels: $\widehat{K}_s = 160\,\mathrm{A\,mm^{-1}}$ and $J_s \simeq 30\,\mathrm{A\,mm^{-2}}$. From (2.18):

$$N_s = \frac{160 \times \pi \times 121.7}{3 \times 0.9452 \times 180} = 120$$

and from (2.3)–(2.4):

$$n_{cs} = n_c = \frac{3 \times 120}{45} = 8$$

since n_{pp} has been set to 1.

Similarly, from (2.13) and (2.17):

$$S_c = S_{c\,eq} = \frac{\hat{I}}{J_s\sqrt{2}} = \frac{180}{30\sqrt{2}} = 4.24\,\text{mm}^2$$

For this prototype, a wire diameter $d_c = 0.75\,\text{mm}$, close to that of the BMW i3, has been selected in order to keep under control the possible skin effect due to the high maximum frequency. The wire cross-section surface S_{1c} results $0.4418\,\text{mm}^2$ and then

$$n_{cc} = \frac{S_c}{S_{1c}} = \frac{4.24}{0.4418} \simeq 10$$

As the number of wires per conductor n_{cc} has been rounded to the nearest higher integer, the S_c, $S_{c\,eq}$ and J_s values have to be updated:

$$S_c = S_{c\,eq} = 4.418\,\text{mm}^2 \qquad J_s = 28.8\,\text{A mm}^{-2}$$

A fill factor $k_{fill} = 0.35$ has been chosen (lower than in Prius and LS 600h) to account for the additional insulation in the slots of a double layer winding.

$$S_{Cu} = n_c \cdot S_c = 35.343\,\text{mm}^2 \qquad S_{slot} = \frac{S_{Cu}}{k_{fill}} = 101\,\text{mm}^2$$

Now, recalling (2.28) and the other related formulas in section 2.3, the motor active volume can be determined.

$$\widehat{K}_{sd} = \widehat{K}_s \cos(\alpha_i^e) \qquad (4.1)$$

$$\widehat{K}_{sq} = \widehat{K}_s \sin(\alpha_i^e) \qquad (4.2)$$

$$\widehat{B}_{sd} = \frac{\mu_0}{g''} \cdot \frac{\widehat{K}_{sd}\,D}{2p} \cdot \frac{1}{\xi} \qquad (4.3)$$

$$\widehat{B}_{sq} = \frac{\mu_0}{g''} \cdot \frac{\widehat{K}_{sq}\,D}{2p} \qquad (4.4)$$

where $g'' = k_{sat} \cdot g'$ is the effective airgap due to the iron magnetic saturation.

Assuming a convenient and reasonable value for the maximum torque current angle $\alpha_i^e = 135°$, a Carter coefficient $k_c = 1.065$, a saturation coefficient $k_{sat} = 1.8$, a saliency ratio $\xi = 2.6$ and a $\widehat{B}_{gm} = 0.8\,\text{T}$:

$$\widehat{K}_{sd} = -\widehat{K}_{sq} = -112\,\text{A mm}^{-1} \qquad \widehat{B}_{sd} = -\frac{\widehat{B}_{sq}}{\xi} = -0.43\,\text{T}$$

$$\widehat{K}_{sq} = 112\,\text{A mm}^{-1} \qquad \widehat{B}_{sq} = 1.12\,\text{T}$$

The assumptions about ξ and $\widehat{B}_{gm}$ are based on Tabs. 2.5–2.6, but must be verified at the end of the design calculations, as well as the other parameters such as k_{sat}.

Since $\widehat{B}_{gm}$ and $\widehat{B}_{sd}$ are airgap flux density components of $\widehat{B}_g$ orthogonal to $\widehat{B}_{sq}$,

$$\widehat{B}_g = \sqrt{\left(\widehat{B}_{gm} + \widehat{B}_{sd}\right)^2 + \widehat{B}_{sq}^2} = \sqrt{(0.8 - 0.43)^2 + 1.12^2} = 1.18\,\mathrm{T}$$

By means of the following flux tube relationship, it is possible to determine the teeth width w_t and then inner slot width w_s, as $p_s = w_s + w_t$.

$$\widehat{B}_g \cdot p_s \cdot L_{stk} = \widehat{B}_t \cdot w_t \cdot L_{Fe} \tag{4.5}$$

where $\widehat{B}_t$ is the peak flux density in tooth and $L_{Fe} = k_{pack} \cdot L_{stk}$.

Since the maximum speed of the prototype is rather high as well as the number of poles, a low specific losses lamination M250-35A has been selected. For a lamination so thin, k_{pack} is about 0.96. Therefore, taking the maximum possible values of $\widehat{B}_g \simeq 1.2\,\mathrm{T}$ and of $\widehat{B}_t = 1.85\,\mathrm{T}$ (the iron saturation value with a slight safety margin), from (4.5):

$$w_t = \frac{1.2}{1.85} \cdot \frac{1}{0.96} \cdot 8.5 = 5.7\,\mathrm{mm}$$

and w_s results 2.8 mm.

By means of the trapezoidal approximation (2.15), the slot height h_s and the outer slot width w_{se} can be found:

$$h_s = \frac{Q_s}{2\pi}\left(\sqrt{w_s^2 + \frac{4\pi}{Q_s}S_{slot}} - w_s\right) = 22.9\,\mathrm{mm}$$

$$w_{se} = \frac{\pi \cdot (D + 2\,h_s)}{Q_s} - w_t = 6\,\mathrm{mm}$$

Now k_{sat} can be computed to check the previous assumptions. It is defined as the ratio between the sum of all the magnetic potential drops along the flux

path and only the potential drop through the airgap.

$$k_{sat} = \frac{\sum H \cdot l}{H_g \cdot g'} = \frac{\dfrac{B_g}{\mu_0}\, g' + H_t\, h_s + H_{bi}\, l_{bi}}{\dfrac{B_g}{\mu_0}\, g'} \simeq 1.8$$

where H_t is the tooth magnetic field corresponding to B_t in the M250-35A magnetization curve, whereas $H_{bi}\, l_{bi}$ is the potential drop related to the stator back-iron.

The assumptions are therefore valid and so the active volume can be obtained through (2.28):

$$\left(\frac{\pi}{4}\, D^2\, L_{stk}\right) \left[(0.8 - 0.43)\, 112 \cdot 10^3 - 1.12 \times (-112 \cdot 10^3)\right] = 160$$

By substituting $D = 121.7\,\text{mm}$, the stack length results:

$$L_{stk} = 82.4\,\text{mm}$$

Finally, the back-iron height h_{bi} can be calculated. As explained in section 3.2, the magnetic flux of each pole splits in two halves and each half goes to the nearest adjacent pole through the stator back-iron [15].

$$\phi_g = \frac{D\, L_{stk}}{p} \cdot \widehat{B}_g = \frac{121.7 \cdot 10^{-3} \times 82.4 \cdot 10^{-3}}{5}\, 1.18 = 0.0024\,\text{Wb}$$

$$\phi_{bi} = \frac{\phi_g}{2} = \frac{0.0024}{2} = 0.0012\,\text{Wb}$$

Again, considering a magnetic saturation limit $B_{biMAX} = 1.85\,\text{T}$ in the back-iron, results:

$$h_{bi} = \frac{\phi_{bi}}{L_{Fe}\, B_{biMAX}} = \frac{0.0012}{82.4 \cdot 10^{-3} \times 0.96 \times 1.85} = 8\,\text{mm}$$

and all the elements necessary to find the stator outer diameter D_e are available.

$$D_e = D + 2\, h_s + 2\, h_{bi} = 183.5\,\text{mm}$$

Obviously, this is only a preliminary design and all the machine parameters are to be checked with FE simulations and adjusted where necessary. For this reason, the final machine parameters in Tab. 4.2 and 4.3, could be slightly different.

4.1.1 Flux weakening

Before moving on to the next topic, some preliminary considerations about the FW capabilities and the maximum reachable speed.

As $\omega_{max} = 20\,000$ rpm, the maximum control frequency is

$$f = \frac{p\,\omega_{max}}{60} = \frac{5 \times 20000}{60} = 1\,667\,\text{Hz}$$

and the corresponding angular frequency $\omega_e = 10\,472$ rad/s.

Since the $V_{bus} = 600$ V and assuming a space-vector PWM modulation, the inverter maximum fundamental voltage amplitude is $V_{MAX} = V_{bus}/\sqrt{3} \simeq 330$ V and the related flux linkage is $\widehat{\Lambda} = V_{MAX}/\omega_e = 330/10\,472 = 0.03$ V s. Therefore the corresponding flux ϕ_g and airgap flux density $\widehat{B}_g$ are:

$$\phi_g = \widehat{\Lambda}\,\frac{2}{k_w\,N_s} = 0.0005\,\text{Wb} \qquad \widehat{B}_g = \phi_g\,\frac{p}{D\,L_{stk}} = 0.277\,\text{T}$$

Setting the current angle to the maximum theoretical value for FW $\alpha_i^e = 180°$ leads to a negligible $\widehat{B}_{sq} \simeq 0$ and a $\widehat{B}_{sd} = -0.6$ T. This yields a $\widehat{B}_g = 0.8 - 0.6 = 0.2\,\text{T} < 0.277\,\text{T}$. It means that a current angle value suitable to reach the maximum speed rating of this prototype exists. To go further into detail, FEA is needed because the strong approximations made in this section (like a single saturation coefficient for both the frame axes) deny the possibility to achieve additional and reliable information. A more detailed analysis will be provided in section 4.3 using FE simulations.

4.1.2 Rotor geometry

For the rotor geometry, a two flux barrier modular scheme composed by three NdFeB magnets per pole (similar to the LS 600h) has been chosen since it has proved to be one of the best solution. Then, an optimization process, based on the model described in section 2.3 and 3.6, has sized properly the rotor elements leading to the CAD drawing in Fig. 4.1.

Table 4.2 reports the final design data.

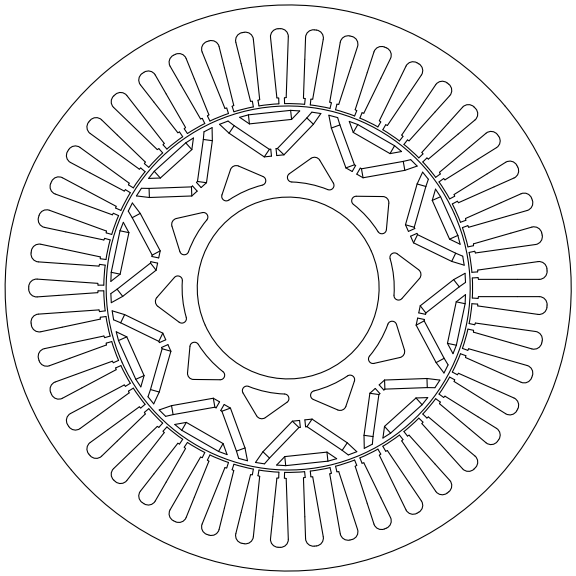

(a) Prototype cross-section CAD

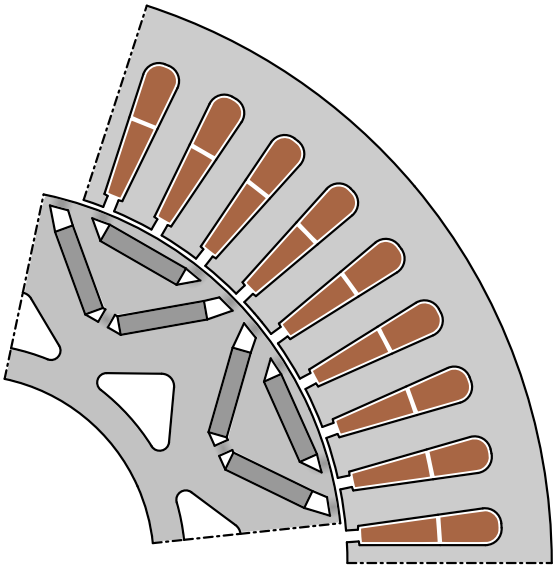

(b) Prototype circular sector drawing (two poles)

Figure 4.1: Prototype motor geometry.

Table 4.2: Prototype motor data.

Symbol	Value	Units	Symbol	Value	Units
P_{max}	70	kW	P_{nom}	40	kW
T_{max}	160	N m	T_{nom}	80	N m
ω_{max}	20 000	rpm	V_{bus}	600	V
m	3	#	p	5	#
Q_s	45	#	q	1.5	#
D_e	186.83	mm	D	121.7	mm
D_r	120.1	mm	D_a	60	mm
g	0.8	mm	L_{stk}	98.3	mm
y_q	4.5	#	τ_p	38.23	#
α_s	8	deg.	p_s	8.5	mm
h_{bi}	7.8	mm	w_t	5.7	mm
h_s	22.76	mm	w_{so}	1.88	mm
h_m	3	mm	w_m	14	mm
n_c	8	#	n_{cc}	10	#
n_{pp}	1	#	n_{cs}	8	#
N_s	120	#	N_{sc}	15	#
d_c	0.75	mm	L_{lam}	0.35	mm
k_{fill}	0.35	#	k_{pack}	0.96	#
$PMs/2p$	3	#	G_{PM}	0.94	kg
$G_{Fe\,stat}$	8.1	kg	$G_{Fe\,rot}$	4.42	kg

4.2 Winding

So far, only single layer full pitch windings have been examined. In this section, another winding arrangement is analyzed: this prototype has a dual layer short pitch scheme, see Fig. 4.2. In Fig. 4.3 the vertical segments (distinguished by solid and dashed lines) denote the slot halves: each pair of segments represent one of 45 numbered slots. Obviously, since the number of turns per slot $n_c = 8$ is even, in each slot half there are 4 turns, as illustrated near the end-windings.

Figure 4.4 compares the star of slots of the Prius and LS 600h full pitch winding to that of the prototype short pitch winding. The three phases are highlighted by the colored triangle pairs: green, ligh blue and yellow. The number of back-emf vectors is different in Fig. 4.4a and 4.4b, as the machine periodicity t, namely the greatest common divisor of Q_s and p, is 4 for Prius and LS 600h, corresponding to $48/4 = 12$ vectors, and 5 for the prototype, corresponding to $45/5 = 9$ vectors.

As Fig. 4.5 illustrates, the fundamental winding factors of the two schemes are similar but the short pitch exhibits not null winding factors also for the even order harmonics. Even harmonics are created by the winding distribution patterns which does not repeat on pole basis, as the even components of the airgap magnetomotive force (MMF) spectrum created by the coils of one pole are not fully eliminated by those of the adjacent pole [36]. However the even order winding factors of this arrangement does not reach serious levels.

Most of the analyses shown in this section have been carried out by means of the open source software *Dolomites* [37].

Table 4.3 reports the prototype winding main data.

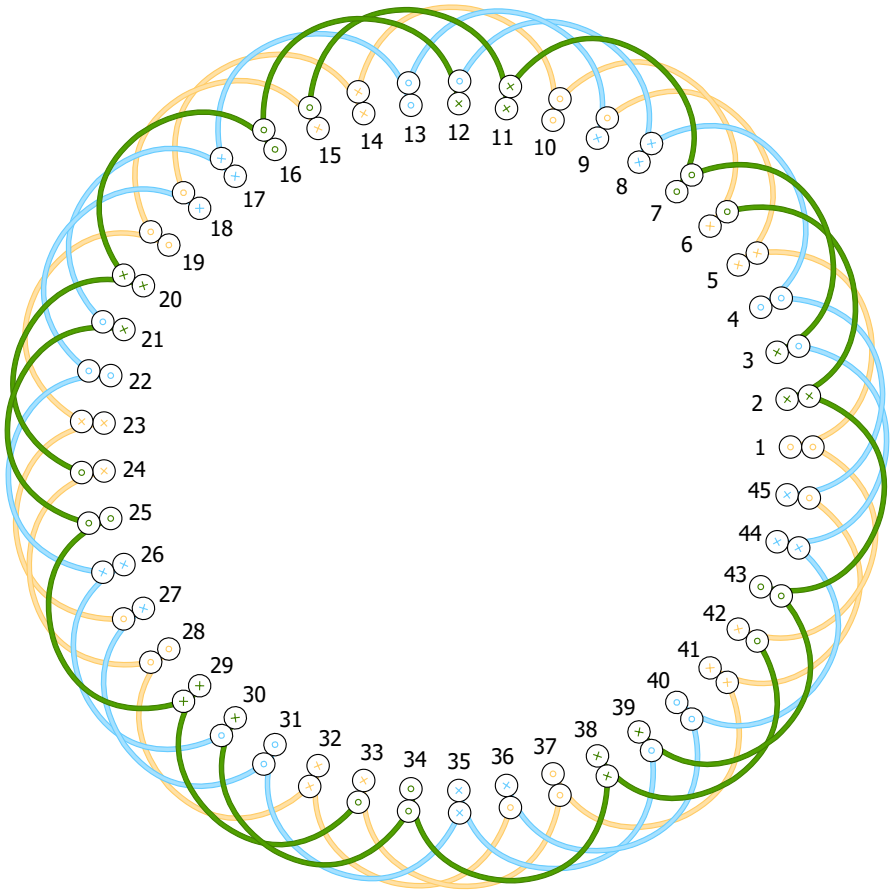

Figure 4.2: Prototype short pitch winding scheme.

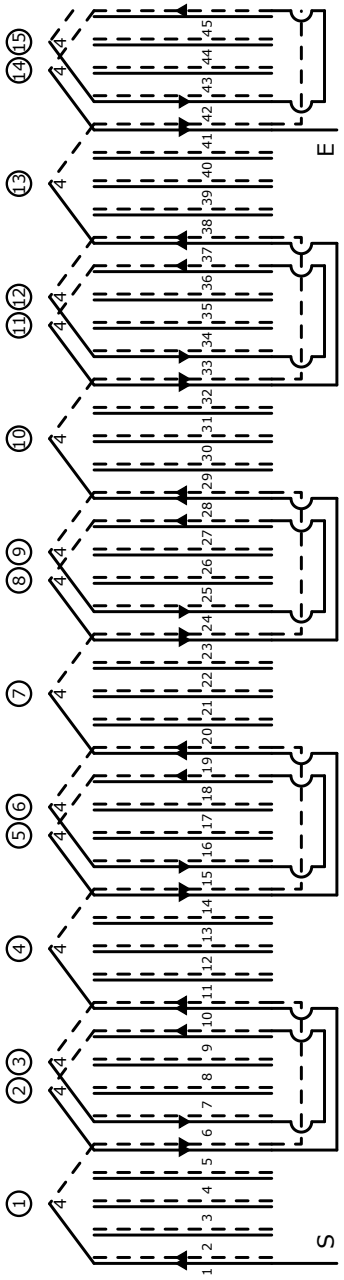

Figure 4.3: Winding arrangement of the prototype (single phase).

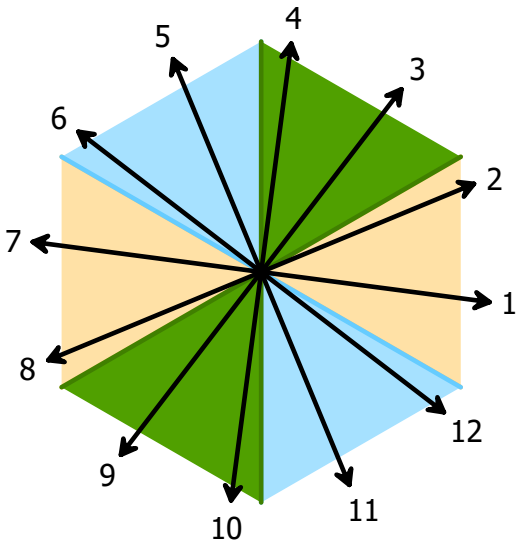

(a) Toyota/Lexus full pitch

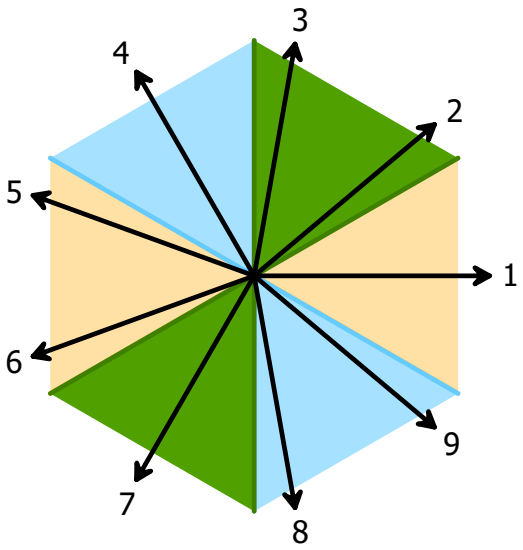

(b) Prototype short pitch

Figure 4.4: Windings stars of slots.

Table 4.3: Prototype winding parameters summary.

Symbol	$\hat{\mathrm{I}} = 90\,\mathrm{A}$	$\hat{\mathrm{I}} = 180\,\mathrm{A}$	**Units**
k_w	0.9452		#
L_{ew}	60.1		mm
L_c	158.4		mm
S_{1c}	0.4418		mm^2
S_c	4.42		mm^2
$S_{c\,eq}$	4.42		mm^2
S_{Cu}	35.34		mm^2
S_{slot}	103.09		mm^2
k_{fill}	0.35		#
R_{ph} (@ 20 °C)	75.86		mΩ
J_s	14.11	28.22	$\mathrm{A\,mm}^{-2}$
$\widehat{K}_s$	80	160	$\mathrm{A\,mm}^{-1}$
Vol_{Cu}	257 300		mm^3
G_{Cu}	2.29		kg

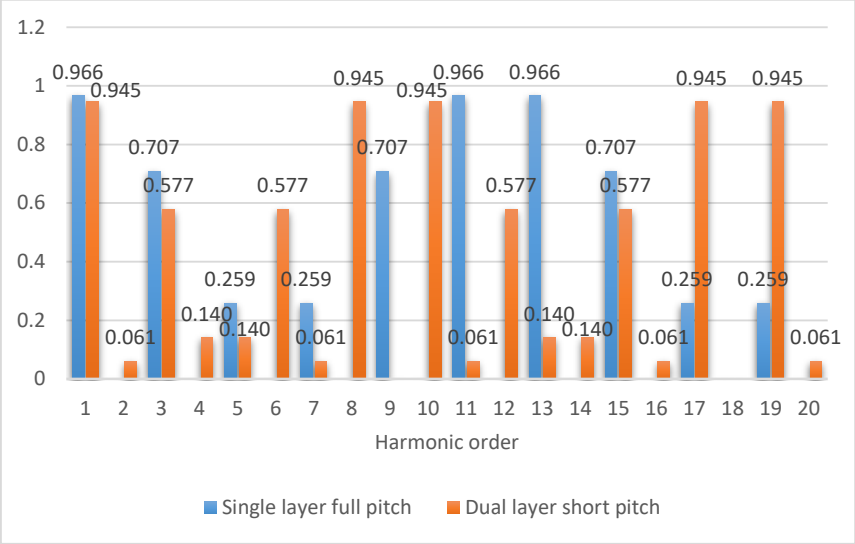

Figure 4.5: Computed winding factors for the two considered winding arrangements (fundamental and harmonics).

4.3 FE simulations results

As done in chapter 2, the overall motor performances are evaluated with FE simulations. Fig. 4.6 shows the saliency ratio map of the prototype. The simulated values are close to the ξ assumed in section 4.1, although slightly lower. The magnetic parameters of the prototype are reported in Figs. 4.7–4.9. In Fig. 4.8a, it can be noted that the d-axis flux linkage changes its sign for negative i_d values close to the nominal current (dashed red circle). It is an promising signal for the FW technique and the control trajectories in Fig. 4.11b confirm this. As shown by the dynamic curves (Fig. 4.11a) a moderate power drop occurs in overload conditions at the high speeds because, to reach the maximum speed with a so large current, the third FW region is needed.

The prototype meets the required performances and exhibits at the same time a rather low torque ripple (see Fig. 4.10). This machine has a PM torque

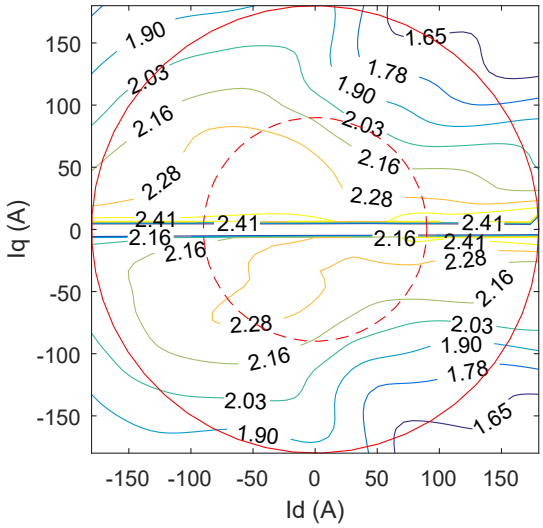

Figure 4.6: Prototype saliency ratio map. Circles represent the current limits (solid line for overload conditions and dashed line for nominal current).

component more pronounced than the reluctance one, in comparison to the Prius and LS 600h motors. The machine torque density probably benefits from this choice and nonetheless the overall amount of PM is not excessive.

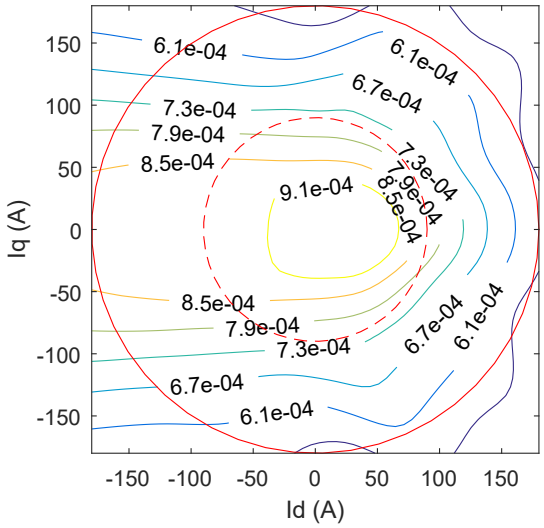

(a) L_d map.

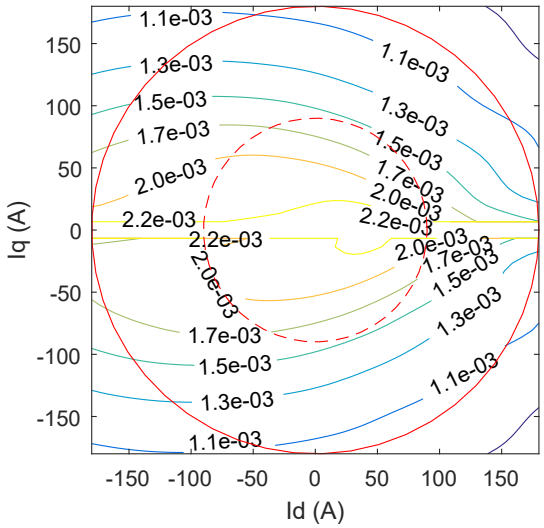

(b) L_q map.

Figure 4.7: Prototype dq-frame inductances. Circles represent the current limits (solid line for overload and dashed line for nominal conditions).

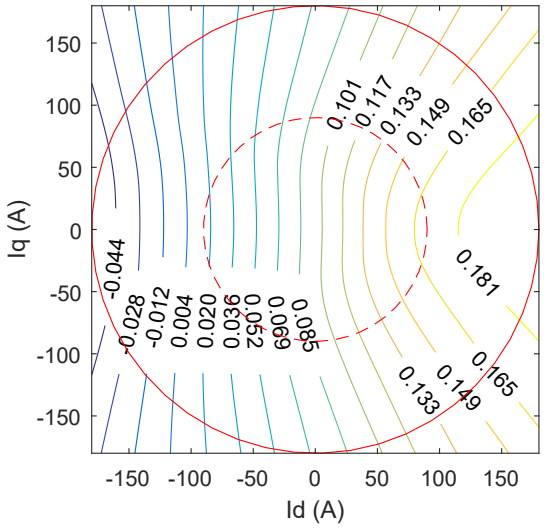

(a) Λ_d map.

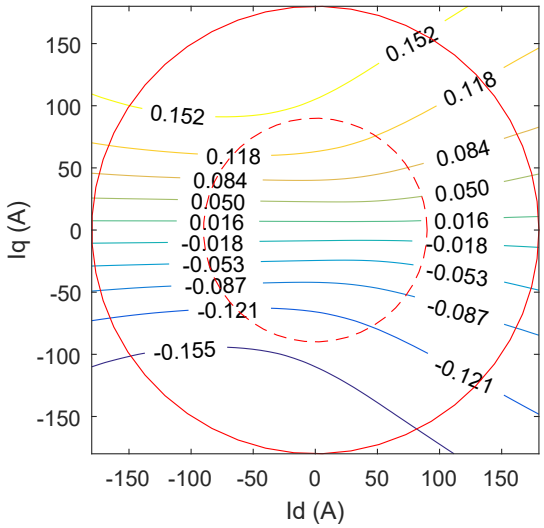

(b) Λ_q map.

Figure 4.8: Prototype *dq*-frame flux linkages. Circles represent the current limits (solid line for overload and dashed line for nominal conditions).

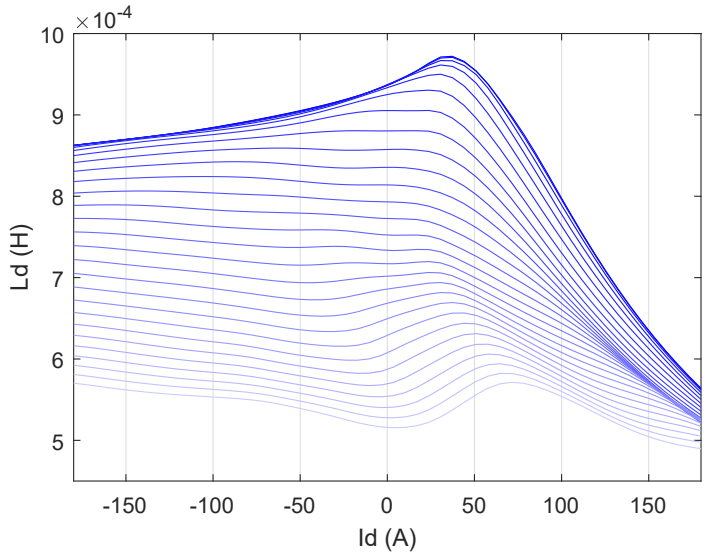

(a) L_d plot.

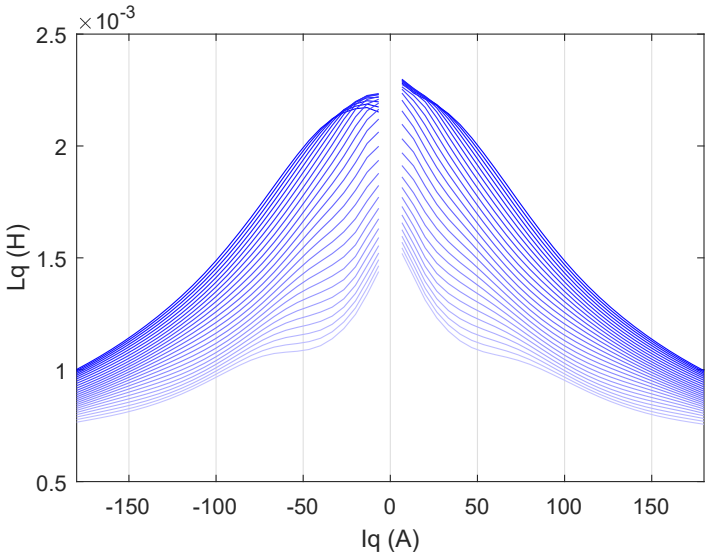

(b) L_q plot.

Figure 4.9: Prototype dq-frame inductances. Color gradient shows the current dependency from the dq current not in the x-axis.

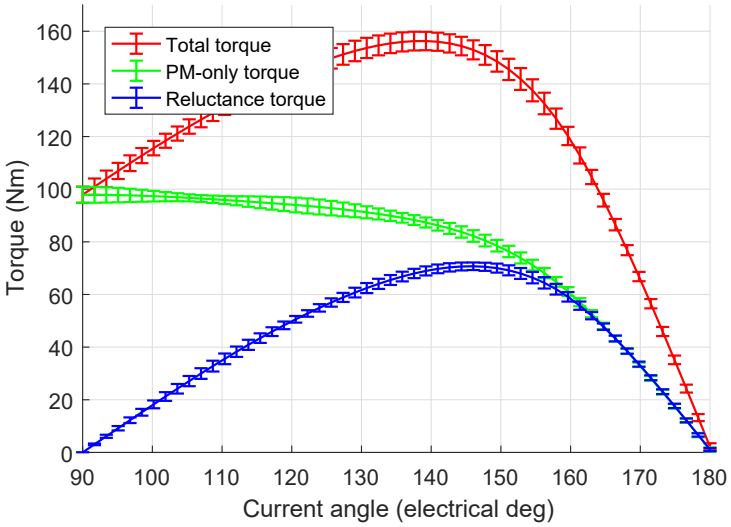

(a) Torque composition.

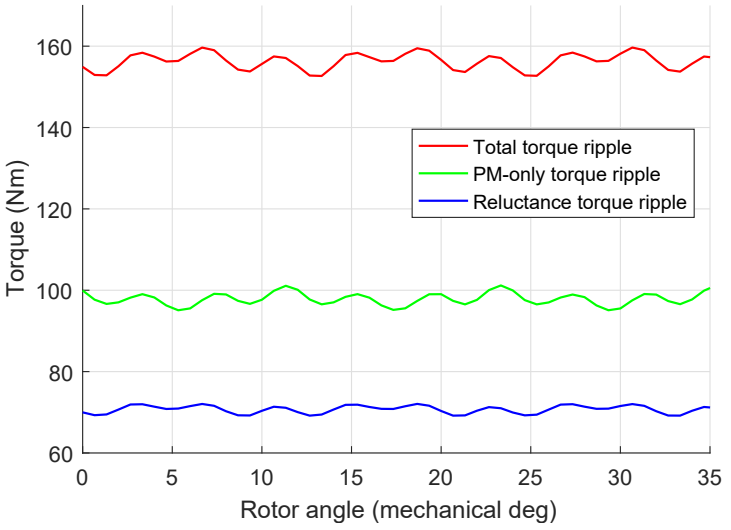

(b) Torque ripple.

Figure 4.10: Prototype torque analysis with overload current. (a) shows the torque composition. Vertical bars report the ripple. (b) illustrates torque ripple.

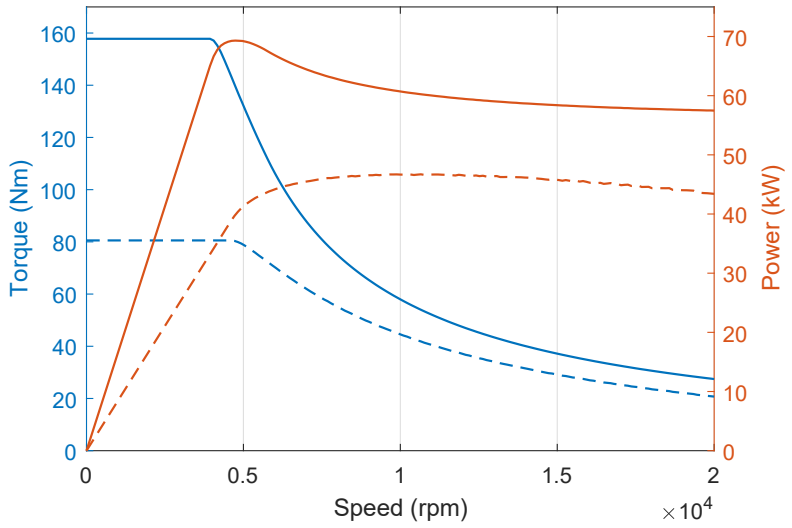

(a) Dynamic curves.

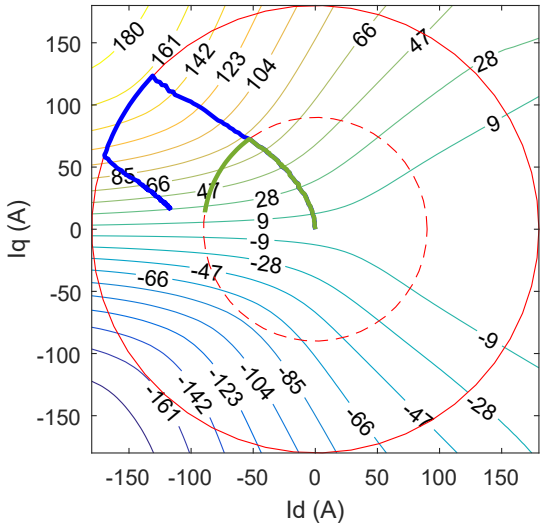

(b) Control trajectories.

Figure 4.11: Prototype max. torque and power vs. speed (a) with control trajectories (b). Solid and blue line for overload, dashed and green for nominal.

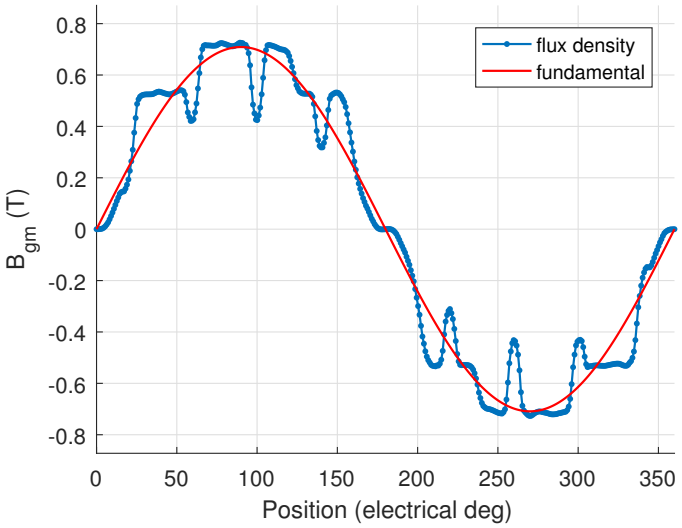

(a) Airgap flux density.

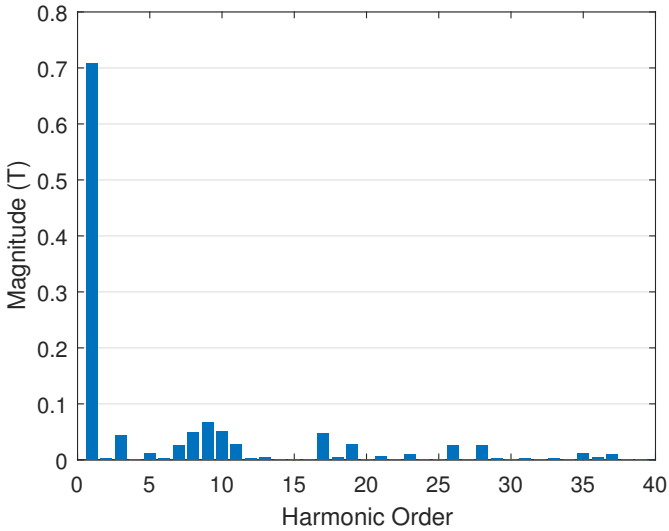

(b) B_{gm} FFT.

Figure 4.12: Prototype airgap flux density at no load condition (two poles).

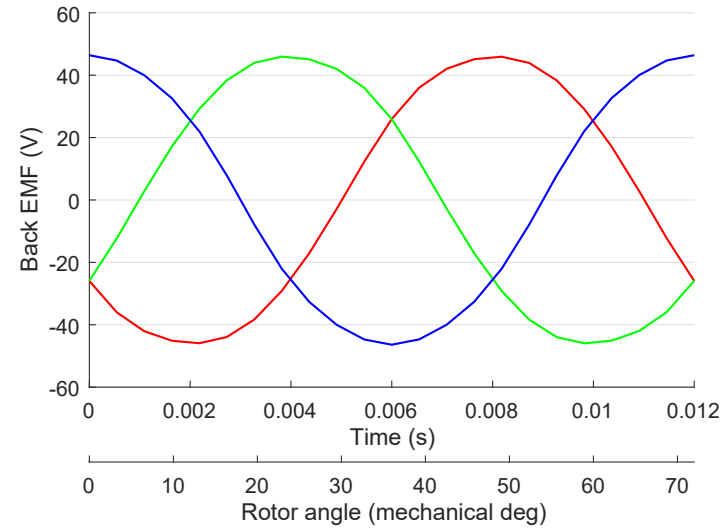

(a) Phase back EMF.

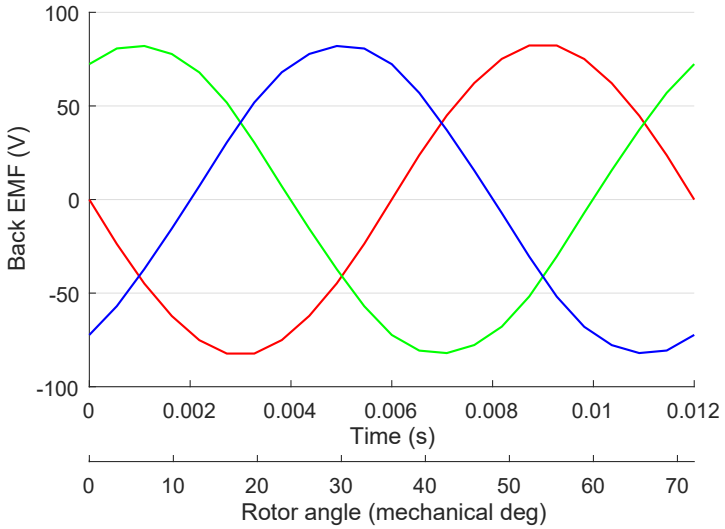

(b) Line back EMF.

Figure 4.13: Open circuit prototype back EMF at 1 000 rpm.

Finally, Fig. 4.14a shows the total losses of the prototype expressed in watts, while Fig. 4.14b depicts its efficiency map. The motor exhibits a high efficiency zone rather large. The iron losses are computed by means of the Steinmetz equation and considering an M250-35A lamination. The first six harmonics are taken into account. As Figs. 4.15 illustrate, the ohmic losses dominate the iron losses and in particular, the rotor iron losses are almost negligible compared to those in the stator. This is normal as it is a synchronous machine, however such low levels of the iron losses probably are due to the winding scheme and the low magnitude harmonics it produces.

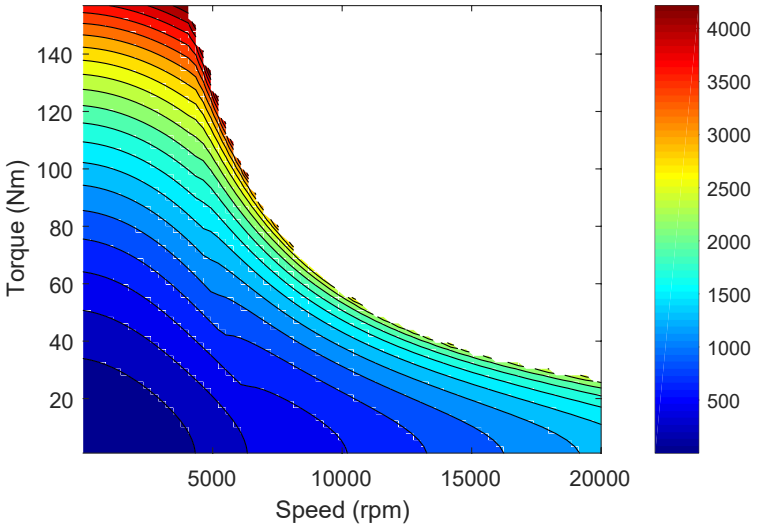

(a) Prototype total losses in watts.

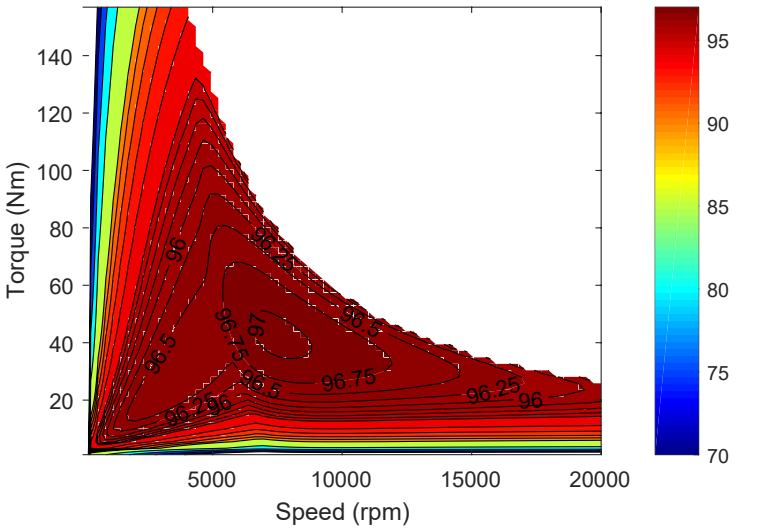

(b) Prototype efficiency.

Figure 4.14: Prototype total losses (a) and efficiency (b) maps.

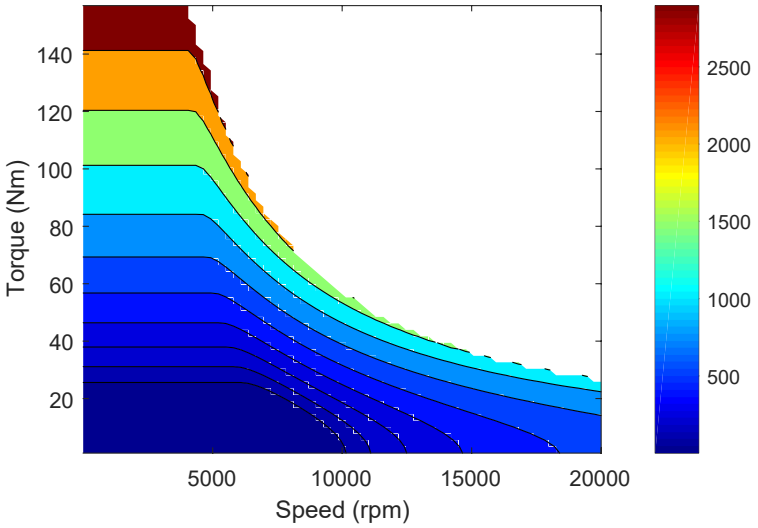

(a) Prototype ohmic losses in watts.

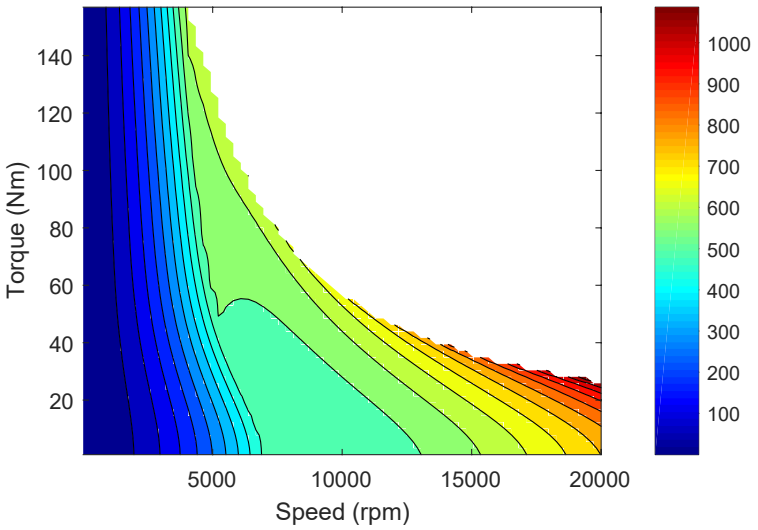

(b) Prototype iron (total) losses in watts.

Figure 4.15: Prototype ohmic (a) and iron (total) losses (b) maps.

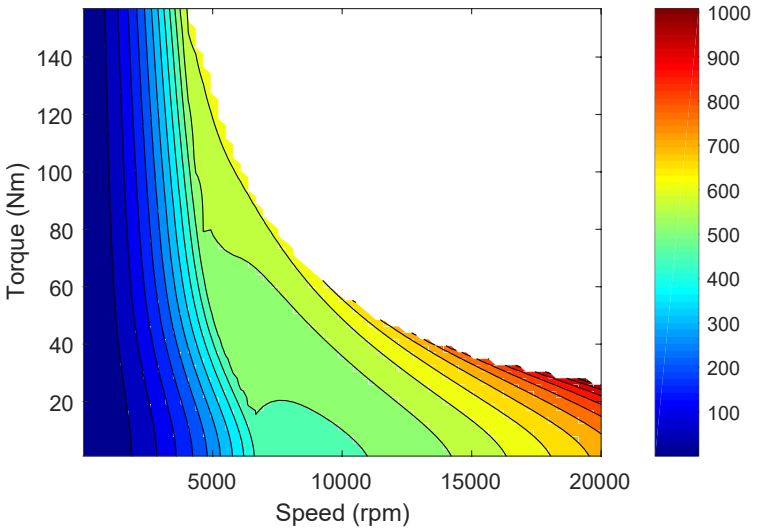

(a) Prototype stator iron losses in watts.

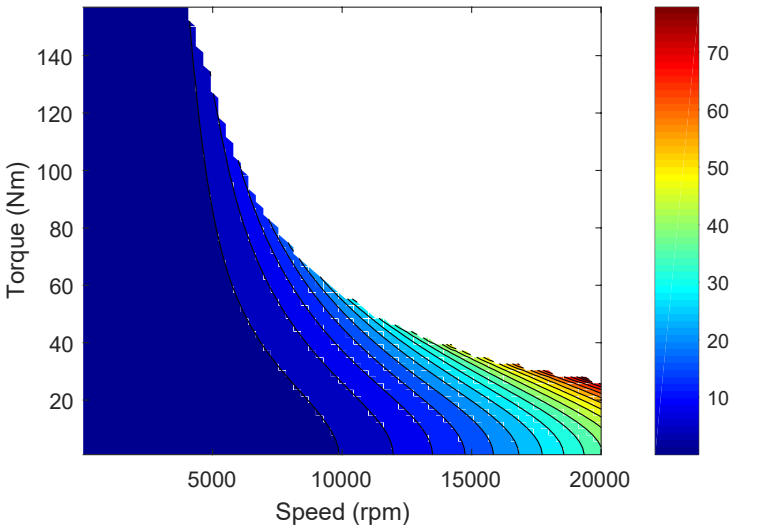

(b) Prototype rotor iron losses in watts.

Figure 4.16: Prototype iron losses in the stator (a) and rotor (b).

4.4 Thermal analysis

Thermal analysis has been performed by processing loss data through a lumped element thermal model in order to identify the proper insulation class, to assess the machine overload behavior and to size the water jacket.

As previously noted, the typical electric load of the traction automotive motors is very high. This means that heat dissipation issues can arise and so the thermal simulation analysis is very important. Although the thermal behavior of an electrical machine is rather complex as it involves both conductive and convective phenomena [38, 39], lumped parameters are usually an accurate method for the thermal analysis [40, 41, 42] since the motor geometric structure is quite regular.

4.4.1 Heat conduction in the motor core

The radial magnetization machines have a cylindrical shape, hence the most convenient way to express the Fourier heat law is in cylindrical coordinates.

$$q = -k \cdot \nabla T = -k\frac{\partial T}{\partial r}\,\vec{a_r} - \frac{k}{r}\frac{\partial T}{\partial \phi}\,\vec{a_\phi} - k\frac{\partial T}{\partial z}\,\vec{a_z} \tag{4.6}$$

where q stands for the heat flux, k is the thermal conductivity and $(\vec{a_r}, \vec{a_\phi}, \vec{a_z})$ represent the cylindrical coordinates unit vectors.

Now, the steady-state heat diffusion equation is:

$$\nabla \cdot q + q' = \frac{1}{r}\frac{\partial}{\partial r}\left(k\,r\,\frac{\partial T}{\partial r}\right) + \frac{1}{r}\frac{\partial}{\partial \phi}\left(\frac{k}{r}\frac{\partial T}{\partial \phi}\right) + \frac{\partial}{\partial z}\left(k\,\frac{\partial T}{\partial z}\right) + q' = 0 \tag{4.7}$$

where $q' = dq/dt$ corresponds to the "heat generation" term.

In addition, some thermal conductivities in the electric motors are very anisotropic and for this reason, Tab. 4.4 reports both axial and radial values for the iron lamination and stator winding. Usually, dielectric materials exhibit a low thermal conductivity. This explains such different axial and radial k_{lm} as well as k_{sw} [38, 43, 44, 45, 46].

Table 4.4: Main thermal conductivities in $\mathrm{W\,m^{-1}\,K^{-1}}$ and specific heat capacities in $\mathrm{J\,K^{-1}\,kg^{-1}}$ [38, 43, 44, 45, 46].

Material	**Symbol**	**Axial**	**Radial**	**Units**
Air	k_{air}	0.026		$\mathrm{W\,m^{-1}\,K^{-1}}$
Water	k_{H2O}	0.613		$\mathrm{W\,m^{-1}\,K^{-1}}$
Aluminium	k_{Al}	167		$\mathrm{W\,m^{-1}\,K^{-1}}$
Iron lamination	k_{lm}	1.7	21.9	$\mathrm{W\,m^{-1}\,K^{-1}}$
Stator winding	k_{sw}	292	0.99	$\mathrm{W\,m^{-1}\,K^{-1}}$
Slot insulation	k_{sli}	0.18		$\mathrm{W\,m^{-1}\,K^{-1}}$
PM (NdFeB)	k_{PM}	9		$\mathrm{W\,m^{-1}\,K^{-1}}$
Shaft	k_{sh}	51		$\mathrm{W\,m^{-1}\,K^{-1}}$
Water	c_{H2O}	4 179		$\mathrm{J\,K^{-1}\,kg^{-1}}$
Iron lamination	c_{lm}	447		$\mathrm{J\,K^{-1}\,kg^{-1}}$
Copper	c_{Cu}	385		$\mathrm{J\,K^{-1}\,kg^{-1}}$
Shaft steel	c_{sh}	446		$\mathrm{J\,K^{-1}\,kg^{-1}}$
PM (NdFeB)	c_{PM}	450		$\mathrm{J\,K^{-1}\,kg^{-1}}$

Equation 4.7 can be translated in an equivalent thermal network (Fig. 4.17), whose parameters can be found separating each component by means of proper assumptions about heat generation and boundary conditions. This network comprises three resistances arranged in a "T"-configuration on the right side of Fig. 4.17b, for the axial conduction, and three resistances on the left side, for the radial conduction [47, 48, 49]. The independent generator and the capacitance C_{cl} at the center correspond to the heat generation and storage effects.

Axial diffusion with zero internal heat generation $q' = 0$: In this case, (4.7) becomes:

$$\frac{\partial}{\partial z}\left(k_a \frac{\partial T}{\partial z}\right) = 0 \tag{4.8}$$

where k_a is the axial thermal conductivity.

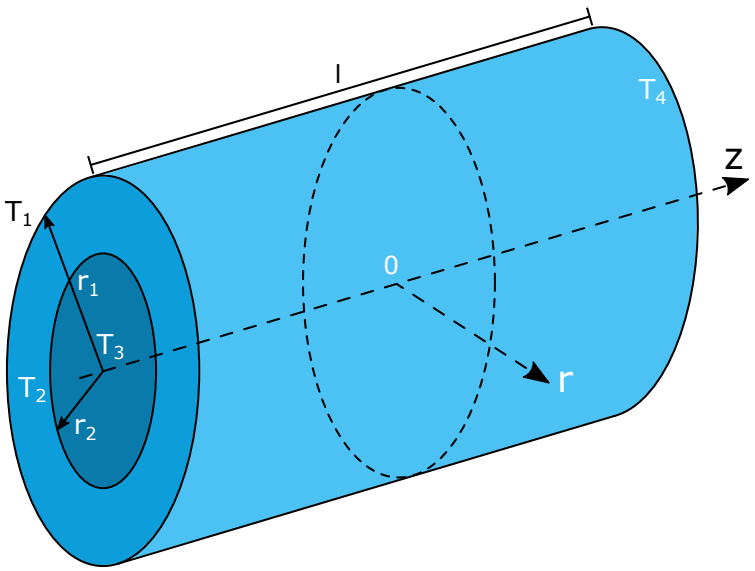

(a) Cylindrical geometric parameters.

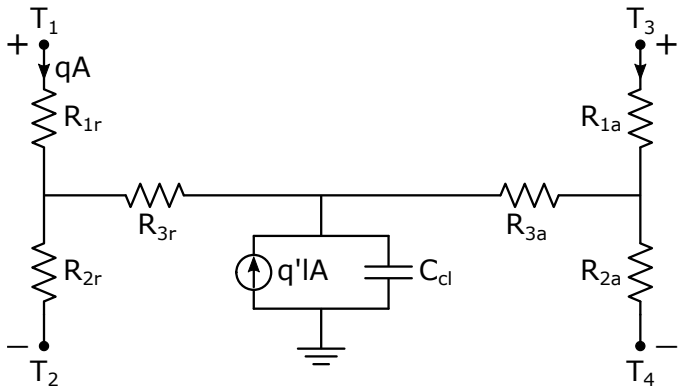

(b) Thermal network.

Figure 4.17: Equivalent thermal network for heat conduction in a cylindrical geometry [47, 48, 49].

Imposing the boundary conditions $T(-l/2) = T_3$ and $T(l/2) = T_4$, the solution of the differential equation (4.8) results:

$$T(z) = \frac{T_4 - T_3}{l} z + \frac{T_4 + T_3}{2} \tag{4.9}$$

l is the cylinder axial length.

From the following thermal resistance definition (4.10), the R_{1a} and R_{2a} expressions can be obtained.

$$qA = -k_a A \frac{dT}{dz} = \frac{k_a A}{l} \Delta T = \frac{1}{R_{1a} + R_{2a}} \Delta T \tag{4.10}$$

$$R_{1a} = R_{2a} = \frac{l}{2k_a A} \tag{4.11}$$

A is the cross-section surface corresponding to the z-axis.

Axial diffusion with zero surface temperatures $T(-l/2) = T(l/2) = 0$: This time, the heat generation term is taken into account.

$$\frac{\partial}{\partial z} \left(k_a \frac{\partial T}{\partial z} \right) + q' = 0 \tag{4.12}$$

Therefore, the temperature profile $T(z)$ results as follows.

$$T(z) = \frac{q' l^2}{2k_a} \left(\frac{1}{4} - \frac{z^2}{l^2} \right) \tag{4.13}$$

In order to apply the thermal resistance definition also in this case, the average temperature value $\overline{T}$ must be computed.

$$\overline{T} = \frac{1}{l} \int_{-l/2}^{+l/2} T(z) dz = \frac{q' l^2}{12 k_a S} \tag{4.14}$$

$$R_{3a} + R_{1a} || R_{2a} = \frac{\overline{T}}{q' l A} \tag{4.15}$$

Finally, substituting the cross-section surface expression $A = \pi(r_1^2 - r_2^2)$, the axial equivalent thermal resistances become:

$$R_{1a} = R_{2a} = \frac{l}{2\,k_a \pi (r_1^2 - r_2^2)} \tag{4.16}$$

$$R_{3a} = -\frac{l}{6\,k_a \pi (r_1^2 - r_2^2)} \tag{4.17}$$

R_{3a} is a negative auxiliary term, not a physical resistance.

Radial diffusion with zero internal heat generation $q' = 0$: In this case, (4.7) can be simplified in the following way:

$$\frac{1}{r}\frac{\partial}{\partial r}\left(k_r\, r\, \frac{\partial T}{\partial r}\right) = 0 \tag{4.18}$$

Again, the solution of (4.18) compatible with the boundary conditions $T(r_1) = T_1$ and $T(r_2) = T_2$ is:

$$T(r) = \frac{T_2 - T_1}{\ln\left(\dfrac{r_2}{r_1}\right)} \ln\left(\frac{r}{r_1}\right) + T_1 \tag{4.19}$$

$$\frac{dT}{dr} = \frac{T_2 - T_1}{r \cdot \ln\left(\dfrac{r_2}{r_1}\right)} \tag{4.20}$$

Following the same procedure as for (4.10) but using $A = 2\pi\, r\, l$ and the temperature derivative (4.20) along the radial coordinate r, the total equivalent resistance is found.

$$R_{1r} + R_{2r} = \frac{\ln\left(\dfrac{r_1}{r_2}\right)}{2\pi\, k_r\, l} \tag{4.21}$$

In order to split (4.21) in the R_{1r} and R_{2r} values, the average temperature $\overline{T}$ has to be computed.

$$\overline{T} = \frac{2}{r_2^2 - r_1^2} \int_{r_1}^{r_2} T(r) \cdot r\, dr = \frac{T_2\, r_2^2 - T_1\, r_1^2}{r_2^2 - r_1^2} - \frac{T_2 - T_1}{2 \ln\left(\dfrac{r_2}{r_1}\right)} \tag{4.22}$$

$$qA = \frac{T_1 - \overline{T}}{R_{1r}} \tag{4.23}$$

Then the thermal equivalent resistance definition (4.23) and (4.21) yield the final R_{1r} and R_{2r} expressions.

$$R_{1r} = \frac{1}{4\pi\, k_r\, l}\left[1 - \frac{2\, r_2^2 \ln(r_1/r_2)}{r_1^2 - r_2^2}\right] \tag{4.24}$$

$$R_{2r} = \frac{1}{4\pi\, k_r\, l}\left[\frac{2\, r_1^2 \ln(r_1/r_2)}{r_1^2 - r_2^2} - 1\right] \tag{4.25}$$

Radial diffusion with zero surface temperatures $T(r_1) = T(r_2) = 0$: As with (4.12), the heat generation term q' changes the $T(r)$ function.

$$\frac{1}{r}\frac{\partial}{\partial r}\left(k_r\, r\, \frac{\partial T}{\partial r}\right) + q' = 0 \tag{4.26}$$

$$T(r) = \frac{q'}{4\, k_r}\left[\frac{r_2^2 - r_1^2}{\ln(r_2/r_1)} \ln\left(\frac{r}{r_1}\right) - (r^2 - r_1^2)\right] \tag{4.27}$$

Then, from (4.27) the average T value becomes:

$$\overline{T} = \frac{2}{r_2^2 - r_1^2}\int_{r_1}^{r_2} T(r)\cdot r\, dr = \frac{q'}{8\, k_r}\left\{r_2^2 + r_1^2 - \frac{r_2^2 - r_1^2}{\ln(r_2/r_1)}\right\} \tag{4.28}$$

Now, all the elements necessary to find R_{3r} are known.

$$R_{3r} + R_{1r}||R_{2r} = \frac{\overline{T}}{-q'\, l\, A} = \frac{\overline{T}}{-q'\pi(r_2^2 - r_1^2)l} = \frac{r_1^2 + r_2^2 - \dfrac{r_1^2 - r_2^2}{\ln(r_1/r_2)}}{8\, k_r \pi (r_1^2 - r_2^2) l} \tag{4.29}$$

$$R_{3r} = \frac{-1}{8\pi k_r (r_1^2 - r_2^2) l}\left[r_1^2 + r_2^2 - \frac{4\, r_1^2\, r_2^2 \ln(r_1/r_2)}{r_1^2 - r_2^2}\right] \tag{4.30}$$

Fig. 4.17b network is used for many concentric areas within the machine: the stator back-iron, the teeth, the rotor "surface" region (where the PMs are

placed), the rotor yoke and the shaft. For each of these motor parts, different radii r_1, r_2 and conductivities k_a, k_r have to be selected properly. The only parameter which does not change for the whole machine normally is the cylinder axial length set to the machine stack length $l = L_{stk}$.

4.4.2 Heat conduction in the winding

Together with teeth, the stator winding forms a sort of "interdigitated structure", hence its equivalent thermal network can be calculated similarly to a circular comb heat exchanger [38, 40]. The first step consists in defining a conventional axial thermal resistance R_{thA} and radial thermal resistance R_{thR}.

$$R_{thA} = \frac{l}{N\, S_{slot}\, k_{swA}} \tag{4.31}$$

where N is the number of "fins" (here the number of slots, $N = Q_s$), S_{slot} is the slot cross-section surface and k_{swA} is the winding axial conductivity.

$$R_{thR} = \frac{1}{l\, N}\left(\frac{1}{4\pi k_{swR}} + \frac{t_i}{P_{ss}\, k_{sli}} + \frac{1}{P_{ss}\, h_c}\right) \tag{4.32}$$

The radial thermal resistance R_{thR} consists of three components: the first is related to the heat conduction within the slot (k_{swR} is the winding radial conductivity), the second refers to the heat conduction through the slot insulation (P_{ss} is the slot perimeter, t_i is the insulation thickness and k_{sli} is the insulation material conductivity) while the third is the contact resistance (h_c stands for the contact heat transfer coefficient). A radial conductance can be also defined: $G_{thR} = 1/R_{thR}$.

Because of the strongly asymmetric shape of the winding, (4.31) is not accurate since neglects the combined effect of the axial and radial heat conduction. Therefore, following an analytic procedure like that in the previous subsection and making some approximations, (4.31) can be replaced by three resistances in "T"-configuration: R_{1a}, R_{2a} and R_{3a}.

$$R_{1a} = R_{2a} \simeq \sqrt{\frac{R_{thA}}{G_{thR}}} \tanh\left(\frac{\sqrt{R_{thA}\, G_{thR}}}{2}\right) \tag{4.33}$$

$$R_{3a} \simeq \frac{1}{G_{thR}} \left[\frac{\sqrt{R_{thA}\, G_{thR}}}{\sinh(\sqrt{R_{thA}\, G_{thR}}/2)} - 1\right] \tag{4.34}$$

4.4.3 Airgap convection

Among the several convective contributions, the most important is that related to the airgap, as it is the only thermal resistance which connects the rotor with the stator. The heat transfer characteristics vary with the rotor speed [50]. When the rotation speed is particularly low, the natural convection is preponderant. As the rotor speed rises, also the Taylor number increases and the flow (called *Couette flow*) becomes steady and laminar. Then, once the *critical speed* is exceeded, the flow becomes very turbulent and the so-called *Taylor vortices* take place [51].

The airgap heat-transfer coefficient h_g is function of the Nusselt number Nu_g.

$$h_g = k_{air} \cdot \frac{Nu_g}{2g} \tag{4.35}$$

Because of the different flow conditions, the *Nusselt number* is expressed by a piecewise function.

$$Nu_g = \begin{cases} 2 & Ta_g < 1\,994 \\ 0.128\, Ta_g^{0.367} & 1\,994 \leq Ta_g < 1 \times 10^4 \\ 0.409\, Ta_g^{0.241} & 1 \times 10^4 \leq Ta_g \end{cases} \tag{4.36}$$

Obviously, the *Taylor number* Ta_g depends on the rotor speed ω.

$$Ta_g = \omega^2 \frac{D_r}{2} \frac{g^3}{\nu_{air}^2} \tag{4.37}$$

where ν_{air} is the kinematic viscosity of air.

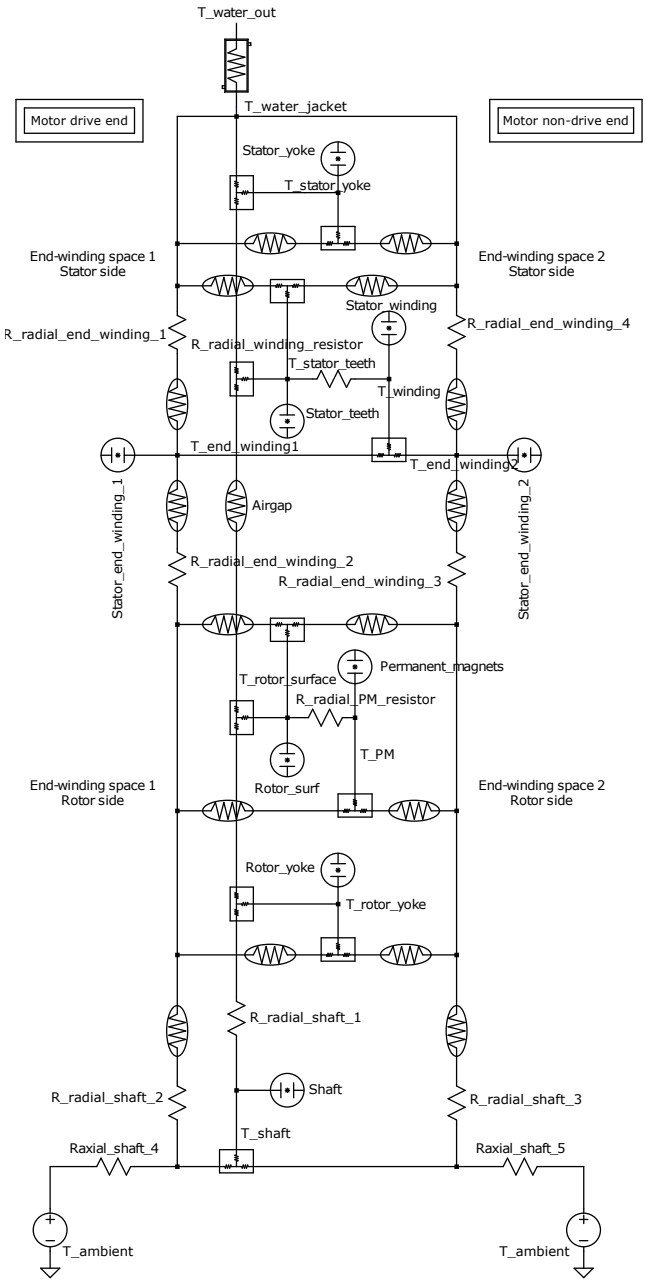

Figure 4.18: Overall motor thermal network.

Table 4.5: Steady-state motor temperatures in nominal operating conditions.

Machine part	**Temperature (°C)**
Winding	143
Stator teeth	78
Stator yoke	49
Rotor surface	79
Rotor yoke	77
PMs	79
Shaft	75

Figure 4.18 depicts the overall motor thermal network. It can be observed that the radial dimension is represented vertically whereas the axial dimension horizontally. In particular, each rectangular box contains three "T"-arranged resistances (see previous subsections), the circular elements incorporate the heat generator and capacitance of Fig. 4.17b, while the oval elements are for the convective equivalent resistors. The first rectangular element on the top of the schematic is the water jacket equivalent thermal resistance.

Both the convective resistances (except for the airgap) and the water jacket are modeled as described in [38, 39] and [52, 53].

In conclusion, Tab. 4.5 and 4.6 report the prototype temperatures in steady-state conditions and the water jacket parameters, respectively. The operating point which has been selected is the worst (highest losses) with the nominal current: the maximum torque (about 80 N m) and base speed. As can be noted, the machine needs at least a *class F* insulation but the *class H* should be preferable. For the water jacket, aluminium case has been assumed.

Finally, Fig. 4.19 shows the overload capabilities of the machine for 30 s. It is a rather long timespan for the traction application, and the simulation results are very encouraging.

The winding and stator teeth temperatures dominate the others which seem also less variable.

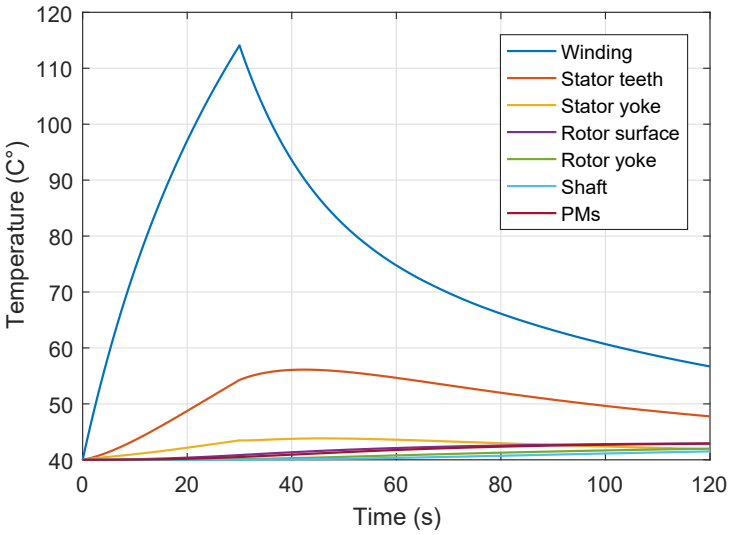

(a) Max torque and base speed operating conditions.

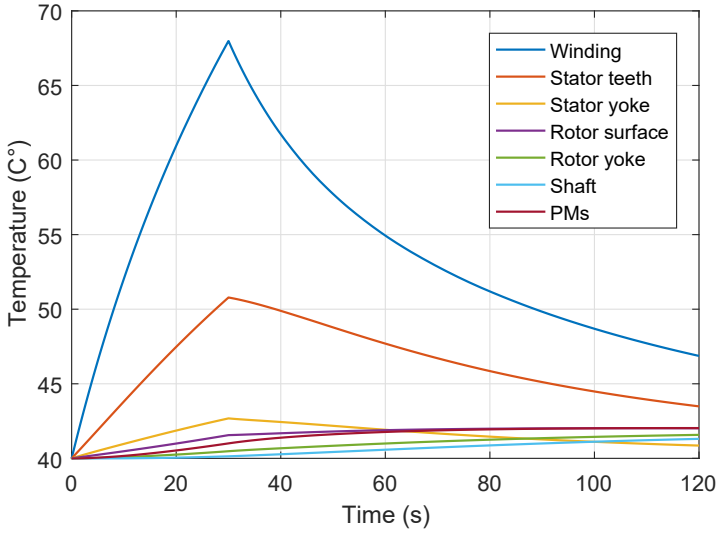

(b) Max speed operating conditions.

Figure 4.19: Prototype 30 s overload thermal simulations.

Table 4.6: Water jacket parameters.

Parameter	Symbol	Value	Units
Water flow rate	-	15	L/min
Tube diameter	d_{tube}	10	mm
Tube turns number	n_{tube}	6	#
Tube walls thickness	t_{tube}	3	mm

4.5 Mechanical design

The IPM machines rotor topology requires dedicated structures, called iron bridges or ribs, in order to guarantee the rotor mechanical integrity. The iron bridges design is a critical task, since they are responsible for PM flux leakage (see Tab. 2.6) and rotor magnetic anisotropy deterioration, despite their mechanical key role. Thicker iron ribs have higher mechanical strength but loose more magnetic flux, along with torque, whereas thinner ribs saturate more deeply, giving better magnetic performances, but they could be too weak. Therefore, the iron bridges dimensions are inherently subject to a design tradeoff. The automotive traction applications are a very challenging context for these kind of issues, as EV electric motors typically exhibit high torque ratings, especially with the overload current, and can achieve a speed of more than 10 000 rpm. Consequently, the iron bridges in an IPM motor for EVs must withstand very large centrifugal and electromagnetic forces at the same time. In addition, reliability in automotive is of primary concern and the average car customer is rather demanding about this matter.

Most professional CAD softwares for the IPM motor design integrate finite elements (FE) structural analysis modules to manage the stresses and strains of the rotor geometry. The standard approach consists in sizing the iron bridges so that the highest computed von Mises stress in the iron ribs is lower than the lamination yield strength (or, more rarely, the ultimate strength). Sometimes the maximum acceptable stress value can be set also with an empirical safety

coefficient. Up to 25 % of the PM flux is used for the iron ribs saturation in an IPM machine, thus leading to a significant PM under-utilization. Improving the effectiveness and accuracy of the mechanical design could therefore enable remarkable cost savings without affecting the performances, by means of PM volume reduction or replacing rare-earth PM with ferrites.

Many studies in literature about mechanical integrity of IPM rotors, neglect magnetic force, giving attention only to the centrifugal force [54], or make simplifying assumptions such as constant magnetic force independently from the operating condition [55].

Table 4.7: Operating points studied.

Prius		**LS 600h**		**Prototype**	
Speed (rpm)	*Torque* (N m)	*Speed* (rpm)	*Torque* (N m)	*Speed* (rpm)	*Torque* (N m)
3 320	205.1	5 310	303.4	4 020	159.7
13 500	44.53	10 230	170.9	20 000	27.3

In this section, a detailed FE study of the mechanical stress propagation in the iron bridges of the Toyota Prius, Lexus LS 600h and the new prototype IPM motors is carried out considering both the electromagnetic and the centrifugal forces. The analysis compares the resulting stresses in two operating points (see Tab. 4.7) for each motor:

- maximum overload torque at base speed,
- maximum overload power at top speed (with flux weakening).

The rotation angular direction is illustrated by the circular dashed curve in Fig. 4.20 and the rotor circumference coordinates system has the same direction but is located at the rotor outer radius. The rotor iron bridges are highlighted with color gradients.

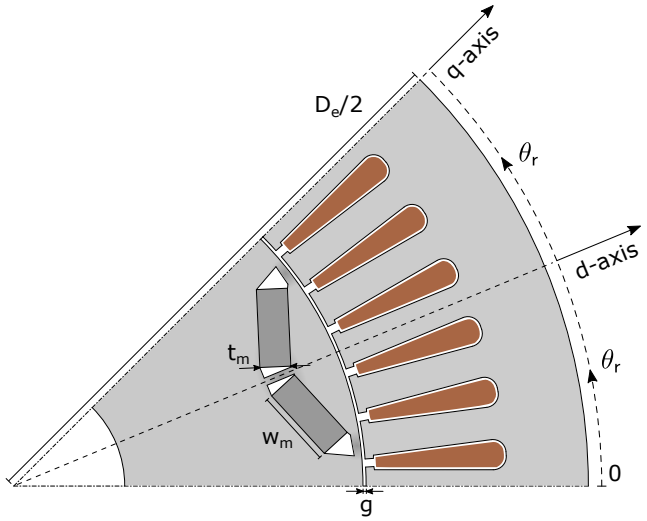

(a) Prius.

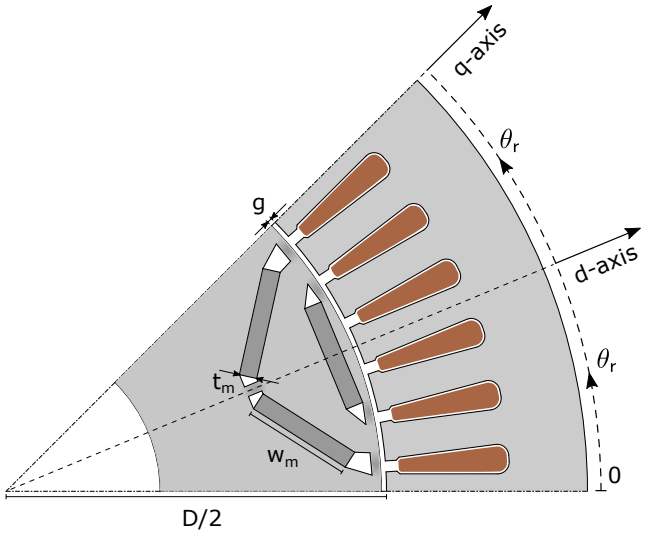

(b) LS 600h.

Figure 4.20: Angle and rotation direction convention.

4.5.1 Magnetic force computation

Magnetic stresses acting on the rotor have been computed by means of the Maxwell's stress tensor, which is a consolidated technique [56, 57, 58, 59, 60]. According to Maxwell's stress theory, the magnetic field strength between objects creates a stress σ_F on the object surfaces. The stress occurs in the direction of flux lines and can be divided into its radial σ_{Fr} and tangential σ_{Ft} components [15].

$$\sigma_{Fr} = \frac{1}{2}\,\mu_0\left(H_r^2 - H_t^2\right) \tag{4.38}$$

$$\sigma_{Ft} = \mu_0\,H_r\,H_t \tag{4.39}$$

Equation (4.38) and (4.39) need the magnetic field radial H_r and tangential H_t components in the airgap, while $\mu_0 = 4\,\pi \cdot 10^{-7}$ H/m is the magnetic permeability of free space. Therefore, the rotor magnetic stresses are computed post-processing magnetic FEA results. In this study, the open-source tool *Finite Element Method Magnetics* (FEMM) [29] was used.

The dynamic curves in Fig. 4.21a and 4.21b come from the maximum torque per ampere (MTPA) and flux weakening (FW) control techniques in overload conditions. Two notable operating points (highlighted with the blue diamond markers) are considered: the first one, represents the maximum speed point achievable in the maximum torque speed range, so it combines a high centrifugal force together with the maximum magnetic one; the second point explores the constant power speed range (CPSR) of the dynamic curves, giving more importance to the centrifugal component than to the magnetic one, so the top speed is selected along with the related torque that results from FW.

Figs. 4.22–4.24 show the magnetic stress distributions σ_{Fr} and σ_{Ft} on the rotor surface of the Prius, LS 600h and prototype motors. Figs. 4.22a–4.23b illustrate the magnetic stresses computed for one pole, as the flux density repeats periodically for those two motors on a single-pole basis. On the contrary, since the prototype motor winding scheme is dual-layer fractional pitch, the minimum the machine portion that repeats is two poles (see Fig. 4.24). The data refer to *d*-axis aligned rotors. In figs. 4.22a–4.23b some dashed vertical

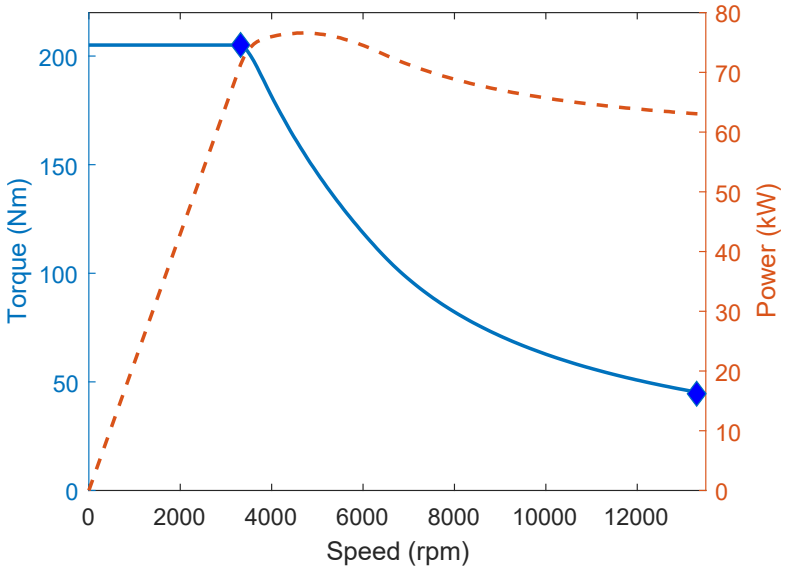

(a) Prius.

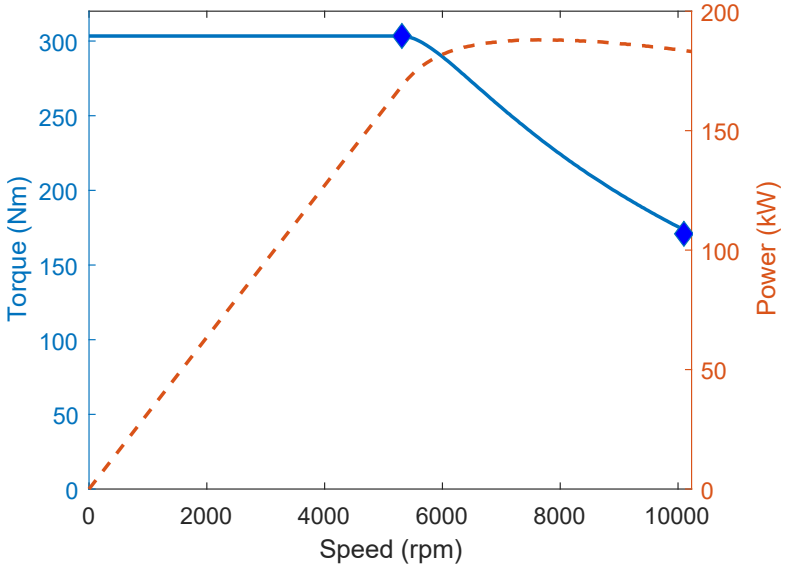

(b) LS 600h.

Figure 4.21: Dynamic curves. In (a) and (b) the solid line is torque, while the dashed line is power.

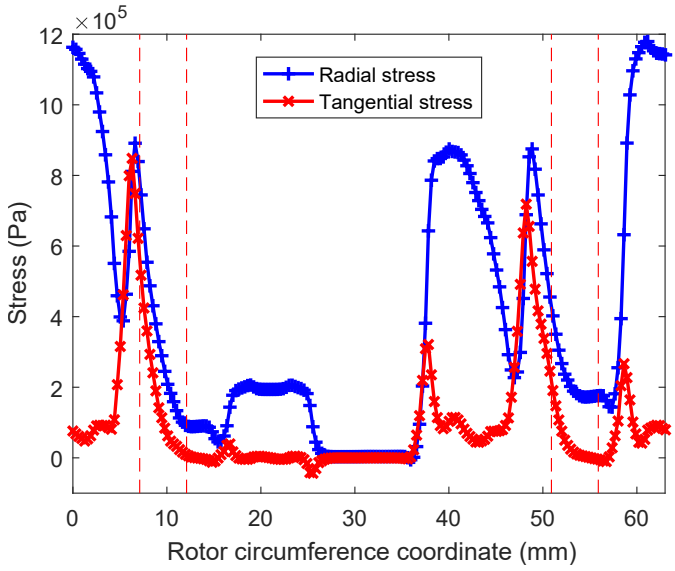

(a) Prius.

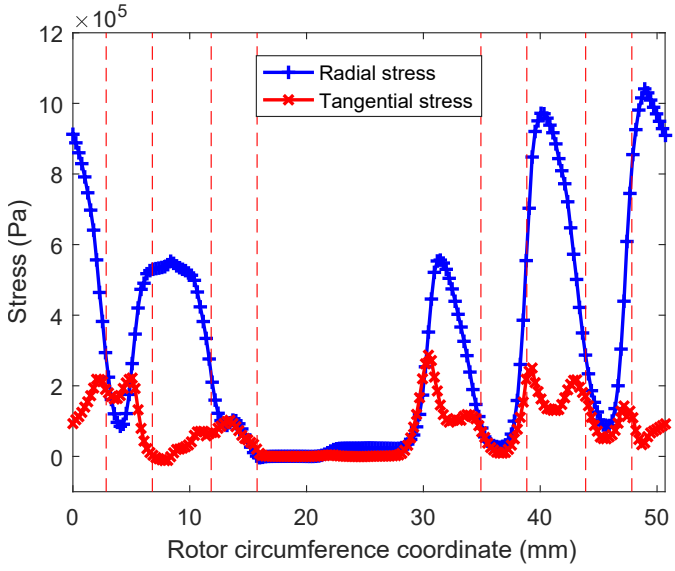

(b) LS 600h.

Figure 4.22: Magnetic stresses for the high-torque operating point. One-pole data are shown.

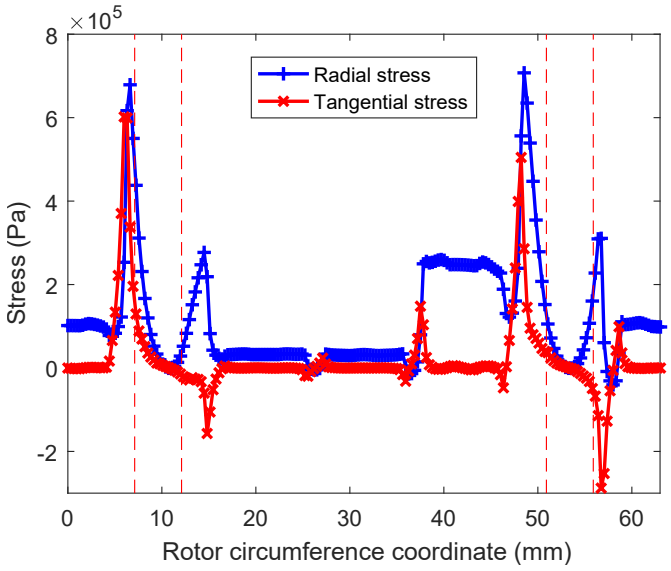

(a) Prius.

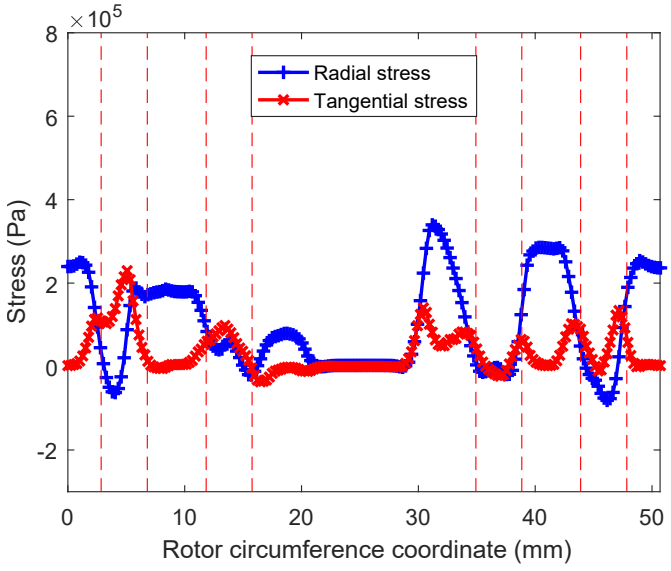

(b) LS 600h.

Figure 4.23: Magnetic stresses for the high-speed operating point. One-pole data are shown.

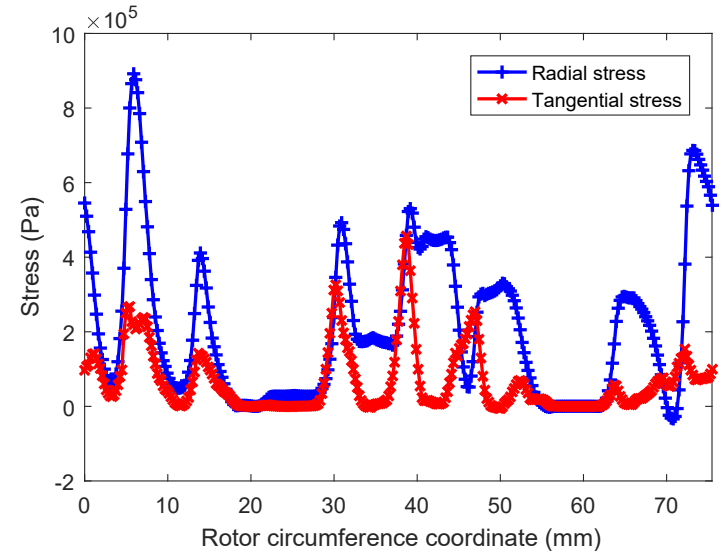

(a) High-torque operating point.

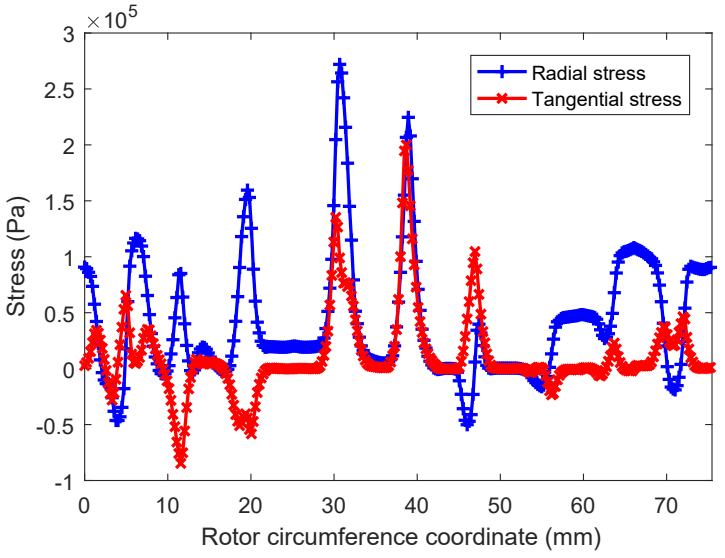

(b) High-speed operating point.

Figure 4.24: Magnetic stresses for the prototype motor. Two-poles data are shown.

red lines have been added for reference to pinpoint the rotor outer ribs as the most directly exposed to the magnetic stresses. Since the electromagnetic and the geometrical alignment are different in the prototype, the outer ribs position has not been reported in its figures because it could be confusing.

In all the operating conditions, the radial stress is much higher than the tangential one. In most cases, the magnetic stress peaks are not located exactly on the center of the iron bridges but rather high stress values (hundreds of kPa) can be observed at the boundary dashed lines. In addition, σ_{Fr} and σ_{Ft} distributions change with the rotor position (Figs. 4.25–4.30), then even higher stress values may cross the ribs boundary lines. This is due to the interaction between the rotor PMs and stator slots relative position. Each of the plots in Figs. 4.25–4.28 show 11 radial and tangential stress curves sweeping the rotor position in steps of $360°/(2p \cdot 11)$, while in Figs. 4.29–4.30 the rotor steps are of $360°/(p \cdot 11)$.

Looking at the stresses of the top speed operating points in Figs. 4.23a–4.23b, 4.24b, 4.26a–4.26b, 4.28a–4.28b, 4.29b and 4.30b it can be observed that peak and average values decrease as expected, due to the FW. However the peak stresses do not drop all in equal measure, thus changing the distribution profile. The magnetic stress order of magnitude still equals to hundreds of kPa and must be added to the maximum centrifugal stress.

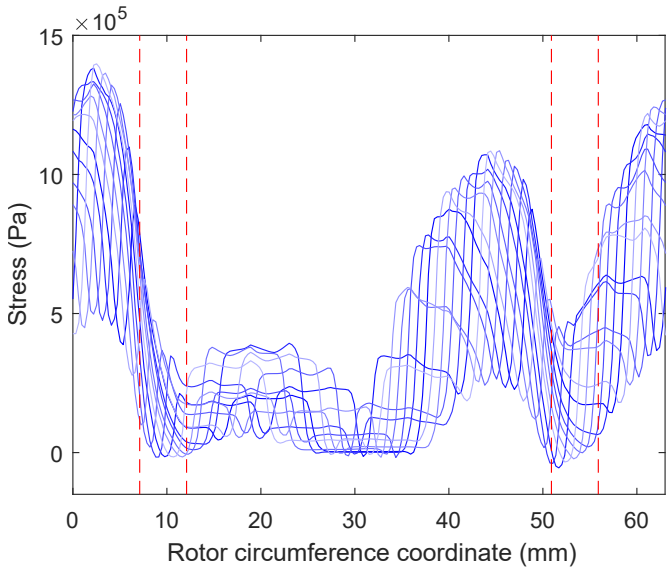

(a) Prius.

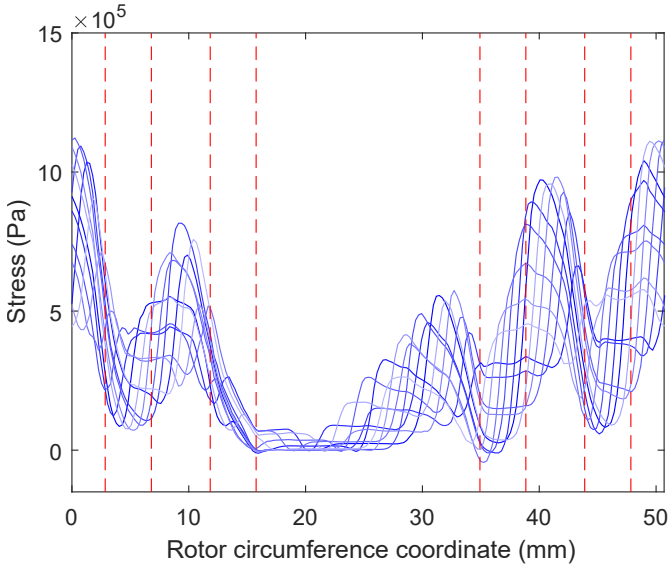

(b) LS 600h.

Figure 4.25: Radial magnetic stresses in high-torque conditions and sweeping the rotor position. The vertical lines mark the rotor outer ribs boundaries.

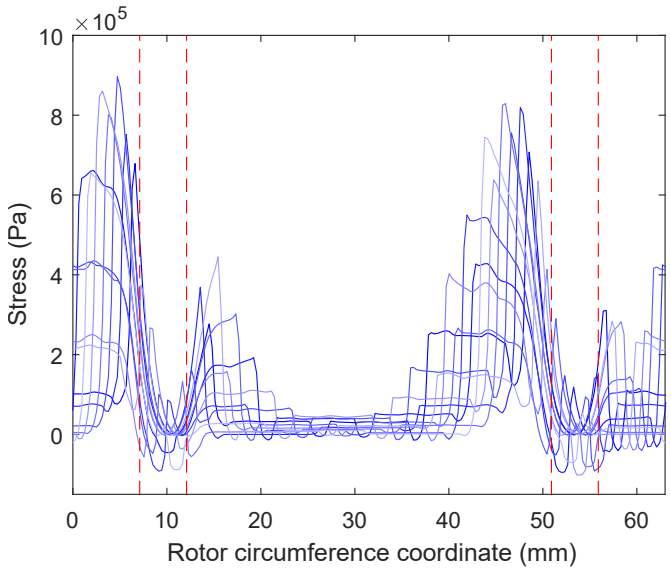

(a) Prius.

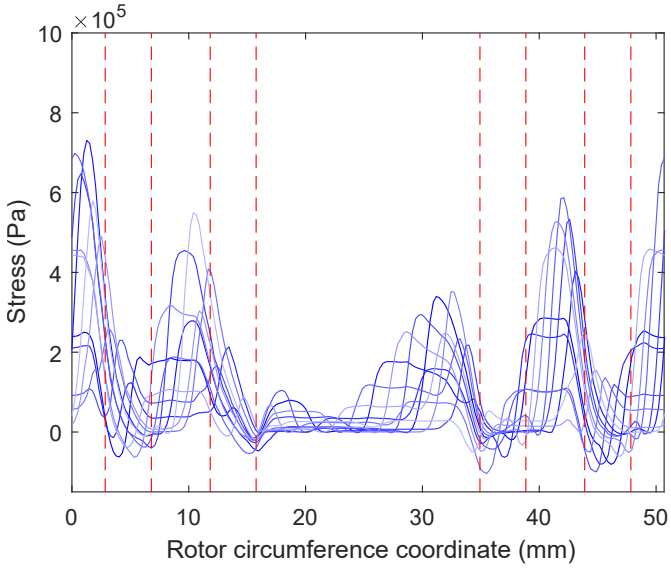

(b) LS 600h.

Figure 4.26: Radial magnetic stresses in high-speed conditions and sweeping the rotor position. The vertical lines mark the rotor outer ribs boundaries.

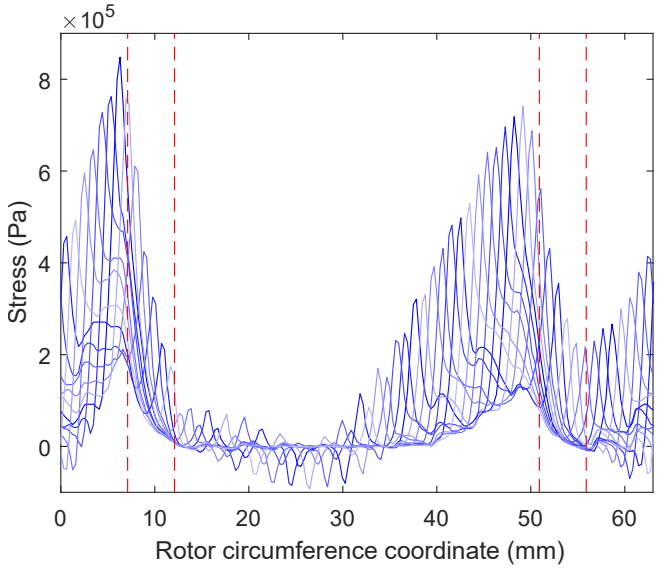

(a) Prius.

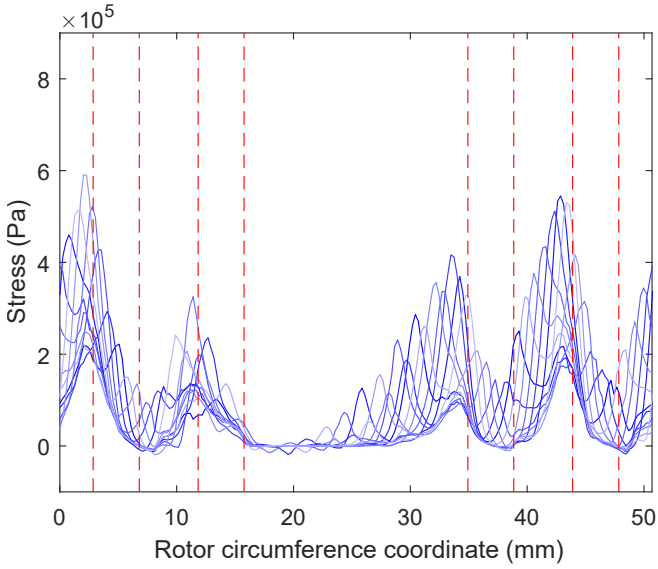

(b) LS 600h.

Figure 4.27: Tangential magnetic stresses in high-torque conditions and sweeping the rotor position. The vertical lines mark the rotor outer ribs boundaries.

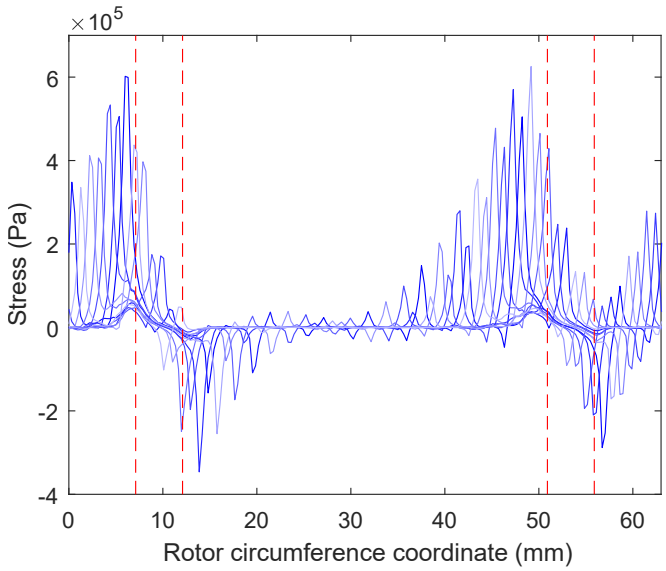

(a) Prius.

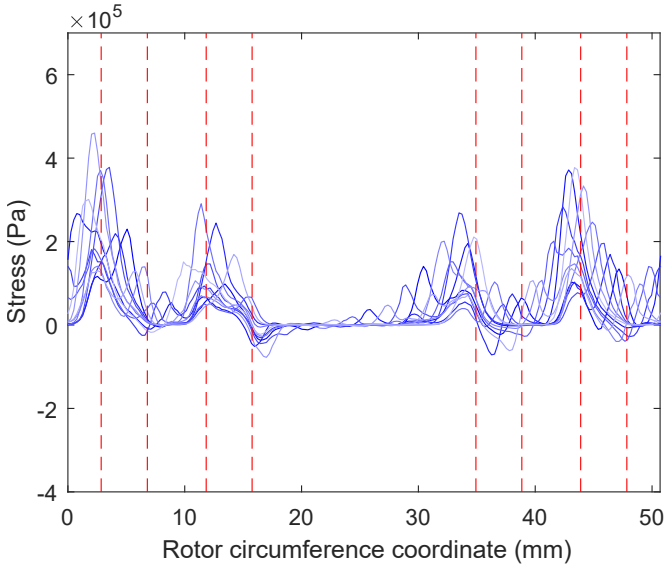

(b) LS 600h.

Figure 4.28: Tangential magnetic stresses in high-speed conditions and sweeping the rotor position. The vertical lines mark the rotor outer ribs boundaries.

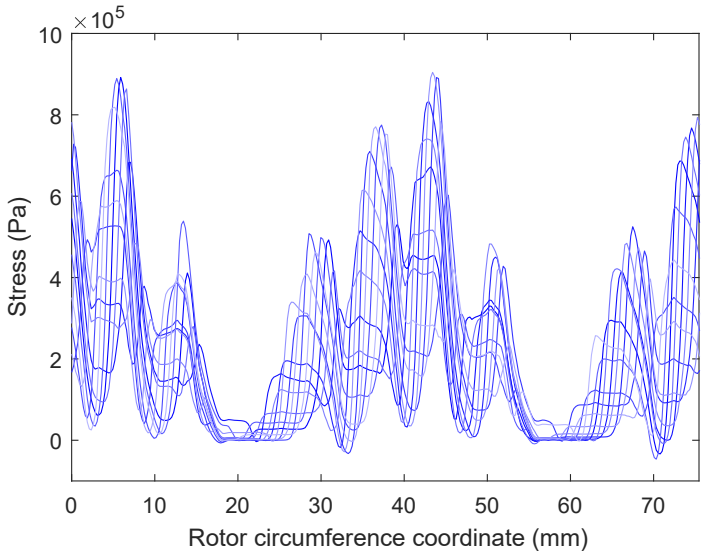

(a) High-torque operating point.

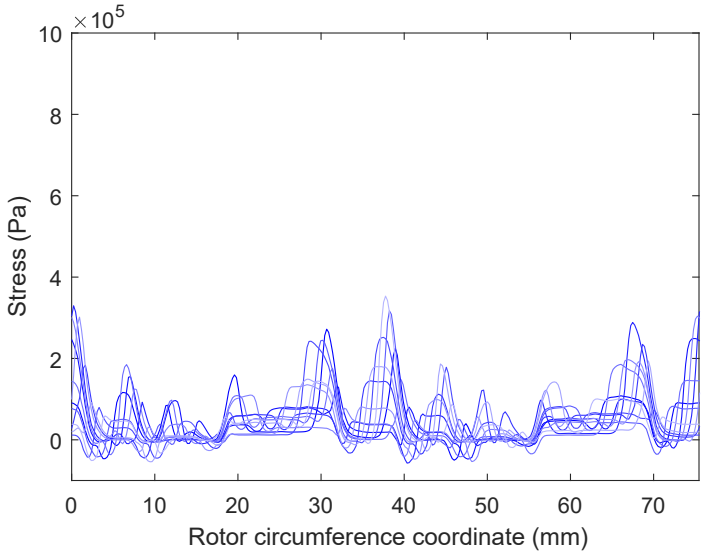

(b) High-speed operating point.

Figure 4.29: Radial magnetic stresses of the prototype sweeping the rotor position.

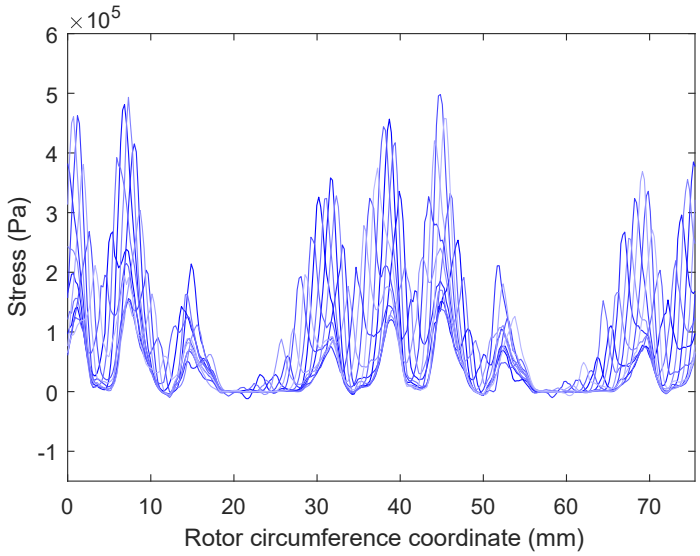

(a) High-torque operating point.

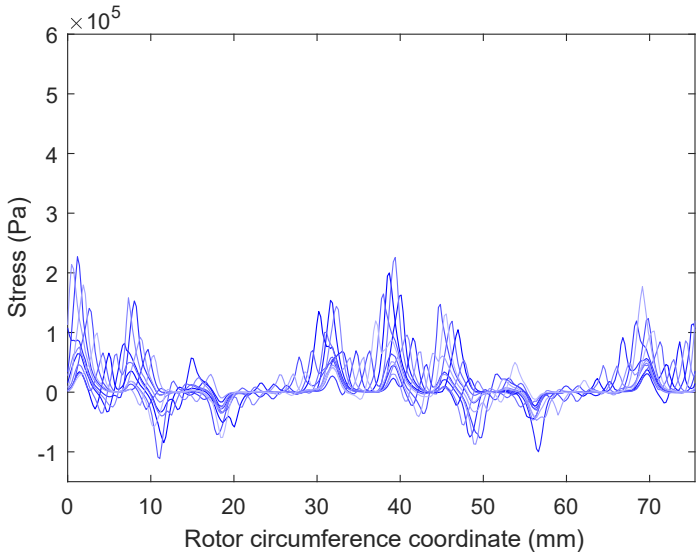

(b) High-speed operating point.

Figure 4.30: Tangential magnetic stresses of the prototype sweeping the rotor position.

4.5.2 Structural analysis

The structural analysis is carried out in *ProjectChrono* [61], which is a "physics-based modeling and simulation infrastructure based on a platform-independent open-source design implemented in C++" [62]. The choice of this tool comes for two of its key features: support for Finite Element Method and massive parallel computations for large scale simulations. This last feature is really important to manage practically the huge amount of FEA elements that are needed to describe the full rotor, in order to have an accurate enough representation of the stress acting on the bridge regions, that are a limited fraction of the overall rotor volume [63].

The possibility to describe the system using C++ code, coupled with powerful parallel solvers that can run on clusters and GPUs, strives for high throughput, thus enabling fine meshes and accurate stress results, that could otherwise be heavily biased. Since ProjectChrono lacks a mesher, the specific module of the open-source SALOME [64] suite is used to create the mesh starting from the rotor geometry. Specific attention is paid to the mesh symmetry which has been realized manually using only quadrangular elements.

As Fig. 4.31 shows, the structural analysis, in addition to determine how the mechanical stress due to the rotor magnetization affects the bridges, accounts for the centrifugal forces due to the distributed iron mass inside the rotor and to the concentrated one of the magnets; hence, load-carrying capacity of PMs is neglected. This allows to completely understand the effects of the rotor shape with respect to the bridge shapes, and also to see if the mass distribution is detrimental for the overall rotor reliability.

During the static linear simulation, centrifugal force to which the i-th element of the rotor is subjected is calculated by means of the following equation:

$$F_{c_i} = m_i \, r_i \, \omega^2 \tag{4.40}$$

where m_i and r_i are, respectively, the mass and distance from rotating axis of the i-th element. Subsequently, the centrifugal force of the element is applied

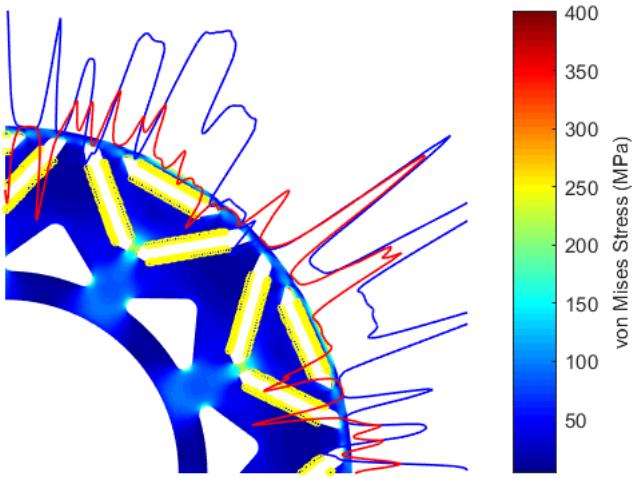

Figure 4.31: Prototype stress field at the high-speed operating point. Yellow dots mark the points where the magnets mass has been added. In blue and red, the radial and tangential magnetic stresses respectively.

to the nodes of the same element. In addition, the proper amount of centrifugal force due to the PMs is applied to the nodes in contact with magnets.

At maximum torque, it is clear that the effect of the magnetic forces is predominant. In fact, we could expect that the stress due to centrifugal forces - since they are directed along the radial direction - should appear as uniformly distributed along the inner central bridge section, as in the case of a simply stretched beam (Fig. 4.32b). On the contrary, at lower speeds, the torque exerted by the magnetic forces on the rotor should manifest a more prominent shear and bending effect, thus implying a non-uniform stress field over the section of the inner central bridge (see Fig. 4.32a). At maximum speed (Figs. 4.32b–4.33b), the centrifugal forces are prevailing and their effect is distinctly having an heavier impact on the stress distribution and peak value, compared to that of the maximum torque case.

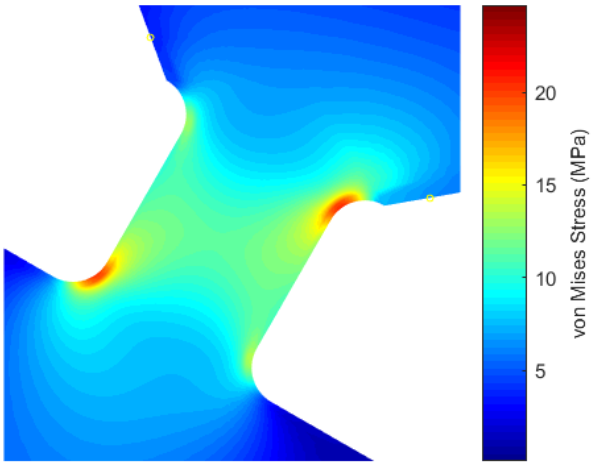

(a) High-torque operating point.

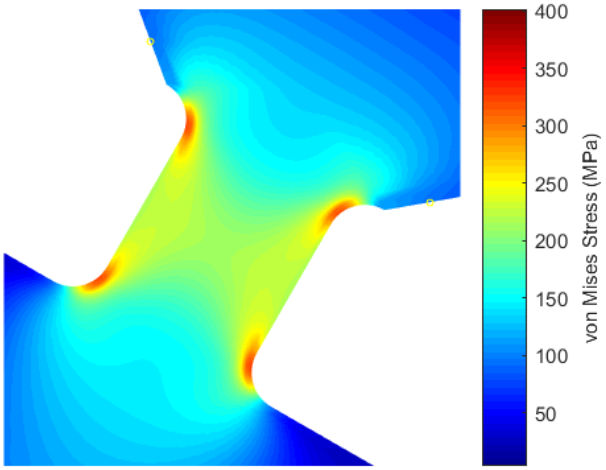

(b) High-speed operating point.

Figure 4.32: Structural analysis detail of the inner central bridge.

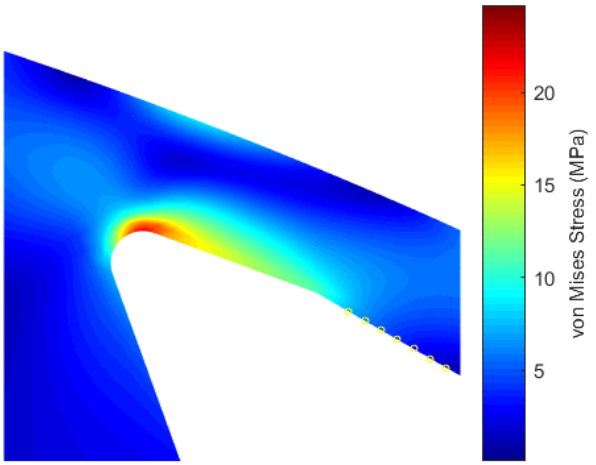

(a) High-torque operating point.

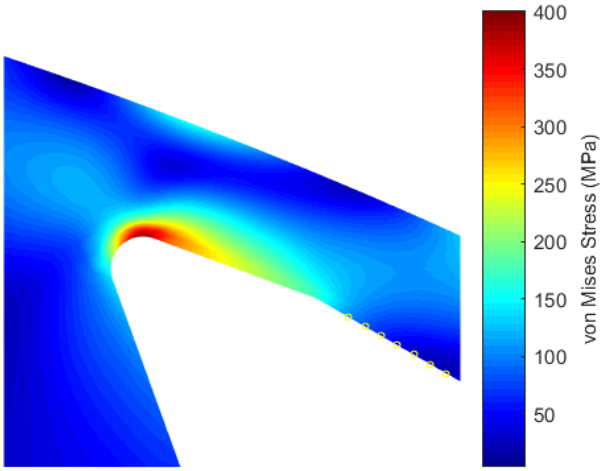

(b) High-speed operating point.

Figure 4.33: Structural analysis detail of the outer central bridge.

In conclusion, the maximum von Mises stress in the prototype resulted approximately 400 MPa at 20 000 rpm while the lamination M250-A35 has a yield stress of 455 MPa [65], so the mechanical-loading test is passed. The von Mises stress in the maximum torque base speed operating condition does not exceed 25 MPa therefore can be neglected. Fig. 4.34 shows a 3D rendering of the prototype lamination stack to give a direct visualization of the geometric proportions.

Table 4.8: Specific torque and power comparison. These values are computed neglecting the water jacket, case and gearbox mass.

Motor	**Specific torque** (Nm/kg)	**Specific power** (kW/kg)
Prototype	10.2	4.4
Prius	9.4	2.7
LS 600h	9.8	5.4
i3	7.1	3.6

Typically, the two most used figures of merit to compare electric motors for traction applications are: the specific torque and the specific power. As Tab. 4.8 shows, the prototype results better than most of the motors considered in chapter 2. Tab. 4.8 values differ from those in Tab. 3 as only the mass of the iron core, copper and PM is taken into account. This choice is necessary in order to compare motors in fair conditions since the mass of the mechanical components of the prototype is yet unknown. The prototype results are particularly remarkable considering that the electric machines figures of merit naturally improve as the torque and power ratings increase. For instance, the LS 600h specific power is higher than that of the prototype but the LS 600h power rating (165 kW) is about twice the prototype one (70 kW). On the contrary, the prototype outperforms the BMW i3 despite the latter having higher ratings (125 kW and 250 N m).

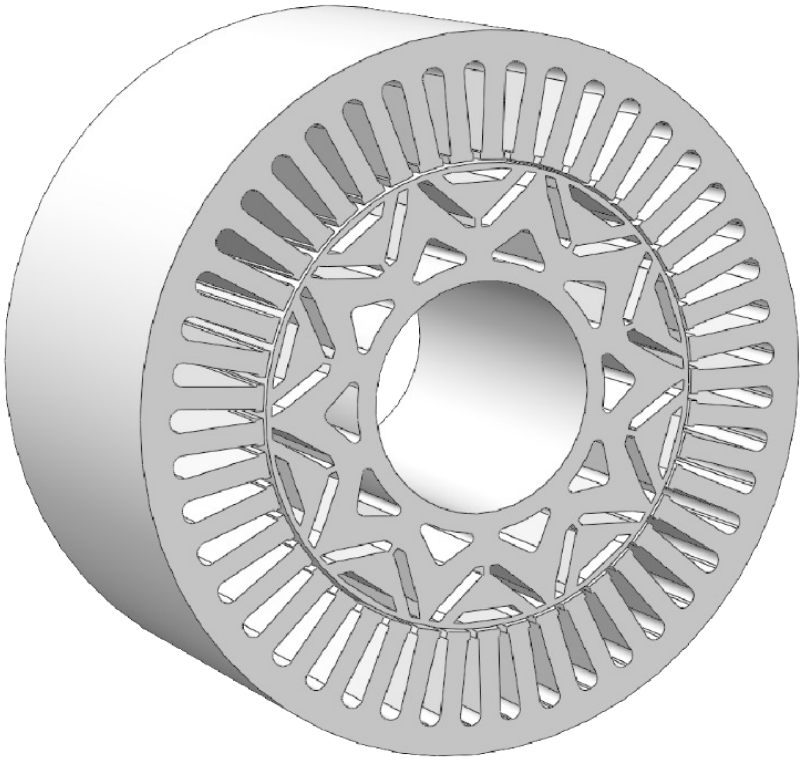

Figure 4.34: Lamination stack rendering of the prototype motor.

Conclusions

The automotive industry is highly competitive as the manufacturers competing for the market are many and customers are extremely demanding in all respects: reliability, safety, performance, cost. In this context, the traction motor design flow must be sound and scientifically rigorous.

This work has investigated the influence of the main design parameters on the electromagnetic performances of the electrical machines for automotive traction applications by using analytical methods and Finite Element simulations. Through a comprehensive comparative study between the Toyota 2010 Prius and Lexus 2008 LS 600h, the most important trade-offs and technical solutions have been pointed out and examined in-depth. Finally, the results of the analysis have been used to design a new prototype motor for the SAE Student Formula, with specific power and torque levels highly considerable.

Two additional novel contributions have been proposed: a closed-form recursive magnetic model very useful in the rotor geometry optimization by virtue of its flexibility and computational efficiency; and a new saliency-enhanced spoke-type rotor topology which enables substantial savings in the total amount of the expensive rare-earth PM.

In future, this prototype shall be realized and tested as well as the presented V-holes spoke-type topology. Also the proposed magnetic model can be further developed including several secondary effects such as iron ribs nonidealities and the machine core magnetic nonlinearity.

In addition, academic research is now focusing on different permanent mag-

net materials in order to replace the rare-earth PMs and to explore the IPM design possibilities provided for instance by AlNiCo magnets, such as Variable-flux Permanent Magnet Machines or Memory Motors. Among the other lines of research, the polyphase machines, to enhance the fault tolerance, as well as the "high torque" machines (e.g.: Vernier, Switched-Flux), to remove the mechanical single-speed gearbox, have to be mentioned. Also Axial-Flux motors are attracting more and more attentions.

Generally speaking, the motor topologies adopted by the automotive industry appear rather established: Tesla and recently Mercedes have chosen the asynchronous motors while the vast majority of the other car manufacturers have selected IPM motors. Except for the introduction of hairpin windings, today's motors do not show substantial differences from the two case studies analyzed in this work. Probably, the underlying reasons are the battery-related critical issues, whose priority is higher at present.

Looking at a Tesla Model S, the battery pack weights 540 kg and costs 45 000 $. The whole curb weight of the car is about 2 000 kg and its price is 90 000 $. Similar numbers can be observed examining a Chevrolet Bolt. Its curb weight is 1 600 kg and it costs 37 500 $, whereas the battery pack weights 436 kg and costs 12 500 $. In other words, the impact of the battery pack on the vehicle price and weight is huge, therefore car manufacturers see the battery technical innovation as the key for market competitiveness. A not fully optimized electric motor is still better than the most advanced ICE available on the market today, but a 20 % reduction of the battery weight or cost can make a lot of difference.

Vehicles in the J and M segments, such as Sport Utility Vehicles and Crossovers, have more space on-board to place large battery packs, hence the next generation EVs will likely belong to those categories (e.g.: Jaguar I-Pace, Audi e-tron, Mercedes EQC, Tesla Model X). The great power scalability of the electric motor in terms of density seen in Tab. 3, will support this trend since providing many horsepowers to the car does not enlarge the motor as much as would be with ICEs.

However, as happens for the motor technology, car manufacturers do not

share the same view on the vehicle energy sources. Toyota has never believed in bulky and expensive battery packs and this is the reason why many years ago it invested in the full-hybrid technology. Today, Toyota thinks that fuel cells are the future of EVs. At present, sales of Toyota's hydrogen fuel cell *Mirai* cars amount to around 3 000 per year globally, but this number is expected to grow significantly in the next two or three years to at least 30 000 annually. As a consequence, Toyota plans to step up its component production to meet demand. The hydrogen technology has a remarkable advantage over lithium batteries in terms of both weight and cost. In addition, the refuel time is very much quicker than that of lithium batteries (basically the same as for gasoline cars).

Unfortunately, another important problem still remains. The weather and traffic conditions influence significantly the range of EVs and HEVs. Conventional ICE vehicles re-use engine exhaust heat to provide the warm air to the cabin, while EVs make use of power consuming electric heaters and HEVs keep the engine running more than necessary. As an example, the Renault Zoe range drops to about 48 % when heaters are on and to around 75 % with air-conditioning.

The frequent "start-and-stop" related to heavy traffic conditions can also shorten the vehicle range. Autonomous vehicles could be the answer together with increased connectivity. Vehicle-to-Vehicle (V2V) and Vehicle-to-Infrastructure (V2I) technology allows the car to communicate with other cars and the infrastructure like traffic lights. Vehicle speed and the distance to other vehicles can be adjusted immediately in response to conditions on the road. Moreover, with cloud connectivity, information can be shared to minimize traffic congestion and to optimize fleet-wide fuel efficiency by means of platooning systems. Platooning dynamically chains vehicles to maximize fuel efficiency. Enhanced car-to-car reporting enables platooning with intelligent stop and go, high-speed merging, and obstacle avoidance. Despite some variability, fuel consumption and emissions reductions tend to be significant (up to 21 %).

In conclusion, whichever will be the future transport technologies, a radical

change of the infrastructures concerning the energy distribution, production and information network will be necessary. This process could involve a massive transformation of both the urban and rural areas, thus it should be considered with careful attention.

Bibliography

[1] B. Bilgin and A. Emadi. Electric motors in electrified transportation: A step toward achieving a sustainable and highly efficient transportation system. *IEEE Power Electronics Magazine*, 1(2):10–17, June 2014. doi:10.1109/MPEL.2014.2312275.

[2] Siang Fui Tie and Chee Wei Tan. A review of energy sources and energy management system in electric vehicles. *Renewable and Sustainable Energy Reviews*, 20:82 – 102, 2013. doi:https://doi.org/10.1016/j.rser.2012.11.077.

[3] Tinton Dwi Atmaja and Amin. Energy storage system using battery and ultracapacitor on mobile charging station for electric vehicle. *Energy Procedia*, 68:429 – 437, 2015. 2nd International Conference on Sustainable Energy Engineering and Application (ICSEEA) 2014 Sustainable Energy for Green Mobility. doi:https://doi.org/10.1016/j.egypro.2015.03.274.

[4] Theodoros Grigoratos, Giorgio Martini. *Non-exhaust traffic related emissions. Brake and tyre wear PM.* European Commission - Joint Research Centre - Institute for Energy and Transport, Luxembourg: Publications Office of the European Union, 2014. doi:10.2790/21481.

[5] UBS, s.l. *UBS Evidence Lab Electric Car Teardown – Disruption Ahead?*, 2017.

[6] European Commission. *GEAR 2030 Strategy 2015-2017 - Comparative analysis of the competitive position of the EU automotive industry and the impact of the introduction of autonomous vehicles, Final report*, 2017.

[7] Tim Burress. U.S. DOE Vehicle Technologies Office 2015 Annual Merit Review: Benchmarking EV and HEV Technologies. Technical report, Oak Ridge National Laboratory, June 2016.

[8] Lambros K. Mitropoulos, Panos D. Prevedouros, and Pantelis Kopelias. Total cost of ownership and externalities of conventional, hybrid and electric vehicle. *Transportation Research Procedia*, 24:267 – 274, 2017. 3rd Conference on Sustainable Urban Mobility, 3rd CSUM 2016, 26 – 27 May 2016, Volos, Greece. doi:https://doi.org/10.1016/j.trpro.2017.05.117.

[9] UBS, s.l. *UBS Evidence Lab: What consumers think about electric cars, and what it means for auto profits*, 2016.

[10] D. G. Dorrell, A. M. Knight, M. Popescu, L. Evans, and D. A. Staton. Comparison of different motor design drives for hybrid electric vehicles. In *2010 IEEE Energy Conversion Congress and Exposition*, pages 3352–3359, Sep. 2010. doi:10.1109/ECCE.2010.5618318.

[11] A. Mebarki, D. Gerada, and N. L. Brown. Analysis of an axial PM flux machine with field weakening capability for engine integration. In *7th IET International Conference on Power Electronics, Machines and Drives (PEMD 2014)*, pages 1–6, April 2014. doi:10.1049/cp.2014.0495.

[12] A. Emadi. *Advanced Electric Drive Vehicles*. Energy, Power Electronics, and Machines. Taylor & Francis, 2014.

[13] G. Pellegrino, A. Vagati, B. Boazzo, and P. Guglielmi. Comparison of Induction and PM Synchronous Motor Drives for EV Application Including Design Examples. *IEEE Transactions on Industry Applications*, 48(6):2322–2332, Nov 2012. doi:10.1109/TIA.2012.2227092.

[14] G. Pellegrino, A. Vagati, P. Guglielmi, and B. Boazzo. Performance Comparison Between Surface-Mounted and Interior PM Motor Drives for Electric Vehicle Application. *IEEE Transactions on Industrial Electronics*, 59(2):803–811, Feb 2012. doi:10.1109/TIE.2011.2151825.

[15] J. Pyrhonen, T. Jokinen, and V. Hrabovcova. *Design of Rotating Electrical Machines*. Wiley, 2013.

[16] N. Bianchi and T.M. Jahns. *Design, Analysis, and Control of Interior PM Synchronous Machines: Tutorial Course Notes ; Seattle, Oct. 5, 2004*. CLEUP, 2004.

[17] Timothy A Burress, Steven L Campbell, Chester Coomer, Curtis William Ayers, Andrew A Wereszczak, Joseph Philip Cunningham, Laura D Marlino, Larry Eugene Seiber, and Hua-Tay Lin. Evaluation of the 2010 toyota prius hybrid synergy drive system. *Oak Ridge National Laboratory*, March 2011. doi:10.2172/1007833.

[18] T.A. Burress, C.L. Coomer, S.L. Campbell, A.A. Wereszczak, J.P. Cunningham, L.D. Marlino, L.E. Seiber, and H.T. Lin. Evaluation of the 2008 lexus ls 600h hybrid synergy drive system. *Oak Ridge National Laboratory*, Jan 2009. doi:10.2172/947393.

[19] B. Ozpineci. Fy2016 electric drive technologies annual progress report. *Oak Ridge National Laboratory*, July 2017. doi:10.2172/1413876.

[20] N. Bianchi. *Electrical Machine Analysis Using Finite Elements*. Power Electronics and Applications Series. CRC Press, 2017.

[21] J.J. Cathey. *Electric Machines: Analysis and Design Applying Matlab*. McGraw-Hill series in electrical and computer engineering. McGraw-Hill, 2001.

[22] G. Pietrini, A. Soldati, C. Concari, and N. Bianchi. General Magnetic Model for the Analysis and Optimization of Multiple Barrier Rotors. In *2018 IEEE Energy Conversion Congress and Exposition (ECCE)*, 2018.

[23] T. Jahns. Getting Rare-Earth Magnets Out of EV Traction Machines: A review of the many approaches being pursued to minimize or eliminate rare-earth magnets from future EV drivetrains. *IEEE Electrification Magazine*, 5(1):6–18, March 2017. doi:10.1109/MELE.2016.2644280.

[24] K. Rahman, S. Jurkovic, P. J. Savagian, N. Patel, and R. Dawsey. Retrospective of electric machines for EV and HEV traction applications at general motors. In *2016 IEEE Energy Conversion Congress and Exposition (ECCE)*, pages 1–8, Sep. 2016. doi:10.1109/ECCE.2016.7855402.

[25] F. Cupertino, G. M. Pellegrino, E. Armando, and C. Gerada. A SyR and IPM machine design methodology assisted by optimization algorithms. In *2012 IEEE Energy Conversion Congress and Exposition (ECCE)*, pages 3686–3691, Sept 2012. doi:10.1109/ECCE.2012.6342478.

[26] Y. Duan and D. M. Ionel. A review of recent developments in electrical machine design optimization methods with a permanent magnet synchronous motor benchmark study. In *2011 IEEE Energy Conversion Congress and Exposition*, pages 3694–3701, Sept 2011. doi:10.1109/ECCE.2011.6064270.

[27] N. Bianchi and S. Bolognani. Design optimisation of electric motors by genetic algorithms. *IEE Proceedings - Electric Power Applications*, 145(5):475–483, Sep 1998. doi:10.1049/ip-epa:19982166.

[28] SyR-e. Synchronous Reluctance (machines) Evolution. URL: https://sourceforge.net/projects/syr-e/.

[29] D.C. Meeker. Finite element method magnetics, Version 4.2. http://www.femm.info.

[30] G. Pietrini, A. Soldati, C. Concari, and N. Bianchi. Saliency-enhanced Spoke-type Rotor Geometry for Permanent Magnet Volume Reduction in Hybrid and Electric Vehicle Motors. In *2018 IEEE Energy Conversion Congress and Exposition (ECCE)*, 2018.

[31] A. Fatemi, D. M. Ionel, M. Popescu, and N. A. O. Demerdash. Design optimization of spoke-type PM motors for Formula E racing cars. In *2016 IEEE Energy Conversion Congress and Exposition (ECCE)*, pages 1–8, Sept 2016. doi:10.1109/ECCE.2016.7855032.

[32] M. Kimiabeigi, R. Long, J. D. Widmer, and Y. Gao. Comparative assessment of single piece and fir-tree-based spoke type rotor designs for low-cost electric vehicle application. *IEEE Transactions on Energy Conversion*, 32(2):486–494, June 2017. doi:10.1109/TEC.2017.2662579.

[33] M. Kimiabeigi, J. D. Widmer, R. Long, Y. Gao, J. Goss, R. Martin, T. Lisle, J. M. S. Vizan, A. Michaelides, and B. C. Mecrow. On selection of rotor support material for a ferrite magnet spoke-type traction motor. *IEEE Transactions on Industry Applications*, 52(3):2224–2233, May 2016. doi:10.1109/TIA.2016.2530722.

[34] M. Popescu, I. Foley, D. A. Staton, and J. E. Goss. Multi-physics analysis of a high torque density motor for electric racing cars. In *2015 IEEE Energy Conversion Congress and Exposition (ECCE)*, pages 6537–6544, Sept 2015. doi:10.1109/ECCE.2015.7310575.

[35] H. Mahmoud, G. Bacco, M. Degano, N. Bianchi, and C. Gerada. Synchronous Reluctance Motor Iron losses: Considering Machine Non-Linearity at MTPA, FW, and MTPV Operating Conditions. *IEEE Transactions on Energy Conversion*, pages 1–1, 2018. doi:10.1109/TEC.2018.2811543.

[36] V. Ostović. *The Art and Science of Rotating Field Machines Design: A Practical Approach.* Springer International Publishing, 2016.

[37] Dolomites. Design Of eLectrical MachInes & drivES. URL: https://sourceforge.net/projects/dolomites/.

[38] T.L. Bergman, F.P. Incropera, A.S. Lavine, and D.P. DeWitt. *Introduction to Heat Transfer.* Wiley, 2011.

[39] J. Welty, C.E. Wicks, G.L. Rorrer, and R.E. Wilson. *Fundamentals of Momentum, Heat and Mass Transfer*. Wiley, 2007.

[40] J. Saari. *Thermal analysis of high speed induction machines*. PhD thesis, Helsinki University of Technology, 1998.

[41] Björn Anderssson. Lumped Parameter Thermal Modelling of Electric Machines. Master's thesis, Chalmers University of Technology, 2013. 72.

[42] A. J. Grobler, S. R. Holm, and G. van Schoor. A Two-Dimensional Analytic Thermal Model for a High-Speed PMSM Magnet. *IEEE Transactions on Industrial Electronics*, 62(11):6756–6764, Nov 2015. doi:10.1109/TIE.2015.2435693.

[43] Gilbert Moreno. Thermal Performance Benchmarking: Annual Report. *National Renewable Energy Laboratory*, April 2016.

[44] J. Emily Cousineau, Kevin Bennion, Doug DeVoto, Mark Mihalic, Sreekant Narumanchi. Characterization of Contact and Bulk Thermal Resistance of Laminations for Electric Machines. *National Renewable Energy Laboratory*, June 2015.

[45] K. Bennion and J. Cousineau. Sensitivity analysis of traction drive motor cooling. In *2012 IEEE Transportation Electrification Conference and Expo (ITEC)*, pages 1–6, June 2012. doi:10.1109/ITEC.2012.6243512.

[46] Mingda Liu. Cooling design and thermal analysis for dual-stator 6-slot 4-pole flux-switching permanent magnet machine. Master's thesis, University of Wisconsin-Madison, 9 2017.

[47] P. H. Mellor, D. Roberts, and D. R. Turner. Lumped parameter thermal model for electrical machines of TEFC design. *IEE Proceedings B - Electric Power Applications*, 138(5):205–218, Sept 1991. doi:10.1049/ip-b.1991.0025.

[48] R. Wrobel and P. H. Mellor. A General Cuboidal Element for Three-Dimensional Thermal Modelling. *IEEE Transactions on Magnetics*, 46(8):3197–3200, Aug 2010. doi:10.1109/TMAG.2010.2043928.

[49] D. Kuehbacher, A. Kelleter, and D. Gerling. An improved approach for transient thermal modeling using lumped parameter networks. In *2013 International Electric Machines Drives Conference*, pages 824–831, May 2013. doi:10.1109/IEMDC.2013.6556188.

[50] M. Fénot, Y. Bertin, E. Dorignac, and G. Lalizel. A review of heat transfer between concentric rotating cylinders with or without axial flow. *International Journal of Thermal Sciences*, 50(7):1138 – 1155, 2011. doi:https://doi.org/10.1016/j.ijthermalsci.2011.02.013.

[51] Distribution of velocity and temperature between concentric rotating cylinders. *Proceedings of the Royal Society of London A: Mathematical, Physical and Engineering Sciences*, 151(874):494–512, 1935. doi:10.1098/rspa.1935.0163.

[52] Zeng-Yuan Guo, Hong-Ye Zhu, and Xin-Gang Liang. Entransy—a physical quantity describing heat transfer ability. *International Journal of Heat and Mass Transfer*, 50(13):2545 – 2556, 2007. doi:https://doi.org/10.1016/j.ijheatmasstransfer.2006.11.034.

[53] Z.Y. Guo, X.B. Liu, W.Q. Tao, and R.K. Shah. Effectiveness–thermal resistance method for heat exchanger design and analysis. *International Journal of Heat and Mass Transfer*, 53(13):2877 – 2884, 2010. doi:https://doi.org/10.1016/j.ijheatmasstransfer.2010.02.008.

[54] E. C. Lovelace, T. M. Jahns, T. A. Keim, and J. H. Lang. Mechanical design considerations for conventionally laminated, high-speed, interior PM synchronous machine rotors. *IEEE Transactions on Industry Applications*, 40(3):806–812, May 2004. doi:10.1109/TIA.2004.827440.

[55] M. Barcaro, G. Meneghetti, and N. Bianchi. Structural Analysis of the Interior PM Rotor Considering Both Static and Fatigue Loading. *IEEE Transactions on Industry Applications*, 50(1):253–260, Jan 2014. doi:10.1109/TIA.2013.2268048.

[56] M. Amrhein and P. T. Krein. Force Calculation in 3-D Magnetic Equivalent Circuit Networks With a Maxwell Stress Tensor. *IEEE Transactions on Energy Conversion*, 24(3):587–593, Sept 2009. doi:10.1109/TEC.2009.2016142.

[57] K. J. Meessen, J. J. H. Paulides, and E. A. Lomonova. Force Calculations in 3-D Cylindrical Structures Using Fourier Analysis and the Maxwell Stress Tensor. *IEEE Transactions on Magnetics*, 49(1):536–545, Jan 2013. doi:10.1109/TMAG.2012.2206821.

[58] F. Freschi and M. Repetto. Natural Choice of Integration Surface for Maxwell Stress Tensor Computation. *IEEE Transactions on Magnetics*, 49(5):1717–1720, May 2013. doi:10.1109/TMAG.2013.2240668.

[59] A. Bermúdez, A. L. Rodríguez, and I. Villar. Extended Formulas to Compute Resultant and Contact Electromagnetic Force and Torque From Maxwell Stress Tensors. *IEEE Transactions on Magnetics*, 53(4):1–9, April 2017. doi:10.1109/TMAG.2016.2633316.

[60] M. K. Ghosh, Y. Gao, H. Dozono, K. Muramatsu, W. Guan, J. Yuan, C. Tian, and B. Chen. Proposal of Maxwell Stress Tensor for Local Force Calculation in Magnetic Body. *IEEE Transactions on Magnetics*, pages 1–4, 2018. doi:10.1109/TMAG.2018.2844310.

[61] A. Tasora, R. Serban, H. Mazhar, A. Pazouki, D. Melanz, J. Fleischmann, M. Taylor, H. Sugiyama, and D. Negrut. Chrono: An open source multi-physics dynamics engine. pages 19–49. Springer, 2016.

[62] Project Chrono. Chrono: An Open Source Framework for the Physics-Based Simulation of Dynamic Systems. http://projectchrono.org.

[63] G. B. Sinclair and Sevda Sezer. Practical Convergence-Divergence Checks for Stresses from FEA. In *International ANSYS conference*, 2006.

[64] OPEN CASCADE. SALOME: The Open Source Integration Platform for Numerical Simulation. https://www.salome-platform.org/, 2000–2018.

[65] Cogent. Electrical Steel Non Oriented Fully Processed Datasheet. `https://cogent-power.com/cms-data/downloads/m250-35a_1.pdf`. Accessed: 2018-07-31.

Ringraziamenti

Innanzitutto vorrei ringraziare coloro i quali mi hanno permesso d'intraprendere questo percorso di studio e di crescita professionale: la mia famiglia, naturalmente, che mi è sempre stata accanto sostenendomi e incoraggiandomi, i professori Carlo Concari e Giovanni Franceschini sotto la cui direzione il laboratorio di automazione industriale dell'Università di Parma ha raccolto la sfida della mobilità elettrica di nuova generazione, e il prof. Nicola Bianchi dell'Università degli Studi di Padova per l'indispensabile contributo fornito al mio lavoro.

Inoltre, non posso certo dimenticare i molti "compagni di viaggio" che hanno condiviso questa esperienza con me nel corso dei tre anni di dottorato: tutti i ragazzi del MEltIngLab inclusi i membri di TeMec Drive nonché i numerosi tesisti e colleghi dottorandi conosciuti per più o meno tempo. Insieme ad alcuni di loro ho avuto l'onore di lavorare e confrontarmi raggiungendo risultati che da solo non avrei mai potuto realizzare. Dedico quindi un particolare ringraziamento a questi ultimi.